Transmission of Vibration Caused by Unbalance in an Aircraft Engine with Active Control Strategies

Dem Fachbereich Maschinenbau
an der Technischen Universität Darmstadt
zur
Erlangung des Grades eines Doktor-Ingenieurs (Dr.-Ing.)
genehmigte

Dissertation

vorgelegt von

Xiaonan Zhao, M.Sc.

aus Jincheng

Berichterstatter:	Prof. Dr.-Ing. S. Rinderknecht
Mitberichterstatter:	Prof. Dr.-Ing. B. Schweizer
Tag der Einreichung:	04.08.2015
Tag der mündlichen Prüfung:	14.10.2015

Darmstadt 2015

D 17

Preface

The research described herein was conducted when I did the PhD study under the supervision of Professor Stephan Rinderknecht at Institute for Mechatronic Systems, Technical University Darmstadt, as a member of DFG-Graduiertenkolleg 'Transient System Modeling of aircraft engines', between April 2012 and October 2015.

I am very grateful to my supervisor Professor Rinderknecht for his trust in me to work on this topic, his timely lead and great enthusiasm in my results, and also to Professor Bernhard Schweizer for the takeover as the co-referent and interesting discussion.

I would also like to thank Rolls-Royce Deutschland, who funded this project and provided me the chance to learn about the whole engine model and simulating methods on site, and especially Mr. Roland Blutke, who accompanied this work almost from the very beginning until the end.

Finally, I take this opportunity to express my gratitude to my colleagues, Fabian Becker, Daniel Ploeger, Philipp Zech, in particular to Ramakrishnan Ambur and Stefan Heindel, for the enlightening discussion, valuable comments and their effort in the correction at the end phase of this work. Thanks also to the ex-colleagues who helped me working my way into the topic at the beginning phase, Zhentao Wang, Sebastian Schittenhelm and Matthias Borsdorf, and to all other colleagues, who was always ready to support in all aspects.

Darmstadt, 29 Jan 2016

Xiaonan Zhao

Contents

List of Abbreviations

Abbr.	Description
ActBrg	Active bearing
ActExSus	Active external suspension
ActInSus	Active internal suspension
ANC	Active noise control
ASC	Active structural control
AVA	Active vibration absorber
AVC	Active vibration control
B1	Bearing 1
B2	Bearing 2
B3	Bearing 3
B4	Bearing 4
B5	Bearing 5
CMS	Component mode synthesis
DOF	Degree of freedom
FBC	Front bearing chamber
FE	Finite element
FLL	Front lower link
FRAC	Frequency response assurance criteria
FUL	Front upper link
FxLMS	Filtered-x least mean square
HPC	High pressure compressor
HPR	High pressure rotor
HPT	High pressure turbine
IFF	Integral force feedback
IMC	Intermediate casing
JntB34	Junctions between bearing 3 & bearing 4 and the non-rotating part
JntENG	Junctions between engine and engine mount system
JntFL	Junctions between fuselage and engine mount system

Li.	Linear
LMS	Least mean square algorithm
LPC	Low pressure compressor
LPR	Low pressure rotor
LPT	Low pressure turbine
LQG	linear-quadratic Gaussian algorithm
LQR	linear-quadratic regulator
MAC	Modal assurance criterion
MNT	Engine mount system
Opt.	Optimizing/optimization/optimized
RMR	Rear mount ring
RMS	Root mean square
Ro.	Rotational
SC	Squirrel cage
SFD	Squeeze film damper
sq.	Squared
SS	State space
thr.	through
VDV	Vibration dose value
WEM	Whole engine model
w/o	Without

List of Symbols

Latin	Unit	Description
A	$\mathrm{mm/s^2}$	Acceleration in frequency domain
A_{ssm}		System matrix of state space model
B_{ssm}		Input matrix of state space model
C_{ssm}		Output matrix of state space model
C_{IFF}		Transfer function of integral force feedback control
D	$\mathrm{N\,s/mm}$	Damping matrix
D_{ssm}		Feedthrough matrix of state space model
F	N	Force in frequency domain
G	$\mathrm{kg\,mm^2/s}$	Gyroscopic matrix
I		Identity matrix
I_x	$\mathrm{kg\,mm^2}$	Moment of inertia about a diameter
J		Cost function
K_{dyn}	N/mm	Dynamic stiffness matrix
K_{LQR}		Transfer function of LQR controller
K_{st}	N/mm	Static stiffness matrix
M	kg	Mass matrix
M_θ	N mm	Moment
N		Weighting matrix for the coupling of states and actuation forces in cost function of LQR control design
P_r		Solution matrix of algebraic Riccati equation
$\bar{P}$	mW	Complex mechanical power
P	mW	Mechanical power in frequency domain
P_{av}	mW	Time-average value of mechanical power
$P(z)$		Transfer function of primary path
Q		Weighting matrix for the states in cost function of LQR control design
Q_y		Weighting matrix for the outputs in cost function of LQR control design

R		Weighting matrix for the actuation forces in cost function of LQR control design
$S(z)$		Transfer function of secondary path
$\tilde{S}(z)$		Estimated secondary path
T	s	Time (constant)
T_{av}	mJ	Time-average value of kinetic energy
T_{res}		Transformation matrix to resolve a single direction into the three degrees of freedom x,y and z
U_{av}	mJ	Time-average value of potential energy
V	mm/s	Velocity in frequency domain
V^{eig}		Eigenvector
$W(z)$		Adaptive filter
X		Physical degrees of freedom in frequency domain
Z		Transfer function
a	$\mathrm{mm/s^2}$	Acceleration in time domain
a_p	$\mathrm{mm/s^2}$	Weighted RMS acceleration at a point 'p'
a_{px}, a_{py}, a_{pz}	$\mathrm{mm/s^2}$	Weighted RMS acceleration at a point 'p' in x, y and z direction
a_r	$\mathrm{mm/s^2}$	Running RMS acceleration
a_{rms}	$\mathrm{mm/s^2}$	Weighted RMS acceleration
a_w	$\mathrm{mm/s^2}$	Weighted acceleration
d	N s/mm	Damping
e		Napier's constant
$e(z)$		Error signal
f	N	Force in time domain
g		Coefficient of integral feedback control
j		Imaginary unit
k	N/mm	Stiffness
k_r	N/mm	Rigid stiffness
m	kg	Mass
n_a		Number of actuators
n_s		Number of sensors
p	mW	Mechanical power in time domain
q_c	N	Control force (the values of real and imaginary parts separately listed in a vector)

t	s	Time
u	mm	Displacement of translational degrees of freedom
$u(z)$	N	Generated actuation force in FxLMS algorithm
v	mm/s	Velocity in time domain
x		States of state space model or physical degrees of freedom in time domain
$x(z)$	N	Reference input of FxLMS algorithm
$\tilde{x}(z)$	N	Estimated input of FxLMS algorithm
y		Generalized modal degrees of freedom
y_{out}		Outputs of the system
$y_{act}(z)$		Response from actuation forces to sensor positions
$y_d(z)$		Response from unbalance to sensor positions

Greek	**Unit**	**Description**
α		Coefficient of the quadratic term of the cost function
β, β_1, β_2		Coefficients of the linear term of the cost function
ϵ	mm	Eccentricity
ϕ_a	rad	Addition of phase angles of force and velocity
ϕ_d	rad	Difference of phase angles of force and velocity
ϕ_s		Normal modes of slave DOFs when the interface nodes are fixed
γ		Constant term of the cost function
η	s	Stiffness-proportional damping coefficient
η_{dmp}		Damping effect
μ	s^{-1}	Mass-proportional damping coefficient
μ_X		Mean of X
θ	rad	Displacement of rotational degrees of freedom
ρ		Step size of FxLMS algorithm
$\rho_{X,Y}$		Pearson's correlation coefficient
σ_X		Standard deviation of X
Ω	rad/s	Rotational speed
ω	rad/s	Angular frequency

Notation	**Description**
$\dot{\square}$	First derivative with respect to time
$\ddot{\square}$	Second derivative with respect to time

$\{\square\}$	Vector
$[\square]$	Matrix
$[\square]^*$	Hermitian/conjugate transpose
$[\square]^T$	Transpose
$E(\square)$	Expectation value
$Im(\square)$	Imaginary part of a complex expression
$min(\square)$	Minimum of the variable
$Re(\square)$	Real part of a complex expression

Index	**Description**
$\square_a$	Relevant to acceleration
$\square_{act}$	Relevant to actuation
$\square_c$	Relevant to the control force
$\square_f$	Relevant to force
$\square_g$	Relevant to gyroscopic effect
$\square^i$	Imaginary part of the variable
$\square_m$	Corresponding to the master degrees of freedom
$\square_{opt}$	Optimized results
$\square_{out}$	Relevant to outputs
$\square_p$	Relevant to the primary force, i.e. the disturbance
$\square_{pw}$	Relevant to power
$\square^r$	Real part of the variable
$\square_{rsp}$	Frequency response in terms of the variable
$\square_s$	Corresponding to the slave degrees of freedom
$\square_{sc}$	Relevant to the squirrel cage
$\square_{sen}$	Relevant to sensors/measurements
$\square_{sfd}$	Relevant to squeeze film dampers
$\square_{sq}$	Square of the variable
$\square_{ssm}$	Relevant to a state space model
$\square_u$	Relevant to translational degree of freedom
$\square_{unbalance}$	Caused by unbalance or of unbalance
$\square_x$	Relevant to x-coordinate
$\square_y$	Relevant to y-coordinate
$\square_z$	Relevant to z-coordinate
$\square_\delta$	Truncated set of the variable
$\square_\theta$	Relevant to rotational degree of freedom

List of Figures

List of Tables

1. Introduction

The International Air Transport Association announced that global air travel demand rose by 5.9% in 2014 compared to the year of 2013. In 2014, it was over the average growth rate of 5.6%. With the increase of demand in air travel, the performance of the aircraft is becoming more important in terms of fuel efficiency, safety, comfort, etc. The present research is focused on one of the aspects, namely comfort: Increasing the comfort of the passenger by reducing or isolating the vibrations from the engine with active methods.

This topic involves three points: Evaluation of the comfort in the aircraft, vibration cause and its characteristics in the aircraft engine, application of active vibration reduction or isolation on the aircraft engine. The first two belong to the fundamental study to support the investigation and evaluation of the last one. The application of active methods includes selection and placement of actuators and sensors and control design. Among them, the actuator placement is determinant in the effectiveness of the active method. This research was initiated by a novel idea of actuator placement inside the aircraft engine (see Section 3.2 for the detailed description) with the goal of preventing the vibration from being transmitted into the fuselage where passengers are seated, different from the current passive damping application and the active damping application outside the engine. The investigation was first aimed at determining the effectiveness of this actuator placement approach as well as other two approaches. Then the research was expanded to encompass a study on the mechanism of vibration transmission with these actuation approaches. Based on the results and conclusions, the focus was last shifted to the real world by carrying out a feasibility study.

In Section 1.1, the comfort problem and vibration reduction techniques used in the aircraft engine will be summarized, and the potential to improve the comfort inside the fuselage with active methods will be raised. Section 1.2

will describe how the scope of the research was narrowed down based on the background knowledge, reasonable assumptions and research conditions. In Section 1.3, the structure of the research will be listed, and the logic of the arrangement of chapters will be explained.

1.1. Motivation

In this section, the significance of the comfort issue in the manufacturing industry of aircraft engines and how one of the comfort-related problems, vibration, is caused will be clarified first. Then the current solutions will be listed and compared. Inspired by the limitation of the existing solutions, an initial proposal will finally be raised together with its potential advantages, as the starting point of this research.

1.1.1. Comfort and vibration

The air transportation technology has come a long way these days with respect to operational performance, fuel efficiency, velocity and safety. The cost, along with these improved features, has also been reduced. All these respects make air transportation attractive and affordable to more and more people. This phenomenon draws the attention of aircraft engineers to the sensation of the passengers, that is, the comfort inside the fuselage. The comfort is related to people's satisfaction and determines, to some extent, the frequency of their use. Therefore, aircraft engine manufacturer engineers are getting more interested in improving passenger comfort.

The perceived comfort is influenced both by objective and subjective factors, which correspond to physical and psychological parameters, respectively. From a technical point of view, our concerns are the physical fields: Vibration and noise. In these two fields, comfort can be reflected by acceleration and sound pressure level, respectively [53]. Since the new approach of actuator placement, which is also the starting point of this research, is aimed at controlling the acceleration actively, the comfort issue caused by vibration has been further investigated in this project and will be discussed here.

The unwanted vibration inside the fuselage can be generated by the fol-

lowing problems [27]: Propeller mass unbalance, aerodynamic excitation and abnormal engine vibration. The first of these is due to the mass distribution problem, a basic and the most common cause of excess vibration. When the blades are not pitched equally or airfoils are not matched, propeller aerodynamic unbalance will appear. And the vibrations which result from combustion problems or unmatched engine components can be regarded as abnormal engine vibration. Moreover, poor isolation between the fuselage and the engine is also an important factor in high vibration in the fuselage.

1.1.2. Vibration reduction techniques

Knowing the importance of comfort and various causes of vibration in the fuselage from Section 1.1.1, this section will focus on the vibration reduction methods which were invented and some of which have been successfully applied on the aircraft or on the engine.

The undesired vibration from the engine can be attenuated using either passive or active damping techniques. Passive methods in the past years can be categorized into two groups; one is to use the squeeze film damper (SFD) on the bearing to reduce the vibration at the source of the unbalance, and the other is to employ the passive engine mount, through which the engine is attached to the fuselage, to isolate the fuselage from the vibration of the engine. SFDs are widely used for the vibration reduction of aircraft engines [14]. In the passive engine mount application, different devices can be used, such as solid blocks of rubber, fluid mounts, vibration absorbers, etc. Elastomeric mounts serve to isolate an aircraft engine from its support pylon [20]. Fluid mounts include fluids in elastomeric chambers, the fluids acting as additional damping by resisting motion [37]. An adaptive improvement was found for the fluid mount, i.e. the adaptive fluid mount, which reduces the vibration in a broader frequency range by changing one or more effective variables [29]. The vibration absorber, utilizing the spring-mass system, works according to a similar principle to that of the fluid mount. The tuned vibration absorber, similar to the adaptive fluid mount, increases the operating frequency range by adjusting the length of the spring [68]. These passive mount applications have been improved in the last years in terms of the operating frequency

range. However, they can still not avoid large mass increases, and the increase of the operating frequency range is limited, because the extent of the increase in operating frequency of the passive system depends on the physical parameters of its own structure, e.g. the size.

These passive damping strategies yield good effectiveness at certain frequencies. At the same time, they employ techniques which increase the mass of the engine system, such as the addition of isolating springs and dampers, or add difficulty to the design process, e.g. dealing with the non-linearity in the SFD application [9]. Moreover, these passive techniques do not always provide sufficient bandwidth or attenuation to damp the vibration. Recently active methods have drawn much attention in overcoming the disadvantages of the passive methods.

Various active methods are mainly focused on actuating the engine mount, to build up an active isolation system. In such systems, higher forces can be achieved and enhanced isolation over a broader frequency range can be provided [62]. Active application on the mounting system between the fuselage and the engine has been realized, e.g. the active mount application has been developed and certified by Lord Corporation for the Cessna Citation X and the McDonnell Douglass DC9/MD80 series [6]. While this application improves performance in terms of isolation as mentioned above [62], its downstream position (close to the fuselage) on the vibration transmission path determines its ineffectiveness on the fatigue loading on the upstream path (close to the vibration source) and that a great mount of effort needs to be expended to control it.

In the realm of active vibration control for the aircraft, another approach is the active structural control (ASC), in which the active vibration absorber (AVA) or the actuator excites a structural component at a certain frequency to cancel the input disturbance. The AVAs are often preferably attached to the mount system, such as to the yoke [57] or to the fuselage, e.g. connecting to the interior surface of an aircraft's fuselage wall [16]. An example of the ASC application with actuators can be found in [15], in which the actuators are integrated in the floor structure to damp the floor vibration. And in some of the ASC applications, the positioning of the actuators is more demanding

than the AVA, e.g. it is stated in [58] that the actuators placed inside a housing specifically built for this purpose along the side of the cabin exterior provide optimal effectiveness in vibration reduction. Generally, ASC systems provide larger dynamic forces, and the operating range is wider than the passive control. They are normally easy to be retrofitted, and there is no safety concern.

1.1.3. Potential improvement

As discussed in Section 1.1.2, passive methods usually suffer the disadvantages of large mass, complex construction, insufficient bandwidth or attenuation, etc. Active techniques provide better solutions in these respects. However, in past studies, the actuation positions of active systems were limited to the fuselage and the mount system, that is, outside the engine and on the very downstream of the vibration transmission path. In these cases, on the one hand, the negative effect caused by the vibration on the upstream cannot be subject to targeted control; on the other, when the vibration is already spread over a structure with complex dynamic behavior, such as over the fuselage, the field of vibration will be complex and hard to deal with. This has led engineers to consider other positions, e.g. on the upstream path, and whether they would be more effective..

When the vibration is caused by the unbalance of the rotor, the main vibration transmission path is shown in a simplified illustration (Fig. 1.1). The double arrows indicate the possibility of actuation, the dotted arrows represent the vibration flow originating from the rotor, and the circles are the connecting points between different parts of this aircraft engine system. Three segments of the transmission path can be recognized. Originating from the rotor, the vibration will be transmitted through the bearings (1) into the core engine. The engine housing is connected to the core engine by supporting parts (2), which constitute the next segment of the path. At last, the vibration enters the fuselage through the mount system (3). Relatively upstream to the mount system and the fuselage are the first two segments inside the engine, (1) and (2). The selection of the actuator positions will be explained in detail in Section 3.2.

The position at the bearing is the closest to the rotor. Aiming at the vibration induced by the unbalance of the rotor, the actuation here would stop or attenuate the vibration directly at the source. A comparatively minor control effort would be expected to yield good effectiveness not only for the fuselage but also for the inside of the engine. The positions labeled as (2) are connected or close to the junctions in circles between the engine and the mount system (Fig. 1.1). Therefore, the vibration, not only originated from the rotor but also from other sources, would presumably be isolated before being carried over into the mount system, and the dynamic loading of the mount system could be reduced. Therefore, less control cost and vibration reduction in more parts of the whole system should be expected with the active control technique applied close to the vibration source. This research has set its goal as confirming these assumptions and discovering further advantages and/or disadvantages of these actuation approaches.

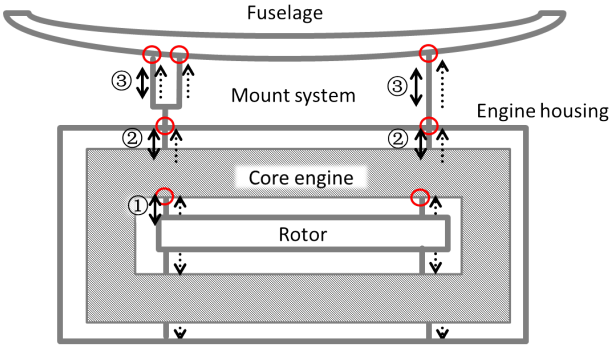

Figure 1.1.: Simplified illustration of vibration transmission path

1.2. Scope of research

In Section 1.1, the focus of the research has been narrowed down to the improvement of the vibration-related comfort. In this section, the scope of the research will be further elaborated based on the assumptions and research resources.

Research object A common type of jet engine, a twin-spool engine with a low pressure rotor (LPR) and a high pressure rotor (HPR), is taken as our investigation object. The relevant fundamentals about this type of engine will be introduced in Chapter 2. All the research is based on a validated finite element (FE) model of this type from Rolls-Royce Deutschland, in which the main mechanical structural characteristics are included. The composition of the model and its features will be presented in Chapter 3.

Targeted problem This work will consider the vibration caused by the unbalance of the rotor, which is the main vibration source. The LPR can be balanced after the assembly of the engine, while the unbalance of the HPR cannot be dealt with, because it is not accessible after the assembly of the engine [42]. Therefore, only the vibration due to the unbalance of the HPR is targeted in this research.

Approaches to be studied Two actuator placement approaches inside the engine (see the positions labeled as (1) and (2) in Fig. 1.1 and Section 3.2 for detail) were raised as the research focus. Since current practice encompasses the passive application with SFDs and the active solution with active mounts (3), they should be also studied on the same system and compared with the other new approaches as benchmarks.

Aim and tasks The aim of this research is to discover the advantages and disadvantages of the passive and active vibration reduction methods with different actuator placement approaches. Said investigation will use the following factors as yardsticks in its analysis: The reduction level, the parts in which the reduction is effective, the control algorithm applicable to each actuation approach and its implementation. The purpose is to make a proposal of an active vibration reduction method applied on the engine for comfort improvement. The tasks to reach the goal are listed below:

1. As a simulation-based study starting from a validated model, a working procedure should be developed to come to reliable conclusions.
    a) Model generation: To find a method to generate such models on

the basis of the FE model that either passive or active vibration reduction methods can be applied. The control algorithm should be able to be integrated in the model of the active system.

b) Evaluation: To select criteria to evaluate comfort and vibration.

c) Effectiveness: To find out the reduction level in terms of the selected criteria with each approach based on the generated models.

2. The results generated through the above working procedure should be organized and analyzed to answer the following questions:

   a) To what extent can the current approaches reduce the vibration?

   b) Under what conditions, e.g. based on which control algorithm, can the proposed actuator placement approaches yield a better performance than the current applications?

   c) How different are the reduction levels with these actuation approaches?

   d) Where does the difference come from? How does each actuation approach influence the whole system?

3. A feasibility study should be carried out as a basis as suggestions for the implementation on the engine in the future.

1.3. Structure of research

Aiming at comfort improvement through vibration reduction, it was decided to use active methods, in which actuator placement and control design were involved. Based on the evaluation of these two aspects, the mechanism of the active systems was discovered and the implementation issues were clarified.

According to the structure of the project, the thesis is arranged as in Fig. 1.2. Chapter 2 starts with the relevant fundamentals about aircraft engines and the unbalance as vibration source. Several evaluation criteria from standards and past studies will be reviewed. As the state of the art, with respect to the application, the current techniques for vibration reduction in the aircrafts will be introduced, while with respect to the research, the

evaluation methods for actuator placement and control design in past studies will be compared.

In Chapter 3, the aforementioned potential actuator positions will be first described in detail. The original FE model will then be introduced, and the working flow to generate models for further study will be explained, including the theory behind each step. The models and validation results will be presented last.

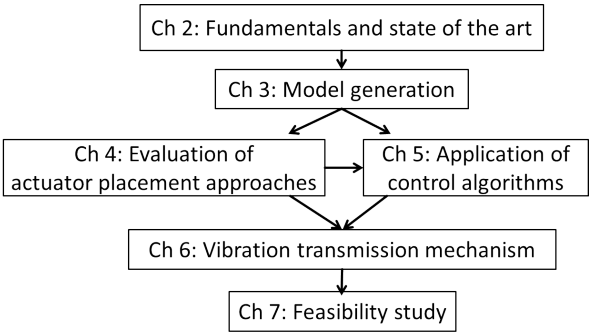

Figure 1.2.: Structure of the thesis

Based on the exploration of the state of the art in Chapter 2, an optimization method was employed to study the ideal effectiveness in the frequency domain. The adaption of this method to the aircraft engine and the results will be presented in Chapter 4. To realize the effectiveness, several control algorithms are selected and adapted to the large complex aircraft engine system. The relevant control theories and results will be shown in Chapter 5. The mechanism in the different active systems will be explained in Chapter 6, based on the results and comparisons with past studies.

Chapter 7 will give an overview how the actuator placement and control strategies can be implemented in the real world to verify the results of the proposed actuator placement approach.

In Chapter 8, the essence of the work and its main conclusions will be summarized, and future research directions will be suggested.

2. Fundamentals and state of the art

This chapter will at the beginning focus on introducing the relevant information on aircraft engines and the vibrations therein, so as to allow a better understanding of the research. Then the evaluation criteria will be discussed, for they are to be used to assess the effectiveness of the actuator placement approach and to decide which sensor signals should be fed into the controller. Given a basic knowledge of the engine, the state of the art of the vibration reduction techniques for aircraft will be elaborated in detail. In the end, the current methods to study the performance of vibration reduction will be reviewed regarding two respects: Evaluation of actuator placement approaches and control algorithms.

2.1. Introduction of jet engines and the vibration cause

Modern passenger aircraft are mostly powered by jet engines. The jet engine applies Newton's third law of motion by forcing a fluid, whether liquid or gaseous, in one direction so as to create an equal reaction, namely, a thrust, propelling the engine and the vehicle it is attached to in the opposite direction [56]. According to this working principle, the air through the jet engine is compressed, combusted and expanded to generate the thrust. Corresponding to these three stages, the core engine consists of three main parts: Compressor, combustor and turbine.

According to the type of compressors, jet engines can be categorized into the following groups: Centrifugal flow and axial flow. The centrifugal flow compressor works by compressing the air perpendicular to the longitudinal axis of the machine and the axial compressor parallel to the longitudinal direction. The axial flow compressor engines are able to handle large volumes

of airflow and high pressure ratios [55]. Among the axial flow compressor engines, the turbofan finds wide use in aircraft propulsion. Many turbofans have a basic twin-spool configuration (Fig. 2.1), where the HP compressor is driven by the HP turbine on the HPR (i.e. the HP spool in purple), and both the fan and the LP turbine (i.e. the LP spool in green) are mounted on the LPR, running concentrically with the HP spool. The turbine drives the compressor on the same spool.

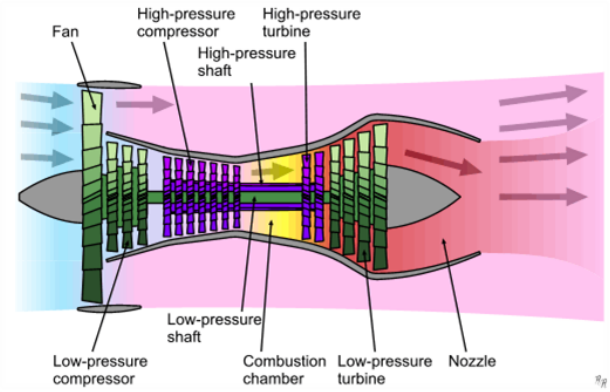

Figure 2.1.: Components of a jet engine [1]

In this research, a reference model of an engine with twin-spool configuration is used. The HPR is supported by bearings 3 & 4 (indicated as B3 & B4 in Fig. 2.2) and the LPR by bearings 1, 2 & 5 (indicated as B1, B2 & B5 in Fig. 2.2). Bearings 1, 2 & 3 are located in the front part ahead of the combustor chamber, that is, the cold-air area, and bearings 4 & 5 are in the rear where the air heated by combustion passes. The compressors, combustor and turbines, as the core engine, which is connected to the engine housing by struts in the front and links in the rear. The casing in which these struts are located in the front is called the intermediate casing (IMC), which supports both the HPR and the LPR in the front through bearings 2 & 3. In the rear, links in the shape of an 'A' (A-frame) support the core engine, as marked with the green boxes. These struts and links are also the only path for the vibration going from the core engine towards engine housing.

The joints highlighted by the blue circles in Fig. 2.2 are used to mount the engine on the fuselage. They are connected to the front upper link (FUL), the front lower link (FLL) and the rear mounting ring (RMR). They also offer the only path for the vibration to go from the engine to the mount system. As shown in Fig. 2.3, a mount system of a general structure is assumed, consisting of two links in the front connecting the fuselage with the FUL and the FLL (numbered as links 1 & 2), two links transmitting the thrust (as links 3 & 4), and two links in the rear connecting the RMR with the fuselage (as links 5 & 6).

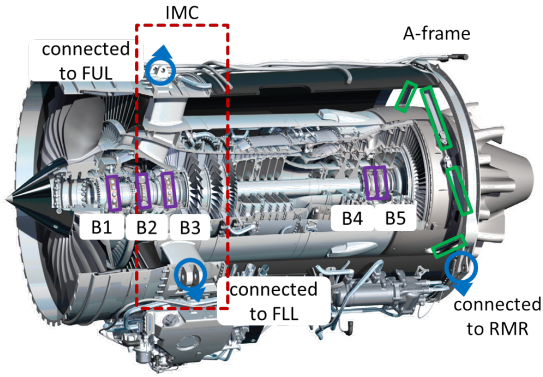

Figure 2.2.: A twin-spool engine [42]

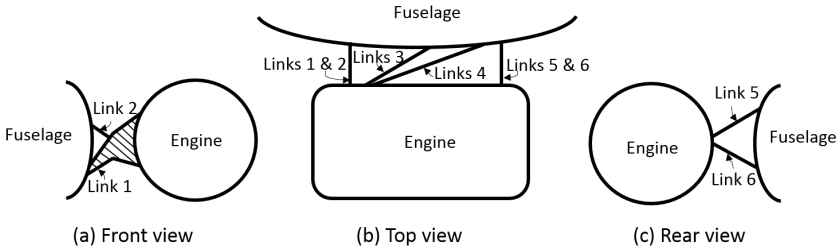

Figure 2.3.: Simplified illustration of the engine mount system

In this research, the unbalance of the HPR is assumed as the vibration cause. Rotors should ideally rotate around the principal axis of inertia. When

the rotation axis, due to the deficiency of production technology or wear, does not overlap the principal axis of inertia, an unbalance appears. As for the engine, the problem of uneven distribution of the HPR cannot be completely avoided during the assembly. And since the HPR is not accessible after the assembly, subsequent corrections with balancing methods, such as are common for the LPR, cannot be implemented either.

The unbalance is quantified by the product of the amount of the mass m which is unevenly distributed and eccentricity ϵ, i.e. the distance between the center of gravity and the center of rotation. The vibration investigated in this research is caused by the force $f_{unbalance}$ generated by the unbalance under the rotational speed of Ω in rad/s:

$$f_{unbalance} = m\epsilon\Omega^2 \tag{2.1}$$

2.2. Evaluation of comfort and vibration

Evaluation of comfort is the basic aspect in this research. Some standard evaluation systems of comfort related to vibration have been established for different vehicles (road, air, rail and marine transport) [35][48] and buildings [12]. Further distinction has been placed on whether people are standing or seated, leading to the development of different criteria with regard to these scenarios, e.g. seat effective amplitude transmissibility index. Most of them are derived from acceleration, which is the most common criterion of comfort. In the mid-1960s, the concept of absorbed power was first discussed as an indicator of human response to whole-body vibration among a number of researchers [50]. While acceleration-based criteria describe the vibration on the vibration surface, the amount of energy (integral of power with respect to time) into the body correlates well to the subjective discomfort according to the experimental results [45]. Apart from acceleration and power, by summarizing the investigation of vibration reduction strategies, it can be seen that transmitted force also plays an important role in the vibrating system. The evaluation criteria developed from these three variables will be listed below.

Criteria based on acceleration [49]

The criteria based on acceleration have been standardized by International Standard ISO 2631 (1997). The root-mean-square value (RMS) of the weighted acceleration a_w during T seconds (Eq. (2.2)) is suggested when subjects undergo periodic whole-body vibration, which is the vibration transmitted to the human body as a whole, due to the vibration of a surface supporting the body [48]. In the time domain, the weighted RMS acceleration is expressed as:

$$a_{rms} = \frac{1}{T}\left[\int_0^T a_w^2\,(t)\,dt\right]^{1/2} \tag{2.2}$$

At a measurement point p, the comfort criterion can be calculated from the RMS values in Eq. (2.2) in each direction:

$$a_p = \left(k_x^2 a_{px}^2 + k_y^2 a_{py}^2 + k_z^2 a_{pz}^2\right)^{1/2} \tag{2.3}$$

where a_{px}, a_{py} and a_{pz} are RMS values of the weighted accelerations in x, y and z directions, k_x, k_y and k_z are weighting factors.

Another criterion, vibration dose value (VDV), accumulates the fourth power of acceleration as shown in Eq. (2.4) and therefore is more sensitive to shocks.

$$VDV = \left[\int_0^T a_w^4\,(t)\,dt\right]^{1/4} \tag{2.4}$$

Since this research is focused on the comfort influenced by the vibration from the HPR unbalance, shocks are not of concern, and thus the RMS value will be used as the criterion based on acceleration (Eq. (2.3)). The RMS value at several points can be derived in a similar way, as shown in Eq. (2.5).

$$a_n = \left(k_1^2 a_{p1}^2 + k_2^2 a_{p2}^2 + \cdots + k_n^2 a_{pn}^2\right)^{1/2} \tag{2.5}$$

where a_{p1}, a_{p2}, $\cdots$, and a_{pn} are RMS values of weighted accelerations at n points, k_1, k_2, $\cdots$, and k_n are weighting factors for each degree of freedom (DOF).

Criteria based on power [3]

The mechanical power exerted on the object is generally defined as $p = fv$, where f is the external force acting on the object and v is the velocity of the object. In the time domain, it can be immediately applied in order to calculate the transient power at each single time point with f and v. However, f and v cannot simply be replaced by the amplitudes of force and velocity in the frequency domain, for the phase shift between them should not be neglected. Taking both amplitude and phase into consideration, the power in the sinusoidal steady-state at a single frequency can be computed as follows, starting with the complex quantities of force and velocity, denoted as F and V.

Force and velocity can be first converted into the time domain, when the sinusoidal steady-state case is assumed:

$$f(t) = \frac{1}{2}\left(Fe^{j\omega t} + F^* e^{-j\omega t}\right) \tag{2.6}$$

$$v(t) = \frac{1}{2}\left(Ve^{j\omega t} + V^* e^{-j\omega t}\right) \tag{2.7}$$

where j is the imaginary unit, ω is the circular frequency and the superscript * indicates the complex conjugate of that value.

Then the power p can be derived from Eq. (2.6) and Eq. (2.7) as:

$$\begin{aligned} p(t) &= \frac{1}{2} Re\left(F^* V\right) + \frac{1}{2} Re\left(FVe^{j2\omega t}\right) \\ &= \frac{1}{2}|F||V| cos\phi_d + \frac{1}{2}|F||V| cos\left(\phi_a + 2\omega t\right) \end{aligned} \tag{2.8}$$

where ϕ_a and ϕ_d are the addition and difference of the phase angles of force and velocity, respectively.

Eq. (2.8) demonstrates that power can be divided into two components; one is constant, while the other is a function of time at a doubled frequency. The constant represents the time-average value of power P_{av} input into the object, as shown in Fig. 2.4. The average power input depends not only on the amplitudes of force and velocity but also on the difference between their phase angles. When the phase difference is less than 90°, the object will absorb energy; otherwise, the object will emit energy back to the source.

Furthermore, the amplitude of the sinusoidal term is half of the product of the amplitudes of F and V. The shadowed portion above the 0 line in Fig. 2.4 represents the energy entering the object in a period, and the negative shadowed portion stands for the energy returned to the excitation source.

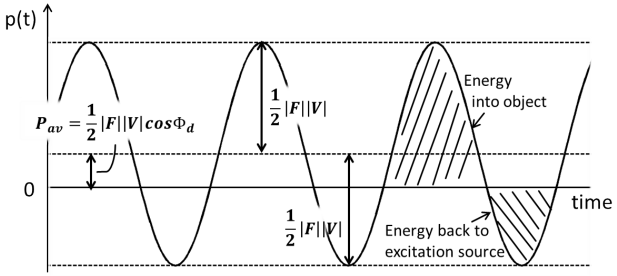

Figure 2.4.: Instantaneous power as a function of time

Borrowed from the concept in electrical engineering, the complex power $\bar{P}$ is defined as:

$$\bar{P} = \frac{1}{2}F^*V = P_{av} + j2\omega\left(U_{av} - T_{av}\right) \tag{2.9}$$

where U_{av} and T_{av} are the average potential and kinetic energies [3].

The real part, equal to P_{av}, is also the power absorbed by the object, and the value in the imaginary part, called the reactive power in the electrical research field, reveals to which extent the excitation source is called upon to participate in the exchange of stored energy.

Moreover, power, as a scalar, allows describing the dynamics of the system in a consistent manner. For example, to evaluate the vibration transmitted into a body through several suspensions, the vibration described by power through different DOFs at a particular or several positions can be summed up.

Criteria based on force

Vibration is the reflection of the energy dissipated in a mechanical system, normally induced by external forces. In past studies, although force is not directly used as a standard criterion to describe comfort, it has frequently

served as the sensor signal and fed into the controller. When the force within the suspension link is zero, then no vibration will pass further into the downstream body. Hence, force should also be taken into account in the evaluation of vibration transmission.

In Fig. 2.5, assuming that the vibration travels from *body A* to *body B* through *body X*, the force applied by *body X* on *body B* at *point b*, i.e. the internal force of *body X*, should be considered to evaluate the transmitted vibration, under the condition that *body X* is connected only with *body B* at *point b*, i.e. no other substructure bears the force from *body X* at *point b*.

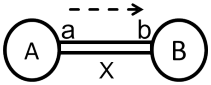

Figure 2.5.: Simple illustration of transmitted force

According to Hooke's law, the internal force of a spring can be calculated as the product of stiffness and relative displacement between the two points. In a vibrating system, it is worth noting that the dynamic stiffness K_{dyn} should be used rather than its static counterpart K_{st}, which depends only on the material and geometry. In dynamic analysis, the forces in the time domain ($f(t)$) and in the frequency domain ($F(\omega)$) are worked out as in Eq. (2.10) and in Eq. (2.11). The dynamic stiffness can thus be extracted from Eq. (2.11), as shown in Eq. (2.12).

$$f(t) = M\ddot{x}(t) + D\dot{x}(t) + K_{st}x(t) \tag{2.10}$$

$$F(\omega) = (-\omega^2 M + j\omega D + K_{st})X \tag{2.11}$$

$$K_{dyn}(\omega) = -\omega^2 M + j\omega D + K_{st} \tag{2.12}$$

where M and D are mass and damping matrices, x and X are the displacement in the time and frequency domains, respectively. The dynamic stiffness is determined by mass, damping, static stiffness and frequency. In the time domain, the internal force can be directly calculated from acceleration, velocity and displacement. Therefore, the calculation of the dynamic internal

force, either in the time or in the frequency domain, requires all the structural information of *body X* and all the motion information of *point a* and *point b*.

2.3. State of the art

The state of vibration reduction techniques applicable to aircraft engines has been discussed in Section 1.1.2 before making suggestions of potential improvements (Section 1.1.3). Here, the applications which have been employed in the market will be elaborated. They will also be compared with the proposed methods as benchmarks in this research.

The research is mainly divided into two parts: Evaluation of actuator placement approaches and control design. The evaluation part will feature comparisons of a number of methods, one of which will serve as the primary focus of this investigation, considering its advantages in large and complex systems. A wide selection of books has been written, presenting many varieties of control design methods. Here the control algorithms which have been applied successfully on large rotating machines will be discussed.

2.3.1. Applications of vibration reduction techniques

Both the engine manufacturer and the mount system provider have striven to improve the comfort inside the fuselage by reducing vibration inside the engine by applying SFDs and by isolating the vibration from the engine by actuating the mount links, respectively.

Passive application: Squeeze film dampers

A typical SFD configuration is presented in Fig. 2.6. Outside the rolling-element bearing is the journal, which is prevented from spinning with an anti-rotation pin or a squirrel cage that forms a centering spring. The squeeze film, normally less than 0.250 mm, is pressurized into the space between the journal and the housing. The lubricant is displaced to accommodate the motion of the journal due to dynamic forces, that is, the reaction forces on the journal generated by the hydrodynamic squeeze film pressures attenuate the

transmitted forces and reduce the amplitude of the rotor motion [2]. SFDs have been employed successfully for many years to manage the vibrations of gas turbine rotors [14].

Generally, SFDs are lubricated elements serving as viscous damping in mechanical systems. When they are used around the bearings in rotating machinery, they can provide structural isolation, attenuate the amplitudes of the response of the rotor to the unbalance at certain frequencies and in some instances assist to suppress rotordynamic instability.

This passive solution will be used as the benchmark in the discussion in the following chapters.

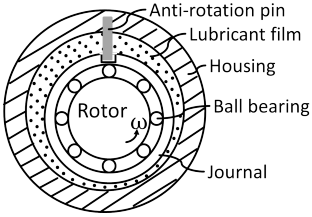

Figure 2.6.: SFD configuration

Active application: Active mounts

The active system developed by Lord Corporation is taken as an example. It consists of actuators, sensors and a controller. Electromechanical actuators are located directly on the vibration path from the engine to the structure They are driven by a central controller to generate counter-acting forces, aiming to cancel the vibration before it arrives at the structure. Microphones located in the cabin provide the controller with information about the noise reduction performance. Reference signals, such as engine vibration signals and tachometer signals, are also fed into the controller. Its design is based on the classic time-domain filtered-U algorithm. They have been certified by Lord Corporation for the McDonnell Douglass DC9/MD80 series.

This approach will be referred to as the active external suspension (ActEx-Sus) approach in this study and be compared with the two proposed active approaches, which are introduced in detail in Section 3.2.

2.3.2. Evaluation of actuator placement approaches

Controllability, as an important property of a controlled system, represents the ability to move the system to any position with certain manipulations. Different criteria derived based on this principle, such as Gilbert, Kalman [25] and index of the LQR (linear-quadratic regulator) optimal control, have been commonly used to evaluate the positions of actuators. In past years, studies were carried out on the optimization of actuator placement on a simple structure, such as a beam or a plate, targeting the above criteria using different optimization procedures [26]. Their application is limited to structures of simple geometries and features and guarantees that only the first few modes could be well controlled. In addition, some of them are mainly focused on efficient optimization techniques concerning large structures or the parameters of the structures in question [43]. However, these methods are not applicable in this research, for two reasons: On the one hand, the engine is geometrically complicated, and many eigenmodes other than the first few are of interest; on the other, due to the size of the system, the large system matrices could cause not only time-consuming computation but also numerical inaccuracy.

Another group of researchers, e.g. in [17], raised the concept of effectiveness of active control strategies, which represents to which extent the actuation forces can minimize the response of the system to the disturbance. This method is flexible, as different variables, power, velocity, force in any direction, or any combination of them can be chosen to build the cost function. It is generalized as Eq. (2.13) and Eq. (2.14): α, β and γ in Eq. (2.13) are derived from the responses to the disturbance Z_p and to the actuation forces Z_c, and the optimum can be reached by determining the optimized control forces $(F_c)_{opt}$ according to Eq. (2.14). The calculation of this method should be conducted at single frequencies in the frequency domain. The detailed derivation for cost functions of squared acceleration, of squared force and of power can be found in Appendix A.

$$J(\omega) = F_c^* \alpha F_c + F_c^* \beta + \beta^* F_c + \gamma \tag{2.13}$$

$$(F_c)_{opt} = -\alpha^{-1}\beta \tag{2.14}$$

This method has been used to study different active systems. In [33], ac-

tive isolators to isolate the vibration from a rigid body to a thin supporting cylinder shell were theoretically investigated based on this method. In [31], the finite element method was used to predict the performance of an active isolator between a vibrating source and a simply supported beam, and optimal control forces were determined according to this method. In [18], with the same method, different control strategies were applied on the mathematical model of a multi-degree-of-freedom system and compared; comprehensive results yielded an insight into the vibration transmission in active systems.

[34] focused more on experiments: A feedforward controller was applied on a beam rig for vibration control. Using the above method to predict the active control performance presented good agreement with the experimental results. Further experimental investigation in [32] showed different control strategies tested both theoretically and experimentally. Commonly used in simple structures in past studies, the method in question can also work for large complex systems, because the cost function is based on the response of the system and the size of the system is not critical regarding the computation time during the optimization procedure.

In [67], this method was used on a commercial airplane system consisting of an airframe ground test model and an analytical finite element model of the engine. Different combinations of control variables, control forces and engine unbalance configurations were tested, and the primary aim was to judge the use of a minimum number of control variables when shakers near the engine were used. This method is also reliable in the case of large and complicated systems, since it is based on the frequency response of the original system. Accordingly, mathematical errors or inaccuracy due to a calculation of large matrices can be avoided. (see Appendix A for the exact derivation of the optimal value)

In all these studies, different systems (beams or cylinder shells or large airplane systems, with single, multiple or complex suspension) have been involved, comparing theoretical, numerical and experimental results. The aim of using this method was either to find the optimal control forces or to acquire insight of the vibration transmission in the active system or to decide on the optimal control strategy related to the formulation of the cost func-

tion [18] or to minimize the number of sensors for practical installation [67]. The method in question has the advantages of flexibility, reliability and independence of the complexity or size of the system, thus allowing many kinds of investigation towards different aims; however, no investigation has been reported exclusively for the evaluation of actuator placement approaches.

The result J in Eq. (2.13) shows the response of the closed-loop system minimally excited with the help of optimal control forces $(F_c)_{opt}$ under the disturbance F_p. Therefore, the comparison of the results of the optimized closed-loop response reflects the effectiveness of the actuator placement approaches. In this way, this method can be used to evaluate the actuator placement approaches. However, since the minimal response is not achieved through a realizable control algorithm, it is only regarded as the ideal effectiveness. Although the experimental results from an actively controlled beam rig were in good agreement with the optimization results based on this method of the effectiveness of active control strategies in [34], its conclusion from a simple beam system cannot yet be extrapolated to general systems. The achievable effectiveness would be determined with the help of the realizable control algorithm, which will be introduced in the next section.

2.3.3. Control design for vibration reduction in rotating systems

Control design methods have been extensively introduced in many text books and further investigated in many studies. In this section, the scope is narrowed down to those applied on an aircraft engine or similar large rotating systems.

As discussed in the last section, the optimized results and experimental results reach good agreement in a beam system in [34], and in the experiments, a feedforward adaptive control algorithm, filtered-x least mean square (FxLMS), was applied; it was also stated that conventional gradient descent algorithms such as FxLMS would converge towards the global minimum. Considering the state of the art of actuator placement approaches in aircraft systems, it was found that the feedforward adaptive control algorithm was commonly used in the active control systems of helicopters [58] [54]. [46]

revealed that attenuations around 25 dB regarding displacement could be obtained in the numerical simulations of the active vibration control system with FxLMS applied on a fuselage section of an aircraft excited by white noise, and this proved FxLMS as a valid choice for broadband excitation signals. In [63], the feasibility and validity of FxLMS was verified experimentally on an active vibration control system implemented on an aircraft framework. While the studies listed above were focused on the application of FxLMS on the airframe/fuselage, the results of the flight tests in [30] showed that a reduction of up to 19.5 dB could be reached during the cruise with FxLMS implemented on the active gearbox struts. In [6], the time-domain filtered-U algorithm was applied on the active mounts of the aircraft engine, and it was also stressed that the implementation issue needs to be resolved because a potential long-term divergence of the algorithm could be caused by ill-conditioned transfer function matrices. A similar conclusion was drawn in [59], where several control algorithms were investigated on rotor systems: A model of high accuracy would be required to avoid instability when implementing the FxLMS algorithm on a large rotating system.

In [59], algorithms PDT_1, LQG, H_∞ and FxLMS were investigated theoretically and experimentally on a rotor system to reduce the vibration from the unbalance of the rotor, respectively categorized as simple control, optimal control, control in the frequency domain and feedforward control in the time domain. It was found that the optimization of FxLMS was simpler than the others and could bring about the best reduction effectiveness; notably, sensor placement did not have a great effect on the optimization. However, sensor signals were required to represent the global vibration behavior when aiming for global reduction. There was not that much difference in reduction effectiveness based on the three feedback control algorithms as long as sensors were placed suitably. The simple control PDT_1 could bring little reduction effectiveness at both resonances when the sensors were improperly placed. H_∞ was proved to be advantageous when the control design was tuned manually. Moreover, it could be transferred onto complex systems and was verified experimentally, showing that as a model-based algorithm, its requirement of the accuracy of the model was not so strict as FxLMS. It was

recommended that a LQG should be considered when the manually tuned H_∞ was not sufficient in reduction, because a LQG had small sensitivity to sensor placement.

[61] presented a comprehensive study of active noise control (ANC) and active vibration control (AVC) in aircraft systems. According to the study, most ANC systems employed an LMS algorithm, such as the FxLMS, and that the basic principles of ANC could be applied to AVC. It was also pointed out that the majority of customized control programs for AVC systems were based on the Linear Quadratic Gaussian (LQG) algorithm. An active strut member was shown to decrease vibration levels by 35 dB using a positive position feedback (PPF) controller. Moreover, since the simulation results of the H_∞ controller applied on the airframe of helicopters showed a significant decrease in vibration, parts of the theory were thus experimentally shown to work.

In [7], the integral feedback force (IFF) was applied on the active bearing of an aircraft engine, with the stability as the advantage of this algorithm proved numerically and experimentally. It also showed that the model-based feedforward control performed better than the IFF but the stability could not be ensured. The study suggested that the feedforward control should be used for the vibration reduction and the IFF as an emergency system.

In summary, the effectiveness of all sorts of control algorithms used for vibration reduction in aircraft systems was investigated numerically and experimentally. Some algorithms proved advantageous, others disadvantageous regarding implementation or stability issues. It can be seen that the feedforward adaptive algorithm has been studied the most for active vibration control in aircraft systems. On the one hand, it showed promise regarding its reduction effectiveness and flexibility; on the other hand, the issue of divergence and instability should be taken into account during implementation. Moreover, there were a number of in-depth studies on controlling the vibration from rotor unbalance [59], while others dealt with broadband excitation as a vibration source [46]; yet others focused on either the control design for active systems applied outside the engine [58] [54] [30] [6] or those applied inside the engine [59] [7].

Accordingly, investigations in the past found methods to design controllers and/or suitable controllers for certain cases, some also providing suggestions for their implementation. In this project, some of these controllers were selected to be used for the vibration reduction in certain cases, i.e. with different actuator placement approaches (see Section 3.2 for detail): on the engine mounts, on the struts inside the engine and at the bearing. The control design for the active system on the struts inside the engine is new, because this actuator placement approach is innovative, while the positions on the engine mounts and at the bearing have been studied, as listed above. Therefore, the similar application in this project allows its results to be compared with and verified by the results in those past studies.

3. Model generation

An FE model of the whole engine built in the finite element analysis program Nastran served as the starting point. This chapter will propose the new actuator placements, before introducing the model generation procedure in order to facilitate the investigation of these approaches. Employing a controller on a large FE model is possible but limited regarding the controller type [28] and the computational efficiency [65]. For an efficient examination of the actively controlled engine, it is necessary to reduce the model and generate the state space (SS) model, allowing a more flexible control design. The working flow to generate SS models and the relevant background will be elaborated subsequently. To prove the reliability of this model generation method, the validation results will then be presented according to different criteria. The current chapter will close by explaining the uses and different characteristics of the generated models.

3.1. Introduction of the whole engine model

As shown in Fig. 3.1, the whole engine model (WEM) consists of a twin-spool engine with an HPR and an LPR (see Fig. 2.1 for the components of the engine), a section of the fuselage and the engine mount system (MNT), connecting the first two parts. This model allows taking into consideration the dynamic characteristics of the engine, the suspension and the fuselage section related to unbalance excitation and includes the structures which form the vibration transmission path. It has originally $34,872$ elements and $35,519$ nodes. Six DOFs have been assigned to most of the nodes and three translational DOFs to the rest of them. Therefore, there are approx. 2 million DOFs in the WEM, which should be reduced for computational efficiency.

From the forward direction indicated in Fig. 3.1, it can be inferred that

this is the model of a left-hand engine. In the following study, for simplicity, it is assumed that the structure, the unbalance excitation and the actuation in the right-hand engine, which is not included in the model, are identical to the left-hand engine. Therefore, the rim of the fuselage section in this engine model is fixed as the boundary condition, due to the symmetric structure and symmetric boundary condition.

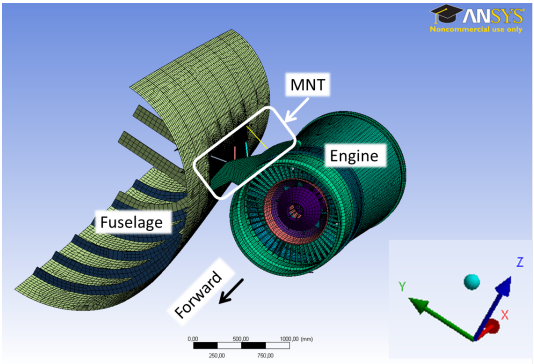

Figure 3.1.: WEM colored according to the type of material

The first five eigenfrequencies of each part of the WEM and the WEM as a whole listed in Table 3.1 show the comparable stiffness of each part, compared with the other parts, and how the eigenfrequencies are shifted when they are constructed as a WEM. According to a general statement in [66] for a suspension system consisting of a machine, a vehicle and mounts, the machine (corresponding to the engine here) is ordinarily much stiffer than the vehicle (the fuselage), and the mount is in-between both of them with respect to rigidity. However, the starting eigenfrequencies of the fuselage here are higher than those of the engine and the mount. The reason for this disagreement with the theory is that only a section of the fuselage is included in the WEM. It is much smaller and not characterized by a low-frequency behavior. But it is sufficient for this study, as it is mainly focused on the high-frequency excitation of the rotor unbalance. The first four eigenmodes of the WEM belong to the MNT, because there is no deformation of the engine and fuselage in these mode shapes. Accordingly, the engine and fuselage can be

regarded as rigid bodies for these frequencies. The deformation of the engine begins to take effect starting with the fifth eigenmode. Since this study is designed for the high-frequency range, all these three parts must be regarded as flexible bodies, and none of them should be simplified as a rigid body. This fact is one of the reasons for the necessity of model reduction (Section 3.3).

(in Hz)	Engine	MNT	Fuselage	WEM
1	20.33	10.91	48.61	6.33
2	28.64	13.35	65.73	8.71
3	31.38	17.39	95.52	15.22
4	33.13	30.68	95.69	19.43
5	34.54	56.65	97.71	24.01

Table 3.1.: First five eigenfrequencies of the original WEM

3.2. Proposed actuator placement approaches

Considering the limited space inside the engine and along the main vibration transmission path, it has been learned that the space 1) at the bearing, 2) inside the hollow struts within the intermediate casing and 3) around the A-frame links in the rear shows good potential as actuator positions [42], corresponding to segments 1, 2 (front) and 2 (rear) on the transmission path in Fig. 1.1.

Active internal suspension

The position and the role of the struts in the IMC are illustrated in a front view of IMC (Fig. 3.2a). The engine mount system holds the engine in the front through the FUL and the FLL. The two struts immediately underneath these two links are hollow, while the other struts are occupied by supply lines for lubricating oil, SFD, sensor units and so on. They are connected sequentially with the bearing chamber of bearings 2 and 3 (see also Fig. 2.2). They are thus responsible for passing on the force from the front bearings. Bearing 3 carries the vibration from the HPR unbalance, wherefore these struts inside the IMC are on the main vibration transmission path.

Fig. 3.3 shows the cross-section A-A (Fig. 3.2a) of the original and modified sketch of the hollow strut underneath the FUL and FLL. To support the actuation, a stiffener can be constructed crosswise inside the strut (see the right hand side in Fig. 3.3). The double arrows in Fig. 3.2 & 3.3 indicate the actuation of actuators. One end of the actuator is attached to the supporting structure and the other end to the engine housing collocated with the FUL and the FLL. The supporting structure should be stiff enough, so that the actuation force effects on the side of the junction to the mount system.

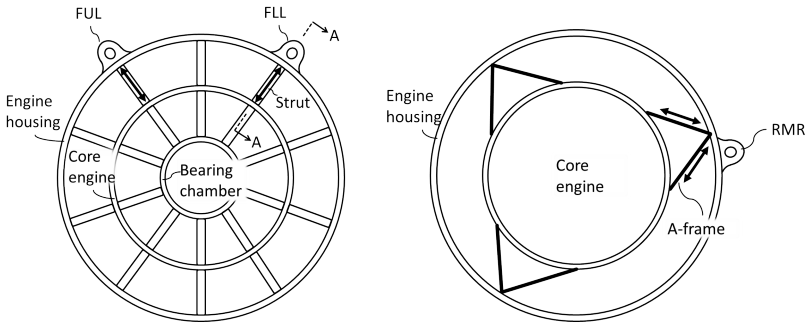

(a) Front view of IMC **(b)** Rear view of A-frame

Figure 3.2.: Actuator placement in the approach of active internal suspension

The front active application can be reinforced by also actuating the rear part. Fig. 3.2b shows the rear view of the A-frame. Unlike the front struts, there is no hollow structure in the rear to directly house the actuators. But they can be attached to the links inside the engine as the arrows indicate, connecting the engine housing with the core engine, close to the RMR. One of the applications of the piezoelectric actuators attached to links is patented under the title 'piezoelectric extension actuator' [4] and will be introduced in the feasibility study (Chapter 7).

This approach is called active internal suspension (ActInSus), because it actuates the inside suspension between the engine housing and the core engine. Its goal is to reduce the vibration at the front and rear links of the mount system on the engine side and eventually at the fuselage. Its advantages lie in smaller mass increase and wider operating range, compared with

the passive methods, and also maintains the benefits of earlier control of the vibration, compared with other existing active methods. No additional safety issues are triggered by this parallel configuration both in the front and the rear, and the case of overload is of no concern.

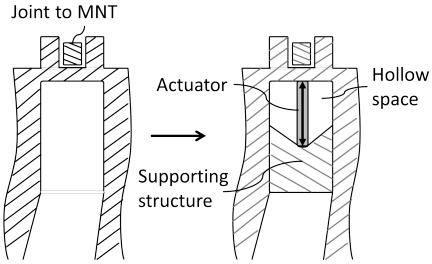

Figure 3.3.: Left: Original strut in IMC; Right: Strut in IMC with actuator installed

Active bearing

With the help of a CAD analysis of the engine components (Fig. 3.4), the front bearing chamber (FBC) was identified as the appropriate space for the actuators. Taking this illustration as example, bearings 2 and 3 (their structures are not shown in detail, and only their positions are indicated) are encompassed in the FBC and the FBC is partly surrounded by the IMC (see also Fig. 2.2 for the corresponding positions of these components in the engine). The hollow space in the strut of the IMC is available for placement. In other words, part of the actuator can protrude into the strut. The actuation force can be transmitted through the common bearing chamber of bearings 2 and 3, influencing the vibration both on the HPR and on the LPR. The other end of the actuator should be attached to a stiff support in the strut of the IMC. The cooling system will be explained in Chapter 7.

An alternative implementation only targets influencing bearing 3. In such an application, the bearing chamber should be drilled so that the actuator can directly exert force on the squirrel cage (SC) of bearing 3, rather than the common bearing chamber of bearings 2 and 3. Additionally, the contact face on the SC should be thus sufficiently stiffened to support the effective

actuation. The other end of the actuator should be positioned and affixed as described above.

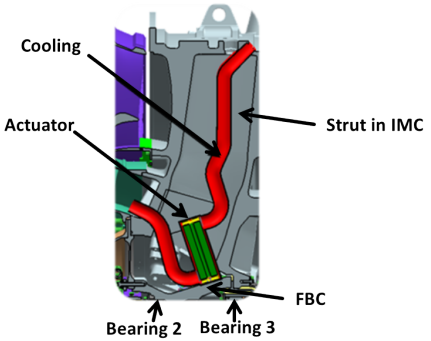

Figure 3.4.: Possible position in a twin-spool engine for the active bearing approach [42]

Actuators placed at the rear bearing were not proposed, due to its surrounding of high temperature. The detailed discussion and the description of the identified possibility of a cooling system in Fig. 3.4 can be found in the feasibility study (Chapter 7).

Generally, it would be expected that the active system at the bearing of the HPR, abbreviated as ActBrg, could reduce the vibration not only in the fuselage but also inside the engine, due to its effect on the vibration source.

3.3. Generation method of state space models

Different models are to be generated on the basis of the WEM introduced above, as necessary for the study of passively and/or actively damped systems. Also considering the necessity of model order reduction and the capability to integrate the control algorithm, the model generation method has been developed as shown in Fig. 3.5.

The procedure starts with two types of files from Nastran and goes respectively through two series of procedures, until the stiffness and mass matrices are obtained. These are documented for the future study which requires a similar model conversion. The common input file (*.dat or *.bdf) of Nastran

can be transferred into an *.inp file which can be further imported into ANSYS for model reduction and matrix extraction (Section 3.3.1). Meanwhile, matrices can be directly extracted from the matrix file *.mtx without being imported into ANSYS (see Appendix B for the detailed procedures).

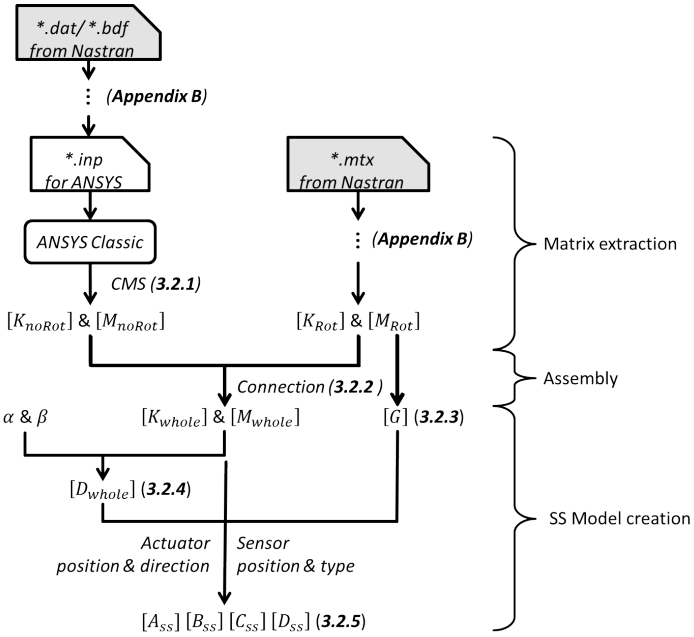

Figure 3.5.: Working flow to generate state space models

As for this model, the non-rotating part (the engine without rotors, the MNT and the fuselage) is saved in the *.inp file, and the *.mtx files representing the rotating parts (HPR and LPR) were generated through static model reduction and validated by the partner company. The extracted matrices are denoted as $[K_{noRot}]$, $[M_{noRot}]$ and $[K_{Rot}]$, $[M_{Rot}]$, respectively. It is mentioned here as a general note that the matrices generated from ANSYS are in the Harwell-Boeing format and can be converted into a full matrix with MatLab functions [8]. The non-rotating and rotating parts can be connected through different bearing configurations (Section 3.3.2). Due to the presence of rotors, the gyroscopic effect should be included in the form of

a gyroscopic matrix $[G]$, which can be created from the moment of inertia of the rotors (Section 3.3.3). Structural damping is defined in this case as being proportional to mass and stiffness, although also permitting other definitions (Section 3.3.4). In the final step, the SS model can be produced with the system information in the form of matrices as described above and the user-defined settings according to the scenario, that is, the selection of the actuator position and direction as well as the sensor position, direction and type (Section 3.3.5).

3.3.1. Model reduction and matrix extraction

Model reduction - CMS

In [40], different model reduction techniques were compared for large mechanical systems, and it was concluded that Component Mode Synthesis (CMS) promises good correlation for high frequency motion. Therefore, the CMS method was selected as the model reduction technique in this study. It reduces the system matrices to a smaller set of master DOFs between substructures and truncated sets of normal mode generalized coordinates [11].

To apply CMS, all the DOFs are divided into two groups: Master DOFs (the DOFs whose physical motion are required to be observable) and slave DOFs (the interior DOFs which should be reduced and estimated by the physical coordinates of master DOFs and the truncated set of modal coordinates). They are assigned the subscripts m and s. The undamped system can be expressed as:

$$\begin{bmatrix} M_{mm} & 0 \\ 0 & M_{ss} \end{bmatrix} \begin{Bmatrix} \ddot{x}_m \\ \ddot{x}_s \end{Bmatrix} + \begin{bmatrix} K_{mm} & K_{ms} \\ K_{sm} & K_{ss} \end{bmatrix} \begin{Bmatrix} x_m \\ x_s \end{Bmatrix} = \begin{Bmatrix} F \\ 0 \end{Bmatrix} \quad (3.1)$$

where x and F denote the displacement vector of all the DOFs and the external force vector applied on the system, respectively.

Assuming that $\ddot{x}_s = 0$, i.e. the movement of slave DOFs is considered as static, then

$$K_{sm}x_m + K_{ss}x_s = \{0\} \quad (3.2)$$

$$x_s = -K_{ss}^{-1}K_{sm}x_m \quad (3.3)$$

Assuming that $x_m = 0$, i.e. master DOFs are fixed, then

$$M_{ss}\ddot{x}_s + K_{ss}x_s = \{0\} \tag{3.4}$$

The solution of x_s in Eq. (3.4), denoted as ϕ_s, represents the normal modes of slave DOFs when the master nodes are fixed.

Combining Eq. (3.3) and a truncated set $\phi_{s\delta}$ of ϕ_s, the transformation between original and reduced coordinates can be expressed as:

$$\begin{Bmatrix} x_m \\ x_s \end{Bmatrix} = \begin{bmatrix} I & 0 \\ -K_{ss}^{-1}K_{sm} & \phi_{s\delta} \end{bmatrix} \begin{Bmatrix} x_m \\ y_\delta \end{Bmatrix} \tag{3.5}$$

where y_δ is a vector of the truncated set of generalized modal coordinates.

This is the transformation used in the CMS method. The reduced order depends on the truncation of ϕ_s, i.e. the number of columns of $\phi_{s\delta}$. The truncation is determined by the frequency range to be considered.

Replacing the coordinates in Eq. (3.1) with Eq. (3.5) allows the reduced system to be written as:

$$\begin{aligned} &\begin{bmatrix} M_{mm} & 0 \\ 0 & \phi_{s\delta}^T M_{ss}\phi_{s\delta} \end{bmatrix} \begin{Bmatrix} \ddot{x}_m \\ \ddot{y}_\delta \end{Bmatrix} \\ &+ \begin{bmatrix} K_{mm} - K_{ms}K_{ss}^{-1}K_{sm} & 0 \\ 0 & \phi_{s\delta}^T K_{ss}\phi_{s\delta} \end{bmatrix} \begin{Bmatrix} x_m \\ y_\delta \end{Bmatrix} = \begin{Bmatrix} F \\ 0 \end{Bmatrix} \end{aligned} \tag{3.6}$$

For this study, the nodes which may potentially serve as positions for actuators and sensors as well as the interface nodes between the substructures of rotors, engine, MNT and fuselage are defined as master nodes. The HPR unbalance is the disturbance source to be investigated. The maximum rotational frequency is 260 Hz at the take-off phase. By experience, to ensure the accuracy of the model up to a certain frequency, the truncation frequency should be at least 2-3 times as high as this frequency. Therefore, the frequency range of $0 - 600$ Hz was set for the truncation of the normal modes of slave DOFs for this investigation.

3.3.2. Bearing configurations

The installation of actuators attached in parallel to the mount links [36] or to the stiff struts inside the engine can hardly change the structural integrity of

the system, due to the high stiffness of the links and struts, while the SFDs and actuators installed at the bearings can indeed alter system behavior, because of their low stiffness and/or the serial connection. Therefore, five models with five types of bearing configurations were generated. Fig. 3.6 shows the configurations of bearing 3 which is available for both SFDs and actuators. The settings of the other bearings where only SFDs should be introduced can be found in Tables 3.2 & 3.3. The models of SFDs are simplified and linearized as parallel springs and dampers, and actuators are added as springs.

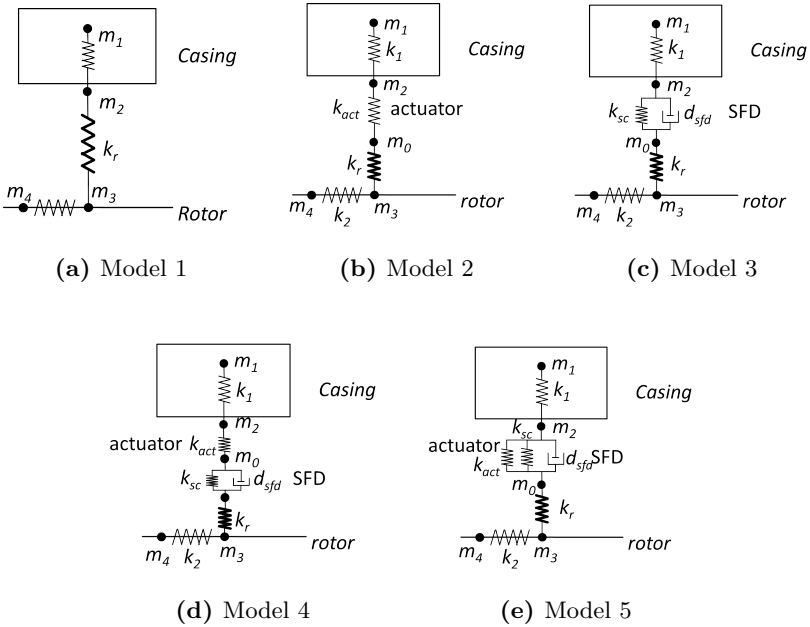

(a) Model 1 **(b)** Model 2 **(c)** Model 3

(d) Model 4 **(e)** Model 5

Figure 3.6.: Five configurations of bearing 3

1. quasi-rigid connections
2. actuators applied
3. SFDs applied
4. SFDs and actuators applied in series
5. SFDs and actuators applied in parallel.

Here the casing indicates the non-rotating part of the engine. $m_1 - m_4$ represent the masses of the interface nodes on the casing, the bearing and the HPR, and m_0 and m_{01} the masses of an additional node due to the introduction of the SFD and/or the actuator. k_r, k_{act} and k_{sc} are the stiffnesses of the quasi-rigid bearing, the actuator and the SC, respectively. k_1 and k_2 are the stiffnesses of the boundary element on the casing and the HPR, respectively. d_{sfd} is the damping of the SFD.

In Model 1 and Model 3, no actuator is installed at the bearings. The connections at the bearings in Model 1 are rigid, and there is no SFD. This will be called a dry case in the following discussion. Model 3 is a reference model since it represents the state of the current engine: Passive damping with SFDs. The other three models have actuators in two perpendicular directions to the rotation axis at bearing 3, the front bearing of the HPR. Model 2 is obtained by introducing actuators in the dry case, and Model 4 and Model 5 in the reference case. The difference between Model 4 and Model 5 is: In Model 4, the SFD and the actuators are serial and in Model 5 parallel. The connection methods are illustrated and the matrices at the connection point are calculated in Appendix C.

The bearings are all ball bearings, handling both the radial and the thrust load at B1 and B3, which are the most forward bearings of the LPR and the HPR, respectively, but are confined to managing only the radial load at B2, B4 and B5. The stiffness and damping at bearings are listed in Tables 3.2 and 3.3 (proportional damping is not considered here). The values in merged cells are shared by different models and DOFs. None of the models show any difference in the rear bearings (B4 and B5) or in the x-direction (the direction of the rotation axis). The differences in stiffness and damping at B1 and B2 and in damping at B3 are related only to the presence of the SFDs. The stiffness at B3 varies according to the installation and connection method of the SFDs ($k_{sc} = 2.5e4$ N/mm) and actuators ($k_{act} = 2.3e5$ N/mm, see Chapter 7 for the selection of actuators). The quasi-rigid bearings are simulated as springs with the stiffness of $k_r = 1e6$ N/mm.

Stiffness (N/mm)	B1			B2		B3			B4		B5	
	x	y	z	y	z	x	y	z	y	z	y	z
Model 1	1.0e6	1.0e6		1.0e6		1.0e6	1.0e6		1.0e6			
Model 2							1.9e5					
Model 3		5.0e4		0			2.5e4					
Model 4							2.3e4					
Model 5							2.6e5					

Table 3.2.: Stiffness of bearings of the HPR and LPR

Damping d_{sfd} (Ns/mm)	B1			B2		B3			B4		B5	
	x	y	z	y	z	x	y	z	y	z	y	z
Model 1	0	0		0		0	0		0			
Model 2							0					
Model 3		100.0		50.0			50.0					
Model 4							50.0					
Model 5							50.0					

Table 3.3.: Damping of bearings of the HPR and LPR

3.3.3. Gyroscopic effect

Based on the theory described in [47] and the introduction method of the gyroscopic effect in [5], the gyroscopic matrix for this study is generated as follows.

For each stage with 6 DOFs, the gyroscopic effect can be presented as

$$\begin{bmatrix} F_{ugx} \\ F_{ugy} \\ F_{ugz} \\ M_{\theta gx} \\ M_{\theta gy} \\ M_{\theta gz} \end{bmatrix} = \Omega \begin{bmatrix} 0 & 0 & 0 & 0 & 0 & 0 \\ 0 & 0 & 0 & 0 & 0 & 0 \\ 0 & 0 & 0 & 0 & 0 & 0 \\ 0 & 0 & 0 & 0 & 0 & 0 \\ 0 & 0 & 0 & 0 & 0 & -I_x \\ 0 & 0 & 0 & 0 & I_x & 0 \end{bmatrix} \begin{bmatrix} \dot{u}_x \\ \dot{u}_y \\ \dot{u}_z \\ \dot{\theta}_x \\ \dot{\theta}_y \\ \dot{\theta}_z \end{bmatrix} = \Omega G_{stage} \begin{bmatrix} \dot{u}_x \\ \dot{u}_y \\ \dot{u}_z \\ \dot{\theta}_x \\ \dot{\theta}_y \\ \dot{\theta}_z \end{bmatrix} \tag{3.7}$$

where I_x is the mass moment of inertia of each stage about the rotation axis and Ω the rotational speed of the rotor.

The gyroscopic matrix can be formulated for the whole rotor system as

$$G = \begin{bmatrix} \mathbf{0} & \mathbf{0} & \mathbf{0} \\ \mathbf{0} & G_{HPR} & \mathbf{0} \\ \mathbf{0} & \mathbf{0} & G_{LPR} \end{bmatrix} \tag{3.8}$$

where the first rows of zeros correspond to all the non-rotating DOFs, G_{HPR} is generated as in Eq. (3.7) for all the stages of the HPR and G_{LPR} for those of the LPR.

3.3.4. Damping

The damping in the WEM system is simplified and assumed to be proportional damping. Thus the damping matrix consists of structural damping proportional to the mass and stiffness and the damping due to the SFD (see Appendix C for the generation of D_{SFD}).

$$D = \mu M + \eta K + D_{SFD} \tag{3.9}$$

3.3.5. State space model

In the previous steps, mass, stiffness, damping and gyroscopic matrices were respectively calculated for the whole system. The model can be written as

$$M\ddot{x} + (D + \Omega G)\,\dot{x} + Kx = f \tag{3.10}$$

For the further study of the whole system, the model needs to be reconstructed as a state space model. Velocity and displacement constitute the states, and the motions of DOFs of interest are set as the outputs.

$$\begin{Bmatrix} \ddot{x} \\ \dot{x} \end{Bmatrix} = A_{ssm} \begin{Bmatrix} \dot{x} \\ x \end{Bmatrix} + B_{ssm} f \tag{3.11}$$

$$\begin{Bmatrix} x_{out} \\ v_{out} \\ a_{out} \end{Bmatrix} = C_{ssm} \begin{Bmatrix} \dot{x} \\ x \end{Bmatrix} + D_{ssm} f \tag{3.12}$$

where the system matrix is

$$A_{ssm} = \begin{bmatrix} -M^{-1}(D + \Omega G) & -M^{-1}K \\ I & \mathbf{0} \end{bmatrix} \tag{3.13}$$

If the inputs f are forces acting directly on each coordinate of each node, then the input matrix $B_{ssm} = [M^{-1}; \mathbf{0}]$. However, this system was to be built for the analysis of the effectiveness of the actuators in each approach, where actuation forces are applied in an arbitrary direction. B_{ssm} should be formulated so that the forces generated by the actuators can be resolved into x, y and z coordinates, as shown in Eq. (3.14). T_{res1} and T_{res2} are used to resolve the unbalance forces and the actuation forces, respectively.

$$B_{ssm} f = M^{-1} \begin{bmatrix} T_{res1} & T_{res2} \\ \mathbf{0} & \mathbf{0} \end{bmatrix} \begin{Bmatrix} f_{unbalance} \\ f_{act} \end{Bmatrix} \tag{3.14}$$

T_{res1} is different according to the analysis domain. In the time domain, the unbalance force should be exerted along the y and z coordinates (the rotation axis is parallel to the x-coordinate, see Fig. 3.1) at the unbalance position as cosine and sine functions defined by the magnitude of the unbalance and the rotational speed, as shown in Eq. (3.15).

$$T_{res1(time)} f_{unbalance} = \begin{bmatrix} \vdots & \vdots & \vdots \\ 0 & 0 & 0 \\ 0 & 1 & 0 \\ 0 & 0 & 1 \\ \vdots & \vdots & \vdots \end{bmatrix} \begin{Bmatrix} 0 \\ |F_{unbalance}|\, cos(\Omega t) \\ |F_{unbalance}|\, sin(\Omega t) \end{Bmatrix} \tag{3.15}$$

$$T_{res1(freq)}\, |F_{unbalance}| = \begin{bmatrix} \cdots & 0 & 1 & -j & \cdots \end{bmatrix}^T |F_{unbalance}| \tag{3.16}$$

The unbalance affects the system in such a way that the excitation in one coordinate is the same as that in the other coordinate with the lag of 90° in the frequency domain. Thus the transformation matrix can be defined as a real unit and an imaginary unit in one column, as shown in Eq. (3.16). With the minus sign, the excitation in z direction lags behind that in y direction. And this corresponds to the formulation of the gyroscopic matrix in Eq. (3.7). In other words, if the two non-zero elements in the gyroscopic matrix in Eq. (3.7) swap, the minus sign in Eq. (3.16) should be removed.

Assuming that t_{nx}, t_{ny} and t_{nz} are the factors to resolve the n^{th} actuation force into the x, y and z directions, then the transformation matrix for the

actuation forces is

$$T_{res2} \tag{3.17}$$
$$= \begin{bmatrix} t_{1x} & t_{1y} & t_{1z} & -t_{1x} & -t_{1y} & \cdots & 0 & 0 & 0 & 0 & 0 & 0 \\ \vdots & \vdots & \vdots & \vdots & \vdots & \ddots & \vdots & \vdots & \vdots & \vdots & \vdots & \vdots \\ 0 & 0 & 0 & 0 & 0 & \cdots & t_{nx} & t_{ny} & t_{nz} & -t_{nx} & -t_{ny} & -t_{nz} \end{bmatrix}^T$$

The output matrix C_{ssm} and the feedthrough matrix D_{ssm} can be expressed as in Eq. (3.18) and Eq. (3.19). I is the identity matrix, and the subscript *part* denotes that only parts of the rows are selected from that matrix. Without an external force acting on the DOF, its corresponding row of acceleration in D_{ssm} is a row of zeros.

$$C_{ssm} = \begin{bmatrix} \mathbf{0} & I_{part} \\ I_{part} & \mathbf{0} \\ -M_{part}^{-1}\left(D_{part} + G(\omega)_{part}\right) & -M_{part}^{-1}K_{part} \end{bmatrix} \tag{3.18}$$

$$D_{ssmAcc} = \begin{bmatrix} \mathbf{0} & \mathbf{0} & M_{part}^{-1}T_{res_{part}} \end{bmatrix}^T \tag{3.19}$$

The model is designed to measure the motion of observation points and sensor points as well as the internal force in the elements on the vibration transmission path, e.g. at the bearings and in the suspension links (FUL, FLL, RMR and MNT links). When only accelerometers are selected to collect the signals, representing the vibration level and being fed back into the controller, velocity and displacement can be derived from the acceleration in the frequency and time domains, respectively, according to Eq. (3.20) & (3.21) and Eq. (3.22) & (3.23). The displacement and velocity at a discrete time point can be approximated according to the rectangle method at the left-point in the numerical integration or other methods [24]. The force can be derived from these three variables according to Eq. (2.11) and Eq. (2.10).

$$V(\omega) = A(\omega)/(j\omega) \tag{3.20}$$
$$X(\omega) = A(\omega)/(j\omega)^2 \tag{3.21}$$
$$v(t_n) \approx v(t_{n-1}) + a(t_{n-1})\Delta t \tag{3.22}$$
$$x(t_n) \approx x(t_{n-1}) + v(t_{n-1})\Delta t \tag{3.23}$$

where $\Delta t = t_n - t_{n-1}$.

3.4. Model validation

In order to check if this generation method is able to reproduce the model, model validation should be performed. Model 1 was generated with this method and is the state space (SS) representation of the original FE model. The SS Model and the FE model should be compared for validation purposes. Three criteria based on the results from modal analysis, harmonic analysis and transient analysis are used. The criterion based on modal analysis should provide a global indicator of the level of correlation, while the other two are related to certain inputs and outputs. The criterion based on harmonic analysis is dependent on the frequency, while that based on transient analysis in the time domain considers all the frequencies.

3.4.1. Validation based on modal analysis

Modal analysis is used to find the frequencies at which the system naturally resonates and their mode shapes, with the overall mass and stiffness of the structure. Results from the modal analysis are eigenfrequencies and eigenmodes. Fig. 3.7 shows good agreement in eigenfrequencies between two models. However, a good eigenfrequency-correlation does not always imply the analogous eigenvector-correlation. [40]

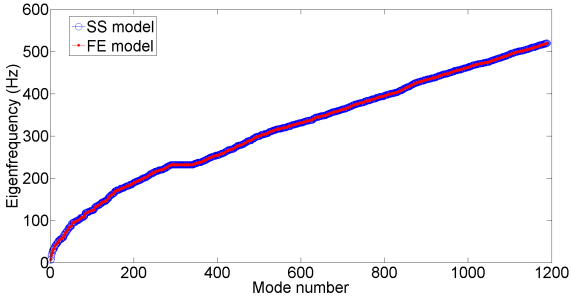

Figure 3.7.: Comparison of eigenfrequencies of the original model and the generated SS model (Model 1)

The modal assurance criterion (MAC) is defined as in Eq. (3.24) [52], to find the correlation between the eigenvectors of two models. V_i^{eig} and $\hat{V}_j^{eig}$

represent the i^{th} and j^{th} eigenvectors of two models. The MAC values range between 0 and 1. The two extremes correspond to the case of orthogonal eigenvectors and that of identical eigenvectors, respectively. In other words, larger values indicate a higher similarity.

$$MAC_{ij} = \frac{\left(\left\{V_i^{eig}\right\}^T \left\{\hat{V}_j^{eig}\right\}\right)^2}{\left(\left\{V_i^{eig}\right\}^T \left\{V_i^{eig}\right\}\right)\left(\left\{\hat{V}_j^{eig}\right\}^T \left\{\hat{V}_j^{eig}\right\}\right)} \tag{3.24}$$

In the calculation of eigenvectors, different formulations can be employed, for example, the two shown in Eq. (3.25) (normalized to unit) and Eq. (3.26) (normalized to mass), where $[V^{eig}]$ is the matrix consisting of all eigenvectors. Using the formulation in Eq. (3.25), it would be expected that all the MAC values generate a matrix approximately equal to the identity matrix when two models are well correlated: The i^{th} eigenvector of one model has a high similarity to the i^{th} eigenvector of the other, and the i^{th} of one model is orthogonal to the j^{th} eigenvector of the other.

$$\left[V^{eig}\right]^T \left[V^{eig}\right] = I \tag{3.25}$$

$$\left[V^{eig}\right]^T M \left[V^{eig}\right] = I \tag{3.26}$$

When the eigenvectors are mass-normalized as in Eq. (3.26), the definition of the MAC can be modified as in Eq. (3.27).

$$MAC_{ij} = \frac{\left(\left\{V_i^{eig}\right\}^T M \left\{\hat{V}_j^{eig}\right\}\right)^2}{\left(\left\{V_i^{eig}\right\}^T M \left\{V_i^{eig}\right\}\right)\left(\left\{\hat{V}_j^{eig}\right\}^T M \left\{\hat{V}_j^{eig}\right\}\right)} \tag{3.27}$$

The correlation between the full and the reduced model faces a problem of different sizes of matrices. As discussed in [39], the reduced matrices should be expanded to the original dimension via the transformation matrix or the opposite. However, the size of the transformation matrix (approx. 2 million DOFs in the full model of WEM) makes this process practically infeasible. Therefore, the application of this criterion was adjusted to the case in this project. Without the transformation matrix, no consistent mass matrix can

be found for both models. The problem of the inconsistent size of eigenvectors could be solved by selecting all the common DOFs from the eigenvectors of both models (Eq. (3.28)). It would be expected in the well-correlated case that the diagonal elements of the MAC values should be close to 1 but the non-diagonal values could not be ensured to be low because the orthogonality is not observable through part of the elements in the vectors.

$$MAC_{ii} = \frac{\left(\left\{V^{eig}_{i(sel)}\right\}^T \left\{\hat{V}^{eig}_{i(sel)}\right\}\right)^2}{\left(\left\{V^{eig}_{i(sel)}\right\}^T \left\{V^{eig}_{i(sel)}\right\}\right)\left(\left\{\hat{V}^{eig}_{i(sel)}\right\}^T \left\{\hat{V}^{eig}_{i(sel)}\right\}\right)} \tag{3.28}$$

Applying the adjusted criterion (Eq. (3.28)), the diagonal MAC values are shown in Fig. 3.8. A good correlation can be seen until the 600^{th} eigenmode, which corresponds to approx. 300 Hz. This criterion could not be employed strictly, providing the global indicator, but it showed the correlation of the common DOFs, i.e. the master DOFs (refer to Section 3.3.1).

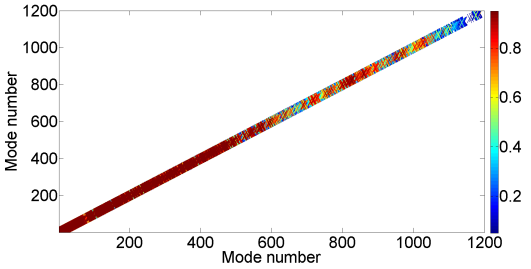

Figure 3.8.: MAC values according to the adjusted criterion

3.4.2. Validation based on harmonic analysis

Harmonic analysis or frequency response analysis is used to calculate the steady-state response of a linear structure to a sinusoidal excitation of a certain frequency. The frequency response assurance criterion (FRAC) shows how the individual DOFs contribute to the overall modal vector correlation. It can be calculated, according to Eq. (3.29), based on the frequency responses

of two models from input p to output q in the frequency range of interest between ω_1 and ω_2.

$$FRAC_{pq} = \frac{\left| \sum_{\omega=\omega_1}^{\omega_2} \hat{H}_{pq}(\omega) H^*_{pq}(\omega) \right|^2}{\sum_{\omega=\omega_1}^{\omega_2} \hat{H}_{pq}(\omega) \hat{H}^*_{pq}(\omega) \sum_{\omega=\omega_1}^{\omega_2} H_{pq}(\omega) H^*_{pq}(\omega)} \tag{3.29}$$

With this criterion, the correlation between the generated SS model and the original FE model up to 260 Hz was evaluated. The unbalance excitation and the actuation along the vibration transmission path from the rotor to the fuselage in the front and in the rear (as shown in Fig. 1.1) were selected as inputs (Table D.1) and the acceleration and force at these relevant DOFs as outputs (Table D.2). The FRAC values (Table D.3) are listed in Appendix D.1, and the minimum and average values are extracted in Table 3.4. Referring to Table D.3, it could be found that all the minimum values correspond to the 6^{th} DOF, rotational DOF around the z-coordinate (see Fig. 3.1 for the definition of the coordinate system), at the junction between link 4 of the MNT (transmitting thrust) and the fuselage. The response from the actuation of the front link of the MNT to the 6^{th} DOF of link 4 is presented in Fig. 3.9 as an example. The correlation is good, and thus it could be inferred that the small FRAC value may result from the small deviation in the low frequency response. The response of the 6^{th} DOF at link 4 is roughly one fifth of the response of the 5^{th} DOF, the rotational DOF around the y-coordinate (Fig. 3.1). According to the high average FRAC values and the small values of minima due to the minor deviation in the low response at a certain DOF, it can be concluded that the generated model is well correlated to the original.

Input	0	1	2	3	4	5	***Min***
Min	63.79%	74.14%	68.10%	65.22%	**61.77%**	64.18%	61.77%
Average	97.23%	97.53%	96.58%	97.97%	97.54%	97.27%	96.58%

Table 3.4.: The minimum and average values of FRAC extracted from Table D.3

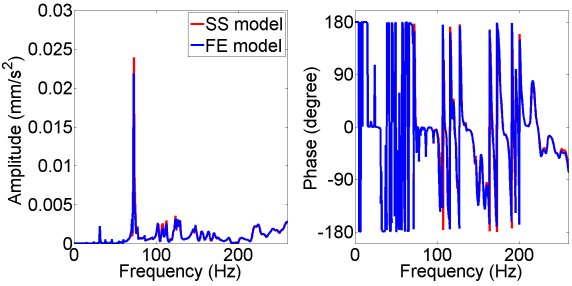

Figure 3.9.: Frequency response from the actuation of the front link of the MNT to the 6^{th} DOF of link 4 of the MNT in acceleration

3.4.3. Validation based on transient analysis

With FRAC, the correlation in a certain frequency range can be considered. As in the section above, the FRAC values up to 260 Hz were investigated, and a good correlation has been proved. Taking the other frequencies also into consideration, the time response should be investigated. Here the Pearson's correlation coefficient (Eq. (3.30)) was applied to evaluate the correlation of the data from the transient analysis. Ranging from 0 to 1, the higher this coefficient is, the better correlation is indicated.

$$\rho_{X,Y} = \frac{E[(X - \mu_X)(Y - \mu_Y)]}{\sigma_X \sigma_Y} \tag{3.30}$$

where X and Y are two series of data, $E(\ )$ computes the expectation, and μ_X and σ_X are the mean and the standard deviation of X.

The transient analyses were conducted under the excitation of unbalance at 150 Hz and 260 Hz, representing the idle state and the max. take-off frequency of the engine, which are also the minimum and maximum of the frequency range of this investigation. The sampling rate was 10 kHz, and the data up to 0.5 s were collected to calculate the correlation coefficient. The results are listed in Appendix D.2. The lowest levels of correlation are indicated by a coefficient of 92.51% and 91.67% for the two excitation frequencies, respectively. With the correlation coefficient at such high values, it can be

concluded that the model is verified and this model generation procedure is reliable.

3.5. Generated models and discussion

As discussed in Section 3.3.2, five models should be generated according to the bearing configurations (Fig. 3.6). The integrated damping methods and the use of each model are listed in Table 3.5. How these different configurations influence the system will be discussed first with respect to the structure of SFDs and the installation of both SFDs and actuators. Since the investigation is focused on the vibration originating from the rotor, the gyroscopic effect of the rotors in this model is also an important aspect to observe. Finally, it will be discussed how the unbalance at different positions affect the response of the system.

No.	Bearing configuration	Passive	Active	Used for
Model 1	Rigid	No	No	ActInSus w/o SFD ActExSus w/o SFD
Model 2	Actuators installed at bearing 3	No	Yes	ActBrg w/o SFD
Model 3	SFD applied at bearings	Yes	No	ActInSus with SFD ActExSus with SFD
Model 4	SFD and actuators applied in serial connection	Yes	Yes	ActBrg with SFD
Model 5	SFD and actuators applied in parallel connection	Yes	Yes	ActBrg with SFD

Table 3.5.: Summary of the use of five models with different bearing configurations

3.5.1. Gyroscopic effect on the model

The gyroscopic effect is caused by the inertial property and changes the resonating behavior of the rotating system. A Campbell diagram is a tool

to describe the change of eigenfrequencies with the increase of the rotational speed of the rotor due to the gyroscopic effect.

On the HPR with both ends fixed

Since the behavior of the WEM is complex, a simplified scenario is firstly considered: The HPR with both ends fixed, excluding the non-rotating parts and the LPR. The Campbell diagrams of the five models below 260 Hz are shown in Fig. 3.10 (no eigenfrequencies within the range between 200 Hz and 260 Hz, wherefore this range in y-axis is not included in the figure). The lines are split with the increase of the rotation frequency of the HPR, representing the frequencies related to the bending modes. The line going up stands for the forward whirl mode and that heading down for the backward whirl mode (see [64] for a detailed explanation). The two flat lines with constant values of 130.8 Hz and 132.1 Hz (five lines corresponding to the five models overlap each other at these two values, respectively) represent the translational and torsional modes, which are neither affected by the rotational frequency of the rotor nor by the different bearing configurations. Below 260 Hz, the translational and torsional modes and two bending modes can be observed on Models 3 & 4, and the translational and torsional modes and one bending mode on Model 1, 2 & 5. The bending eigenfrequencies of the former are lower than those of the latter, which may be due to the different values of stiffness at the front bearing (Table 3.2). The black dotted line corresponds to synchronous excitation, that is, the analysis frequency is equal to the excitation frequency. The intersection points between this and the other lines represent the eigenfrequencies at which the resonances of the rotating system are excited.

To further investigate the response of the rotor with the influence of gyroscopic effect, the frequency response analyses were performed to determine the bearings' reaction to the unbalance applied in the middle of the HPR (at the 6^{th} stage) which is synchronous with the speed of rotor. Fig. 3.11 shows the responses in x, y and z coordinates at B3 of Model 1, comparing the behavior of Model 1 with and without the gyroscopic effect. The two resonances at B3 on the x-coordinate represent the bending and translational modes, and both are much lower than the response over the whole frequency

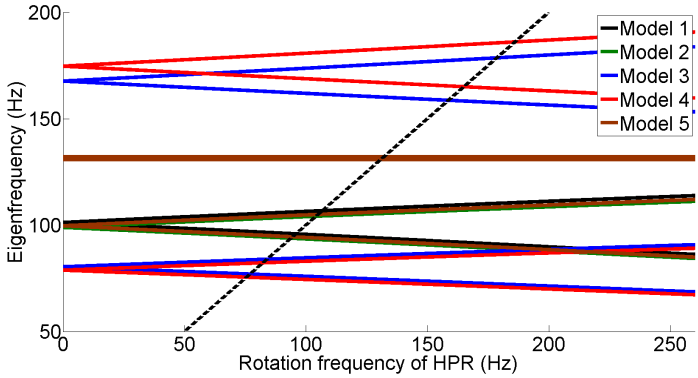

Figure 3.10.: Campbell diagrams of the HPR with both ends fixed

range in the y and z directions. Due to the symmetry of the rotor, the responses in the y and z directions are the same at both bearings, where only the bending mode is visible at around 100 Hz.

The gyroscopic effect can be observed by comparing the case without the gyroscopic matrix and the case with the gyroscopic matrix. The first resonance of the former case corresponds to the first bending mode of Model 1 when the rotor is at standstill. It corresponds to the first eigenfrequency on the y-axis in Fig. 3.10. Since the unbalance triggers the forward whirl mode influenced by the gyroscopic effect [64], the first resonance of the latter case corresponds to the intersection point between the line of synchronous excitation and the forward whirling line of Model 1 in Fig. 3.10. Generally, the gyroscopic effect does not affect the translational mode and shifts the bending eigenfrequency toward the right side.

Fig. 3.12 shows the response in Model 3 under the same excitation as above. Since SFDs are added, the bending resonances are almost fully damped, and the translational mode is not affected. In this case of a fixed HPR, the gyroscopic effect is not evident as the lines representing the two cases almost overlap each other.

On the HPR connected with the WEM

The same analysis as above was also conducted on the WEM without the

gyroscopic effect, with that of the HPR alone, with that of the LPR alone and with that of both rotors. The comparison among these cases in different frequency ranges can be found in Appendix E and that of the high frequency range 150 Hz − 260 Hz is shown in Fig. 3.13.

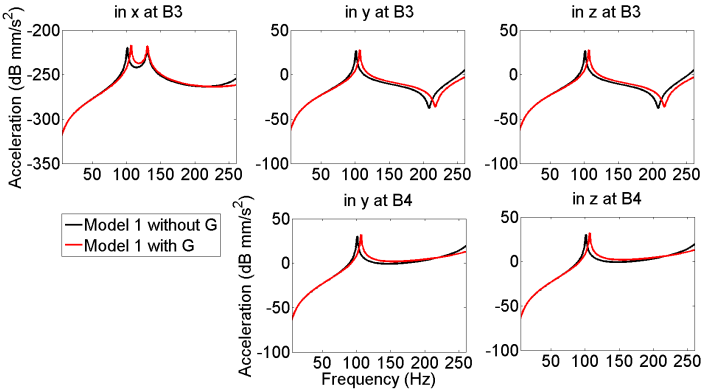

Figure 3.11.: Frequency response of HPR (Model 1) to the unbalance showing gyroscopic effect

Generally, the gyroscopic effect of both rotors on the WEM is complicated, especially in the frequency range above 120 Hz. Between 0 and 80 Hz, the gyroscopic effect of the HPR has little influence on the whole system, but around 95 Hz, it starts to become involved. In the rear at B4, several relatively high resonances around 160 Hz and in the range above 230 Hz are shifted and increased by the gyroscopic effect of the HPR, while at B3, the resonance around 250 Hz is critically changed by this effect as can be seen in Fig. 3.13. The gyroscopic effect of the HPR shows its greater effect in the range around 250 Hz compared with other ranges.

In these analyses of the reaction of the synchronously excited systems with the HPR, the interaction between the LPR and the HPR reduces the resonance amplitudes: those around 160 Hz and above 230 Hz in the rear and around 250 Hz in the front.

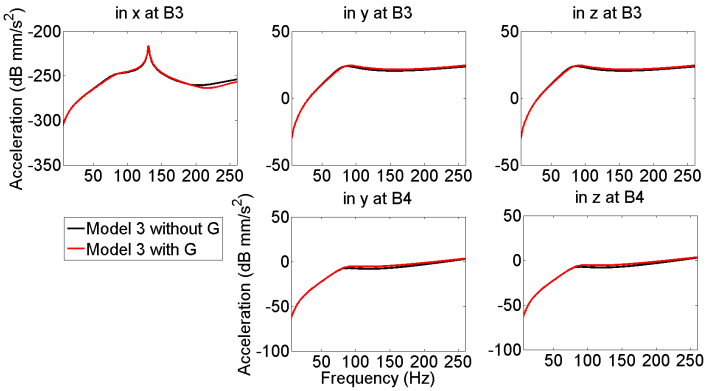

Figure 3.12.: Frequency response of HPR (Model 3) to the unbalance showing gyroscopic effect

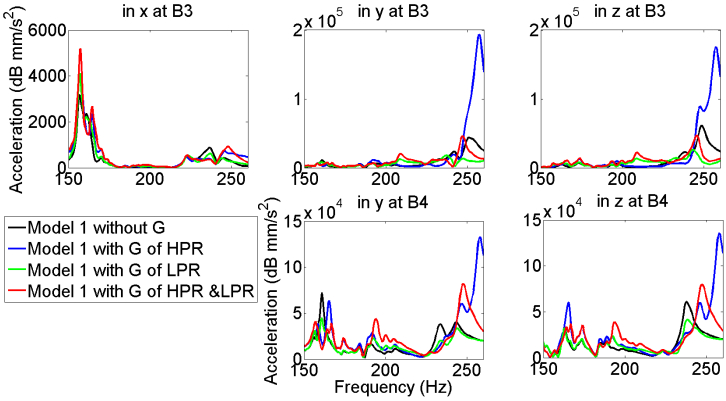

Figure 3.13.: Frequency response of HPR (Model 1) to the unbalance showing gyroscopic effect of the HPR and LPR (150 Hz – 260 Hz)

3.5.2. Effect of squeeze film dampers and their squirrel cage

SFDs are modeled with a spring element and a damping element, representing the SC and the oil film, respectively (see Section 2.3.1 for the structure of SFDs). The same synchronous analysis as above was conducted on the fixed HPR of Model 1, of Model 1 with only the SC but without a damping element in the front and of Model 3 in which both elements are included in the front. Fig. 3.14 shows the response at B3 in the above cases. The introduction of the SC shifts the bending eigenfrequencies to the left and increasing the resonance amplitudes, especially at B3 in the front. The decrease of the eigenfrequencies result from the smaller stiffness of the SC compared with the rigid bearing. The decrease of stiffness at B3 causes the vibration to be transmitted more through B3. With the damping element additionally introduced, the resonances are completely damped. With both elements included, the shift of frequencies is not evident but only the damping effect.

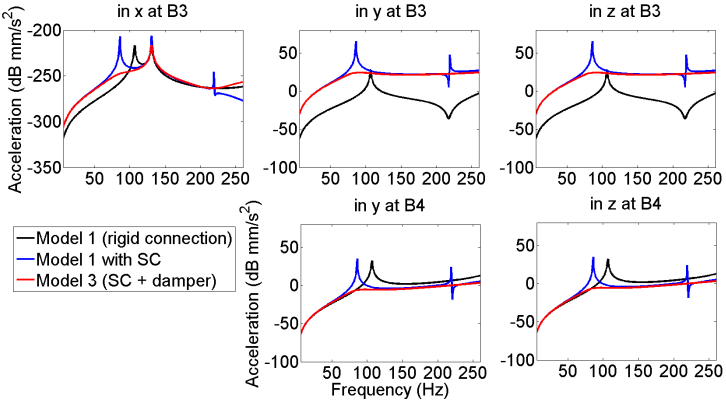

Figure 3.14.: Frequency response of HPR (with both ends fixed) to the unbalance showing the effect of SC alone and SFD

Fig. 3.15 shows the response at B3 under the same excitation as above, when the analysis is carried out in the environment of the WEM. The blue and black lines represent the systems with the SFDs applied at the front bearing of the HPR and that without the SFDs. The same as concluded

in the last paragraph, little frequency shift is visible, but only the damping effect. When SFDs are also introduced at the front bearings of the LPR, the response at B3 will be further reduced and that at B4 is scarcely altered.

3.5.3. Effect of squeeze film dampers and installed actuators at the bearings

To investigate the influence of the installation of SFDs and actuators, when they are not activated, the synchronous analyses as above were undertaken for the five models. The response at B3 can be found in Fig. 3.16 and in Fig. 3.17 when the two boundary conditions (fixed or connected with the WEM) are applied on the HPR, respectively. As seen in Fig. 3.16, they can be categorized into three (Model 1, Models 2 & 5, Models 3 & 4) and two groups (Models 1 & 2 & 5, Models 3 & 4), according to the front and rear responses, respectively. The difference between Models 1 & 2 & 5 and Models 3 & 4 is the effectiveness of the damping element of the SFDs. In Model 5, although SFDs are being used, the damping element is not effective due to the parallel connection with stiff actuators. The difference between Model 1 and Models 2 & 5 in the front result from the installation of the SC, which decreases the stiffness and increases the response at the front bearings.

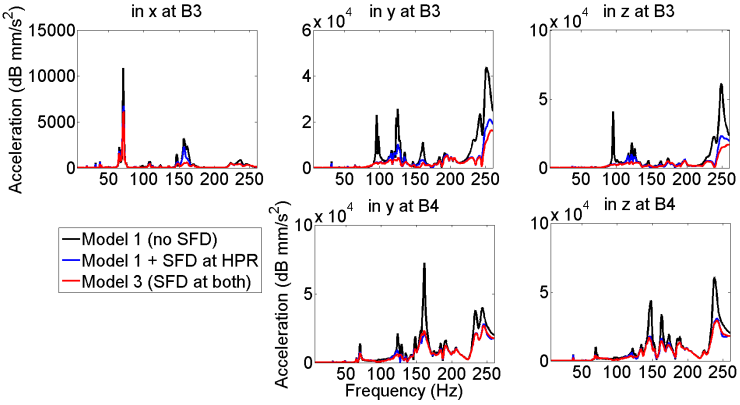

Figure 3.15.: Frequency response of HPR (connected with the WEM) to the unbalance showing the effect SFDs on the HPR and LPR

Considering the whole engine system (Fig. 3.16), similar conclusions can be drawn for the rear reaction. In the front, the responses can be categorized into three groups (Models 1 & 2, Model 5, Models 3 & 4) in the frequency range below 150 Hz. SFDs in Model 5 are relatively effective in the low frequency range in spite of a parallel connection with stiff actuators, compared with the models without SFDs. With an increasing frequency, the response of Model 5 approaches that of Models 1 & 2 up to 245 Hz. Around 220 Hz, the response varies little among all five models, while all of them differ from each other at the resonance around 250 Hz, shrinking with the decrease of the stiffness at B3 when SFDs are present.

3.5.4. Unbalance position

The synchronous excitation of unbalance at the 6^{th} stage was applied in the above analyses, to observe the first bending mode. Fig. 3.18 displays different lines representing the responses of the HPR with both ends fixed in Model 1 to the unbalance at different positions. The lines of different blue colors not listed in the legend represent the other stages except the 6^{th} and the bearings. At the first bending frequency, the unbalance at the bearing positions excites the system the least and that at the 6^{th} stage the most.

When the SFD is introduced, the maximum resonance at the first bending frequency is still caused by the unbalance at the 6^{th} stage (Fig. 3.19). The response to the excitation at B3 is similar to that at the 6^{th} stage, due to the lower stiffness at B3. The response at B4 to the excitation at all positions does not differ significantly, due to its relatively high stiffness. The unbalance at the 6^{th} stage of the HPR is the most critical, because it triggers the system's greatest response at the first bending eigenfrequency. This excitation has been used for all the investigations presented in the following chapters.

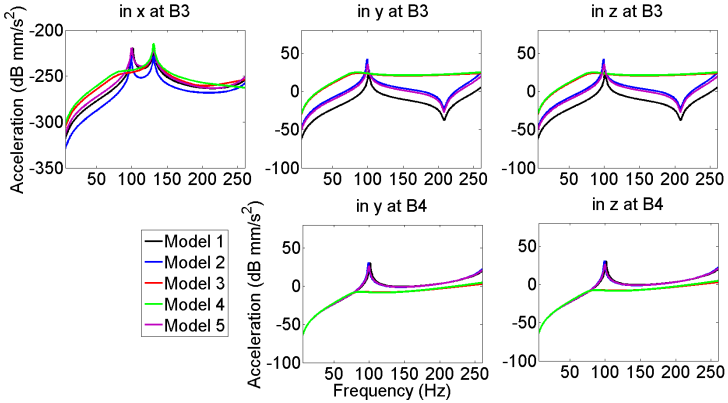

Figure 3.16.: Frequency response of the HPR (with both ends fixed) to the unbalance (five models)

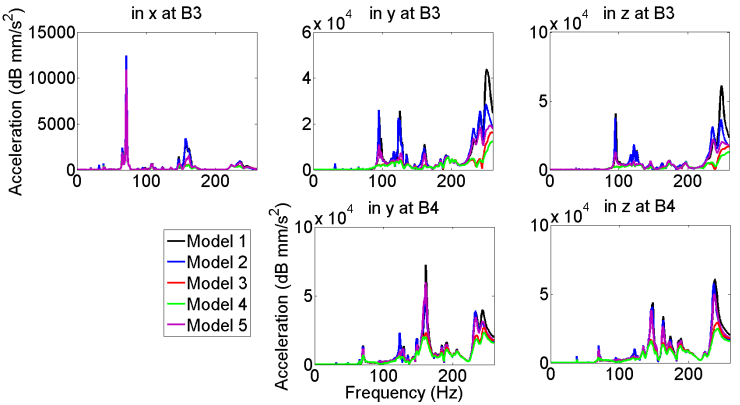

Figure 3.17.: Frequency response of the HPR (connected with the WEM) to the unbalance (five models)

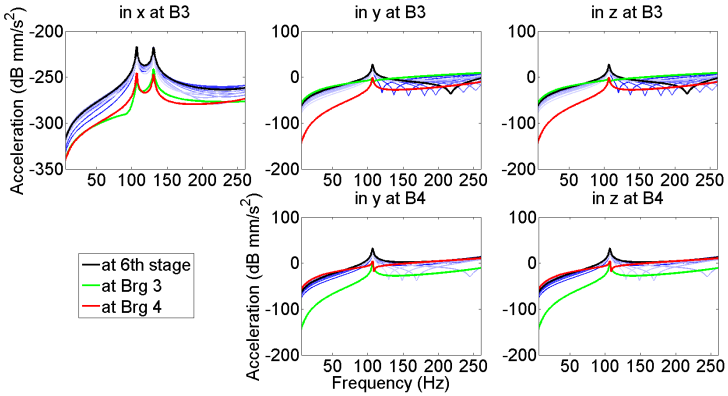

Figure 3.18.: Frequency response of the HPR (Model 1) to the unbalance at different positions

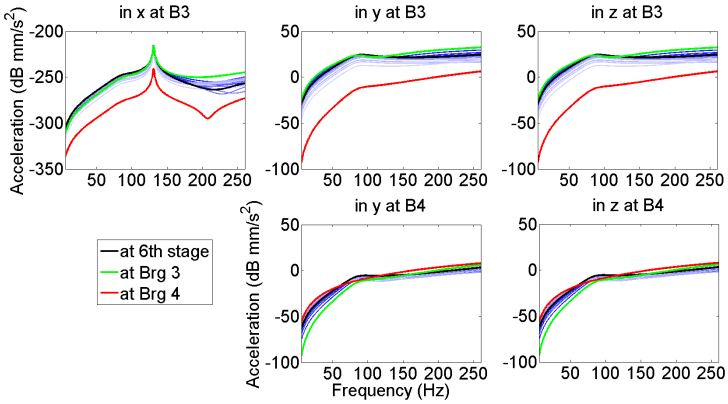

Figure 3.19.: Frequency response of the HPR (Model 3) to the unbalance at different positions

4. Evaluation of actuator placement approaches in the aircraft engine system

As discussed in Section 2.3.2, there are criteria 1) used to evaluate the controllability of a control system and 2) allowing the evaluation of the actuation positions with the optimized closed-loop response. In this chapter, the results from and discussion about the three actuator placement approaches with the second evaluation method will be presented, because a) there are comparatively few actuation positions to be studied, b) this method provides the information of the frequency response at frequencies of interest and c) it permits various settings for the closed-loop system, with which some relevant issues to control design can be studied initially, such as the type and number of sensors.

4.1. Suspension systems and evaluation criterion

Three suspension systems, consisting of vibration sources, transmission suspensions and vibration receivers, have been identified corresponding to the three actuator placement approaches (see Section 2.3.1 for the ActExSus approach and see Section 3.2 for the ActInSus and ActBrg approaches), so that they can be compared with the conclusions from some past studies on the suspension systems of simple structures (Section 6.1).

Generally, the positions of actuators are assumed as suspension, the part close to the HPR serving as vibration source and the part at the other end as vibration receiver, as listed in Table 4.1 and shown in Fig. 4.1. The arrows in the figure represent the actuation along the suspension and the

circles indicate the targeted positions in optimization. To investigate the effectiveness of ActExSus, the links of the MNT are actuated to reduce the vibration from the FUL, FLL and RMR to the fuselage; the vibration at the junctions of the MNT links with the fuselage (JntFL) should be optimized. ActInSus is designed to attenuate the vibration of the junctions between the MNT and the engine (JntENG) by actuating the internal struts, as the double arrows indicate. In the approach of ActBrg, the HPR is set as the source due to its unbalance and the other part of the engine as the receiver. B3 and B4 connect them as suspension, and only B3 is actuated aiming at achieving optimal vibration reduction at both B3 and B4 (JntB34).

Appr.	Source	Suspension	Receiver	Opt. at
1 ActExSus	FUL FLL RMR	MNT	Fuselage	JntFL
2 ActInSus	Core engine	Internal struts	FUL FLL RMR	JntENG
3 ActBrg	HPR	B3 and B4	Engine	JntB34

Table 4.1.: Three suspension systems corresponding to the three actuator placement approaches

The results in this chapter will be mainly presented in terms of power (the power in the following text, if not specified, refers to the average power, see the constant part in Eq. (2.8) or the real part in Eq. (2.9) or P_{av} in Eq. (A.21) in Appendix A), since power corresponds to the vibrational energy carried along the transmission path. Acceleration is an important evaluation criterion of the sensed comfort in the vehicle [41]. However, before reaching the comfort-sensing position, where passengers are located, the vibration is passed on as energy, and the analysis of acceleration on the transmission path is insufficient to come to any conclusion. In this study, the sensors are placed to measure the acceleration at the junctions between the fuselage and the MNT (JntFL). Nevertheless, the JntFL are not the end of the vibration transmission path, for the vibration will be further spread over the fuselage as vibrational energy to the seats. It is stated in [17] that different mechanisms in the vibration transmission may be compared by using a power approach and that vibrational power has been used in past studies, such as in a series study [21][22][23] and in [38]. The comparison of power on the upstream and

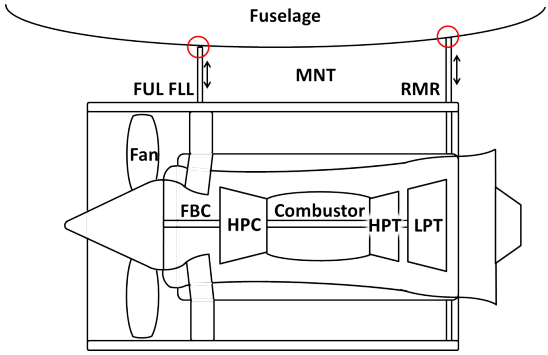

(a) Active external suspension

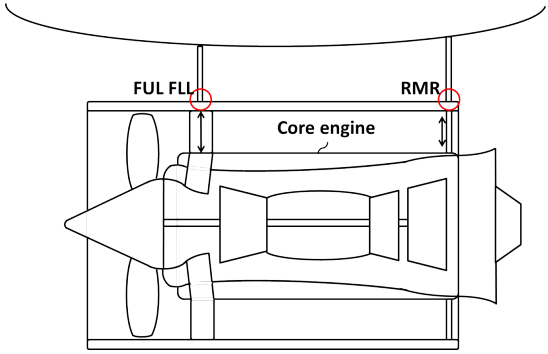

(b) Active internal suspension

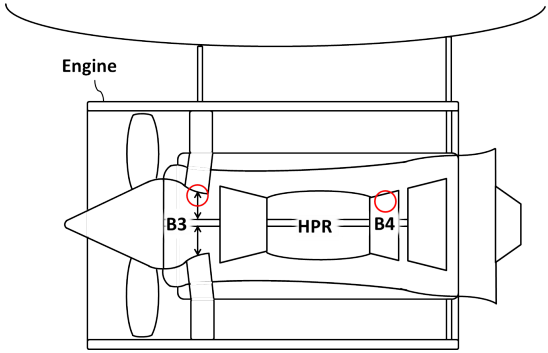

(c) Active bearing

Figure 4.1.: Three suspension systems corresponding to the three actuator placement approaches

downstream path also indicates how the vibration is transmitted. Moreover, this single parameter can be used to describe the dynamics of the system in a consistent manner [17]. The acceleration is evaluated in different degrees of freedom at each junction, while, considered in terms of power, the vibration in different degrees of freedom can be compared or added up as one, indicating the transmitted vibration at a single or several junctions. The comparison of the vibration through axial forces and through moments is also possible.

4.2. Damping effect of the open-loop systems

Before discussing the optimized active systems and evaluating the actuation approaches, the damping effect of the open-loop systems will be presented here.

In the following tests, a constant unbalance of the HPR is assumed to be the vibration cause. The excitation increases with the rotational speed of the HPR as expressed in Eq. (2.1). The rotational speeds of two rotors are plotted in Fig. 4.2. As labeled, the engine is in the idle state, when the HPR rotates at 150 Hz, and the HPR is accelerated from 150 Hz to 260 Hz to take off. The rotational speed of the LPR is 0.2 of the HPR in the idle state and increases linearly from 30 Hz to 120 Hz during the acceleration to take off.

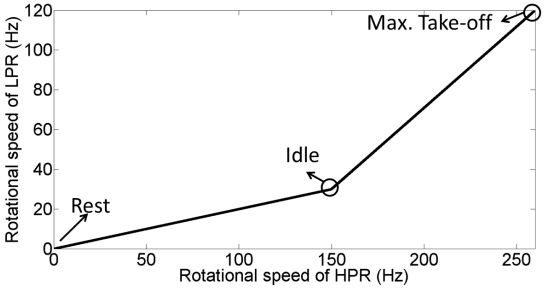

Figure 4.2.: Rotational speed of HPR & LPR

Fig. 4.3 shows how the vibrational power due to the unbalance (1000 gmm) at stage 6 (see Section 3.5.4 for relevant reason) travels from the HPR to the JntFL in terms of the total power through forces and moments in Model

1. Four stages have been identified to describe the power flow in the WEM due to the unbalance of the HPR: 1) The input power by the unbalance, 2) the power transmitted through B3 & B4, 3) through the FUL, FLL & RMR and 4) through the MNT. The input power is computed with the unbalance forces and velocities at the unbalance position. The power through B3 and B4 is only slightly lower than the input power, which means that there is little damping effect on the HPR and its bearings, and the same applies to the MNT, through which rather little vibration is damped, considering the power transmitted through the FUL, FLL and RMR and that through the MNT. And the effect of the structural damping of the engine cannot be neglected according to the difference between the power through B3 and B4 and that through the FUL, FLL and RMR.

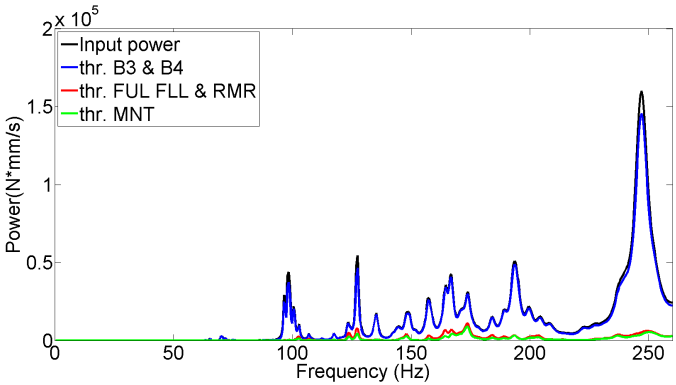

Figure 4.3.: Vibration transmission in terms of power in Model 1 due to the unbalance

To study the robustness of the five systems, i.e. how robust the systems can be when the actuators are installed but fail to operate, the power transmitted through the MNT into the fuselage is assessed in five uncontrolled systems in Fig. 4.4. It proves comparable to the result in terms of acceleration at both HPR bearings in Fig. 3.17. The highest vibration produced at the end of the transmission path, at the JntFL, is in Model 1 without passive or active damping. With the installation of the actuators, the stiffness at bearing 3 is reduced, and the vibration in terms of power is slightly reduced in the high

frequency range above 200 Hz as seen from the Model 2. Model 5 with SFDs and actuators installed in a parallel connection has better performance than Model 2 in most of the frequency ranges. Model 4 with SFDs and actuators installed in a serial connection is slightly better than Model 3 with SFDs, and both of them vastly outperform the other three.

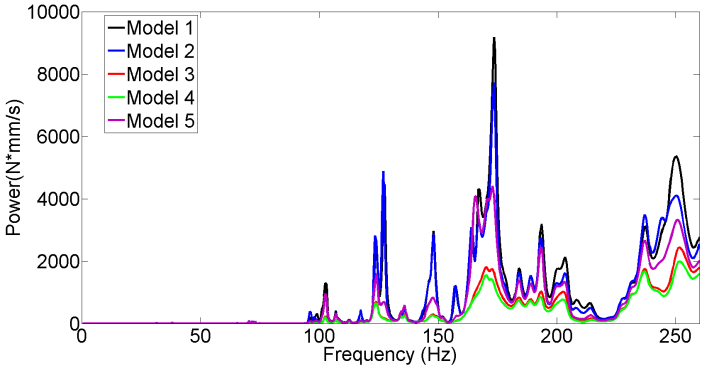

Figure 4.4.: Power transmitted through the MNT into the fuselage in five uncontrolled systems due to the unbalance

From the results above, it can be inferred that installing the actuators reduces the stiffness at the bearing together with the vibration. In Model 5, although the stiffness is increased due to the parallel connection of actuators and SFDs compared with Model 2, the vibration is attenuated more by the damping effect of the SFDs. In the presence of SFDs, the parallel configuration of Model 5 shows the worst robustness, presumably because the high stiffness hinders the damping effect of the SFDs. Accordingly, the serial configuration proves to be the best. Therefore, it can be concluded that a low stiffness at the bearing and the damping element of the SFDs play an important positive role regarding the robustness of the system. In terms of the power transmitted into the fuselage, the models can be categorized into three groups from the best to the worst: Models 3 and 4 with SFDs, Model 5 with SFDs in parallel with actuators, Models 1 and 2 without SFDs.

The introduction of SFDs and/or actuators alters the vibration transmission through the bearings and eventually through the MNT into the fuselage.

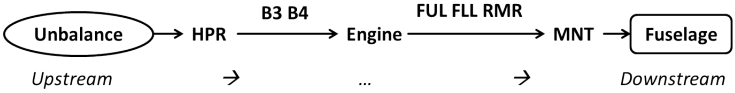

Figure 4.5.: Illustration of the vibration transmission path from the upstream to the downstream in the WEM

To find out if the change at the bearings also influences the structural damping effect of the MNT, the engine and the rotor, the ratio η_{dmp} of the power difference between the upstream and the downstream positions to the power at the upstream position (Eq. (4.1)) is calculated to indicate the damping effect of each part. Fig. 4.5 shows the upstream and downstream positions of each part. The damping effects of the MNT, of the engine and of the rotor are plotted in Fig. 4.6. The first two are of the same magnitude in the five systems. Models 1 and 2 without SFDs overlap each other, and Models 3, 4 and 5 with SFDs overlap each other at most of the frequencies. Thus, the damping effects of the MNT and of the engine are only slightly affected by the presence of SFDs. As for the damping effect of the bearings of the HPR, Models 3 and 4 are identical with high damping over 0.5 at most of the frequencies, especially high in the low frequency range, while the other three models mostly show a value below 0.5. It can be concluded that the effective SFDs (the SFDs in Model 5 can be counted as ineffective) affect the damping effect of the HPR and that the presence of SFDs has a slight influence on the damping effect of the engine and of the MNT.

$$\eta_{dmp} = \frac{Power_{ups} - Power_{dns}}{Power_{ups}} \tag{4.1}$$

4.3. Optimization of the closed-loop systems

Based on the method of optimizing the closed-loop response introduced in Section 2.3.2 and the minimization calculation of the quadratic cost functions in Appendix A, not only can the three actuator placement approaches be evaluated, but several other aspects can also be studied, such as the sensor type.

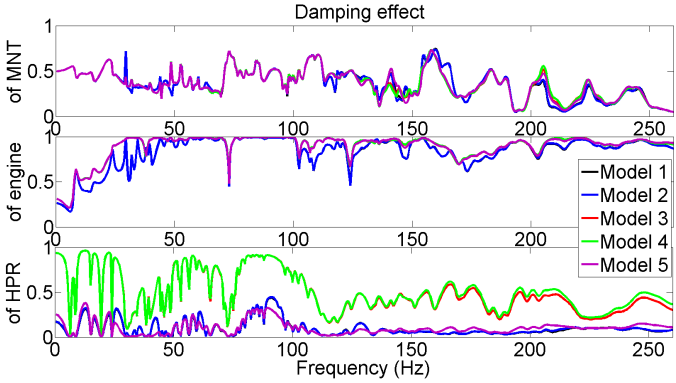

Figure 4.6.: Damping effect of the HPR, the engine and the MNT in five uncontrolled systems

This section will focus on comparison of the three approaches and relevant factors which can influence the reduction effectiveness of each approach.

The system is assumed to undergo the vibration caused by an unbalance of 1000 gmm at the 6^{th} stage of the HPR. Assuming that translational actuators are used, the actuation are force pairs in opposite directions along the suspension and are set as the variables in the optimization calculation. The target is to minimize the physical quantities measured at that end of the suspension (in circles in Fig. 4.1), aiming at minimizing the vibration carried into the receiver. These settings are summarized in Table 4.2. In the last physical quantity of target, k is a scaling factor to combine the two quantities, squared force and squared velocity. The scaling factor in this investigation was adjusted as one constant for all the frequencies, aiming at minimizing the highest resonance.

With these optimization settings, five groups of simulations were carried out. First of all, it was designed to find out how the cost functions of different physical quantities (Eq. (A.13), (A.14) & (A.21)) influence the effectiveness of the vibration reduction. Then, selecting one of the optimization quantities as a preliminary decision for the sensor type, the three actuator placement approaches should be compared. The vibration is transmitted by forces in the form of translational (Tr.) movement and moments in the form of rota-

	Physical quantity	Position
Excitation	Unbalance 1000 gmm	at the 6^{th} stage of HPR
Variable	Actuation forces	on suspension
Target	Power $P = FV$	at the suspension end close to the receiver
	Squared force F^2	
	Squared acceleration A^2	
	Combination $(F^2 + kV^2)$	

Table 4.2.: Summary of optimization settings

tional (Ro.) movement. It was stated in [31] that when only the translational power transmitted through translational DOFs is minimized, the overall performance of the active isolator can be worse than without control in its beam system. Therefore, it is worth finding out for the three suspension systems in the WEM if the measurement of both, the translational and the rotational DOFs, is necessary for the reduction in the whole vibrational power. In Chapter 3, it was explained how the gyroscopic effect influences the uncontrolled system, and in this chapter, a group of simulations was also designed to observe how this effect interacts with the active system. The previous section demonstrated how SFDs affect the damping of passive systems, and this section will examine if they influence the active system differently and how this passive damping interacts with the actuation of the active method. For the above purposes, groups of simulations are listed in Table 4.3.

Section 4.3.1	Section 4.3.2	Section 4.3.3	Section 4.3.4	Section 4.3.5
Physical quantity	Approach	Ro. DOFs	Gyroscopic effect	SFDs
$P = FV$ F^2 A^2 $F^2 + kV^2$	ActBrg ActInSus ActExSus	Only Tr. Tr. & Ro.	Considered Not considered	With Without

Table 4.3.: Summary of comparison groups in the optimization study

4.3.1. Optimization of different physical quantities

The original system Model 1 without any damping techniques was selected for the study on physical quantity to be optimized, not considering any effects from the SFDs or the gyroscopic effect for simplicity. In the optimization, both the translational and rotational DOFs were considered. Four quantities will be compared: Power, squared force, squared acceleration and the combination of squared force and squared velocity. These quantities reflect the sensor type and/or number used in the future control design and implementation. Since the results are evaluated in terms of power, it is expected that using power as the optimization objective will yield the best performance. Therefore, optimizing power is used as a benchmark in this section, and it will not be selected for the following investigation because the reduction effectiveness based on this strategy could be very sensitive to the measurement accuracy of sensors [18]. From the open-loop response in Fig. 4.4 it can be seen that the high excitation appears mainly above 100 Hz. So the results are restricted to 100 Hz − 260 Hz in this section.

In the suspension system of ActExSus, the total power, both translational and rotational, through links of the MNT is estimated for each frequency and compared with the open-loop system in Fig 4.7. Optimizing the squared forces yields small improvements at most of the frequencies, but worse performance in some frequency ranges, e.g. around 160 Hz. Optimizing power is, as expected, the best among them. The other two show slightly less effectiveness than optimizing power.

As for the ActInSus system in which the actuated suspension connects the core engine and the outside mount links (FUL, FLL and RMR), Fig. 4.8 shows the optimized results in terms of total power through the FUL, FLL and RMR. It allows similar inferences as above in the MNT suspension system, except that optimizing power here brings approximately ten times better performance than the other three, and optimizing the squared force is comparable with optimizing the squared acceleration.

In the ActBrg system consisting of the HPR as the source and the rest of the engine as the receiver, the trend of each optimized result is different from those of the two suspension systems above. As shown in Fig 4.9, optimiz-

ing power and optimizing squared acceleration are similar and approx. 100 times lower than the other three in the frequency range below 200 Hz, while optimizing the squared force provides little improvement to the uncontrolled system and optimizing the combination reduces the power roughly by ten times. In the frequency range above 200 Hz, all of them show good effectiveness with the following ranking from best to worst: Optimizing power, squared acceleration, combination, squared force. It is worth noting that at 260 Hz, the max. take-off frequency, optimizing the squared acceleration or squared force alone does not yield any improvement, and optimizing the combination or power reduces the power by half from around 2000 Nmm/s to 1000 Nmm/s.

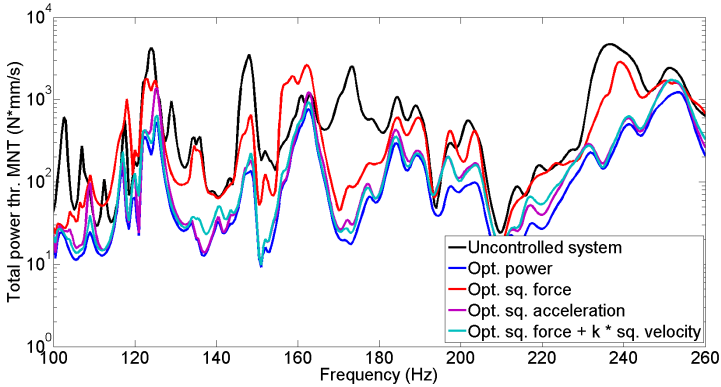

Figure 4.7.: Power transmitted through the MNT when optimizing four quantities at the links of the MNT

In summary, optimizing power always provides the best result, as expected. The performance of the closed-loop system, when optimizing the squared acceleration, is the second best at most of the frequencies in the three suspension systems. Especially in the first suspension system and the third suspension system in the low frequency range, it shows almost the same performance as optimizing power. However, at certain important frequencies it can be ineffective, e.g. in the third suspension system at the max. take-off frequency. Optimizing the squared force leads to the worst performance in the first and

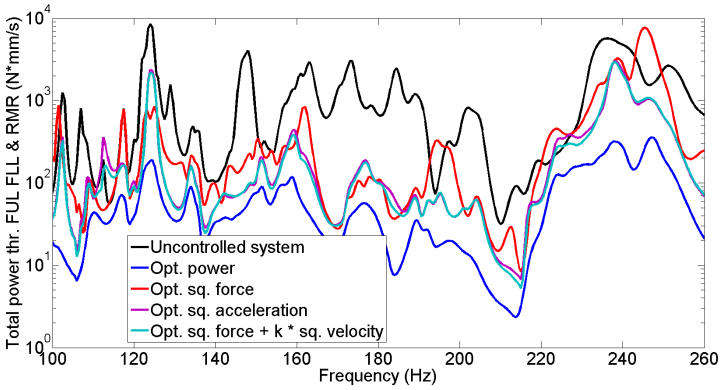

Figure 4.8.: Power transmitted through the FUL, FLL and RMR when optimizing four quantities at the FUL, FLL and RMR

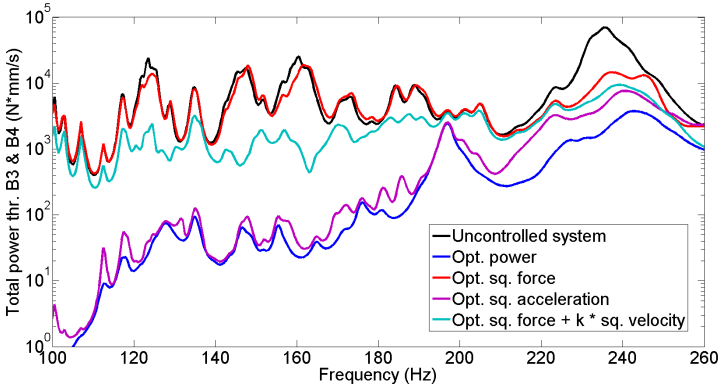

Figure 4.9.: Power transmitted through B3 and B4 when optimizing four quantities at B3 and B4

third systems, and it presents even greater vibration in terms of power than the uncontrolled system at some frequencies. However, its comparable results in the ActInSus system with optimizing the squared acceleration indicate the importance of forces in transmitting the power through FUL, FLL & RMR. Optimizing the combination of the squared force and squared velocity has the same effectiveness in vibration reduction in power as optimizing the squared acceleration in the first two suspension systems. It can also avoid the ineffectiveness of optimizing the squared acceleration alone at certain frequencies in the third suspension system, although compromising for a lower reduction in the low frequency range.

4.3.2. Damping effect of different actuator placement approaches

Based on the analysis in the last section, optimizing the combination of the squared force and squared velocity was selected to study different actuation approaches. Both the translational and rotational DOFs were considered in the optimization calculation. The effects from the SFDs and gyroscope were not considered in this section, either.

Damping effect of the MNT, engine and HPR in active systems
As can be seen in Fig. 4.6, the damping effect defined in Eq. (4.1) is limited between 0 and 1, since the power is always positive and decreases along the transmission path from the HPR as the source to the fuselage in the passive systems. However, it is not the case in the active system due to the active elements at a certain section of the vibration transmission path. Thus the damping effect is no longer limited to $0 - 1$. The meanings of the values in different ranges are listed in Table 4.4. The categorized cases are described below:

- (1) $Power_{ups}$ and $Power_{dns}$ are both negative (deduced according to the equations below), and $Power_{ups}$ is larger than $Power_{dns}$, i.e. the absolute value of $Power_{ups}$ is smaller than that of $Power_{dns}$. It means that the power flows in fact from the afore-defined downstream to the

upstream and is reduced, when going through this part. In other words, this part in this case dissipates the energy from downstream.

Based on

$$Power_{ups} > Power_{dns} <=> Power_{ups} - Power_{dns} > 0 \quad (4.2)$$

and

$$\eta_{dmp} = \frac{Power_{ups} - Power_{dns}}{Power_{ups}} < 0 \quad (4.3)$$

it is derived that

$$Power_{ups} < 0 \quad (4.4)$$

i.e.

$$Power_{dns} < Power_{ups} < 0 \quad (4.5)$$

- (2) $Power_{ups}$ and $Power_{dns}$ are both positive (similar deduction to case (1)), and $Power_{ups}$ is larger than $Power_{dns}$, i.e. the absolute value of $Power_{ups}$ is larger than that of $Power_{dns}$. It means that the power flows in fact from the afore-defined upstream to the downstream and is reduced, when going through this part. In other words, this part in this case dissipates the energy from upstream.

- (3) $Power_{ups}$ is positive and $Power_{dns}$ negative (similar deduction to case (1)). It means that $Power_{ups}$ flows from the afore-defined upstream to this part and $Power_{dns}$ also from the afore-defined downstream to this part. In other words, this part in this case dissipates the energy both from upstream and downstream.

- (4) $Power_{ups}$ and $Power_{dns}$ are both positive (similar deduction to case (1)), and $Power_{ups}$ is smaller than $Power_{dns}$, i.e. the absolute value of $Power_{ups}$ is smaller than that of $Power_{dns}$. It means that the power flows in fact from the afore-defined upstream to the downstream and is increased, when going through this part. In other words, this part in this case works as an additional source towards downstream.

- (5) $Power_{ups}$ and $Power_{dns}$ are both negative (similar deduction to case (1)), and $Power_{ups}$ is smaller than $Power_{dns}$, i.e. the absolute

value of $Power_{ups}$ is larger than that of $Power_{dns}$. It means that the power flows in fact from the afore-defined downstream to the upstream and is increased, when going through this part. In other words, this part in this case works as an additional source towards upstream.

- (6) $Power_{ups}$ is negative and $Power_{dns}$ positive (similar deduction to case (1)). It means that $Power_{ups}$ flows from this part to the afore-defined upstream and $Power_{dns}$ also from this part to the afore-defined downstream. In other words, this part in this case dissipates works as an additional source both towards upstream and downstream.

This indicator η_{dmp} indicates not only the magnitude of the damping through a certain part but also the direction of the energy flow and the function of this part either as damper or as energy source. When the upstream power is larger than the downstream, energy is always dissipated from one side (i.e. upstream or downstream) with the value less than 1 or from both sides with the value larger than 1. When the upstream power is less than the downstream, that part works as an additional source toward one side with the value smaller than 1 or toward both sides with the value larger than 1.

η_{dmp}	$Power_{ups} > Power_{dns}$	$Power_{ups} < Power_{dns}$
	Dissipating energy from	*Additional source toward*
(-inf, 0)	downstream (1)	downstream (4)
[0, 1)	upstream (2)	upstream (5)
[1, inf)	down- and upstream (3)	up- and downstream (6)

Table 4.4.: Interpretation of values of the damping effect due to an active control systems

Based on the principle described above, the functions of the MNT, the engine and the HPR with the three approaches applied in the system are summarized in Tables 4.5, 4.6 and 4.7. The simulation has been carried out in the frequency range of $0 - 260\,\text{Hz}$ with an interval of $0.5\,\text{Hz}$. The total number of frequencies is 520. The number in the tables means how many frequencies belong to the corresponding case. The number in the merged cell

indicates the total number of frequencies belonging to the three cases. These cases under the condition of $Power_{ups} > Power_{dns}$ are not divided, because the dissipation is generally regarded as positive and it is not necessary to distinguish them in this investigation.

MNT active	$Power_{ups} > Power_{dns}$	$Power_{ups} < Power_{dns}$
(-inf, 0)	459	3
[0, 1)		none
[1, inf)		58
Engine passive	$Power_{ups} > Power_{dns}$	$Power_{ups} < Power_{dns}$
(-inf, 0)	520	none
[0, 1)		none
[1, inf)		none
HPR passive	$Power_{ups} > Power_{dns}$	$Power_{ups} < Power_{dns}$
(-inf, 0)	441	71
[0, 1)		none
[1, inf)		8

Table 4.5.: Damping effect of the HPR, the engine and the MNT with active external suspension

It can be inferred that with the active external suspension (Table 4.5), the MNT dissipates the energy at most frequencies and works as a source toward the upstream and downstream at some frequencies. It is acceptable since the vibration in power at these frequencies is less than that in the uncontrolled system. The damping effect through the actuated MNT on the original vibration source attenuates the original vibration to a larger extent than the vibration generated by the actuated MNT as a source. The engine in this system works only as a passive damping part, which dissipates the vibration from both sides. While the role of the engine is unchanged through this actuation method, the HPR is forced to act as a source toward the downstream and upstream at some frequencies. The role of the HPR in the active case is to transmit the vibration, which comes from the unbalance

position and is reduced by the actuated MNT, and at the same time act as an additional source. In other words, the vibrational energy does not originate concentrated from the unbalance position at these frequencies, but is distributed along the HPR due to the actuated MNT.

MNT passive	$Power_{ups} > Power_{dns}$	$Power_{ups} < Power_{dns}$
(-inf, 0)	520	none
[0, 1)		none
[1, inf)		none
Engine active	$Power_{ups} > Power_{dns}$	$Power_{ups} < Power_{dns}$
(-inf, 0)	483	none
[0, 1)		none
[1, inf)		37
HPR passive	$Power_{ups} > Power_{dns}$	$Power_{ups} < Power_{dns}$
(-inf, 0)	440	70
[0, 1)		5
[1, inf)		5

Table 4.6.: Damping effect of the HPR, the engine and the MNT with active internal suspension

With the active internal suspension approach (Table 4.6), the engine dissipates the vibrational energy at most frequencies and acts as a source toward the upstream and the downstream parts at the other, but it is acceptable for the same reason as in the ActExSus approach. Similar to the approach above, the active part between the core engine and the MNT also turns its upstream part, the HPR, into a source at some frequencies, so that the vibration source is not concentrated but distributed along the HPR. This approach does not affect the role of the MNT as a passive damping structure.

The active bearing approach (Table 4.7) activates the front bearing of the HPR. As the active part effecting directly the original vibration source, it dissipates vibrational energy from both sides. The MNT and the engine work as normal passive damping parts. In other words, the ActBrg approach does

MNT passive	$Power_{ups} > Power_{dns}$	$Power_{ups} < Power_{dns}$
(-inf, 0)	520	none
[0, 1)		none
[1, inf)		none
Engine passive	$Power_{ups} > Power_{dns}$	$Power_{ups} < Power_{dns}$
(-inf, 0)	520	none
[0, 1)		none
[1, inf)		none
HPR active	$Power_{ups} > Power_{dns}$	$Power_{ups} < Power_{dns}$
(-inf, 0)	520	none
[0, 1)		none
[1, inf)		none

Table 4.7.: Damping effect of the HPR, the engine and the MNT with active bearing

not change the role of other parts, due to its effectiveness at the beginning of the transmission path.

This indicates that the role of the HPR can be changed from a passive to an active part when the internal struts or the MNT are actuated (in the ActInSus and ActExSus approaches), while the passive damping effect of the internal struts and the MNT would not be changed when the HPR serves as the active part in the system (in the ActBrg approach). A reasonable inference for the role change of the HPR is that the HPR is the source of the original vibration and has to be affected directly (in the ActBrg approach) or indirectly (in the ActInSus and ActExSus approaches), no matter which part of the system is actuated.

Damping effect on translational and rotational power in the front and in the rear

While the discussion above shows how the actuated part influences the damping effect of each part in the WEM, the paragraph below will investigate how

these active systems reduce the vibration transmitted through different DOFs and positions. Fig. 4.10 shows how the power is transmitted through the front and rear links as translational and rotational power in the uncontrolled system and how the transmission mechanism is changed in the active systems with the three approaches.

In the uncontrolled system, the power from the HPR is transmitted mainly as translational power through the rear bearing B4, and in the high frequency range, the front bearing B3 absorbs energy as displayed by the negative blue line in Fig. 4.10a. There is little rotational power through all suspension except for few frequencies through the FUL and FLL and the high frequency range above 130 Hz through the RMR, as the red lines show. The rotational power through the MNT is approximately one tenth of the translational power through the MNT.

Comparing Fig. 4.10a and Fig. 4.10b, there is little change in the translational power through the bearings and in the rotational power through the FUL and FLL; primarily, rotational power through the RMR is reduced with the ActExSus approach. At a closer look, it can be found that the translational power through the RMR slightly increases and the power in both translational and rotational DOFs through the MNT is diminished. Accordingly, it shows that this approach leads to the vibration at the end of the transmission path, i.e. at the JntFL, being attenuated by restraining the rotational movement of the RMR, the rear junction between the MNT and the engine.

With the active internal suspension approach (Fig. 4.10c), the rotational power of the FUL, FLL and RMR is largely lessened, as well as its translational counterpart, which can be seen under greater magnification. At a higher magnification, the plots also show that the power through the MNT is reduced in all DOFs, which can also be inferred based on the conclusion from the preceding discussion that the MNT functions as passive damping when the ActInSus approach is applied in the system: The power through the FUL, FLL & RMR is largely reduced, and so is the power at the downstream position through the MNT. The translational power through the bearings is reduced in the middle frequency range of 100 Hz − 200 Hz. In the high fre-

quency range the roles of the front and rear bearings are swapped at 240.5 Hz. In other words, the front bearing transmits and the rear bearing dissipates vibrational energy. With the ActInSus approach, not only can the vibration at downstream positions be reduced, but also that at the source, the HPR, especially in the middle frequency range.

With the active bearing approach (Fig. 4.10d), the power in both forms at all positions is reduced. The front bearing transmits vibration with a positive value of power in the high frequency range, rather than dissipating energy as in the uncontrolled system. In this active system, both bearings carry less energy in all the frequency range, thus diminishing the total energy into the downstream part through this actuation approach.

In summary, with the ActExSus approach, the vibration is attenuated at the end of the transmission path by restraining the rotational movement of the RMR, while the ActInSus approach affects the power transmission at all positions by reducing the absolute value of power in both forms, i.e. less transmission and also less absorption. In this respect, the ActBrg approach is similar to ActInSus, with the exception that the attenuation of the vibration transmitted through the front links is generally greater than that with the ActInSus approach, and its effectiveness on the rear links is less than ActInSus. The translational power through the front links of the MNT and through the FUL and FLL is reduced to a negative value in some frequency ranges. Consequently, the ActBrg approach reduces the total power transmitted into the fuselage by having the front internal and external suspension absorb energy due to its lesser effect on the rear links.

4.3.3. Importance of rotational degrees of freedom in cost functions

As discussed above, the vibration is transmitted through translational and rotational DOFs. All the tests above took both into consideration in optimization. In this section, it will be discussed if or in which case the rotational DOFs can be ignored. This question is related to the decision about the number of sensors.

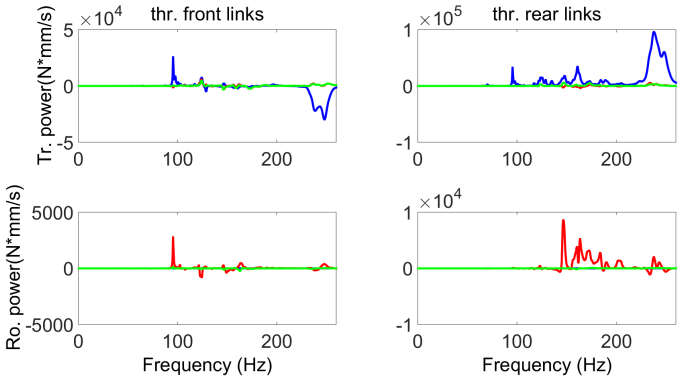

(a) in uncontrolled system

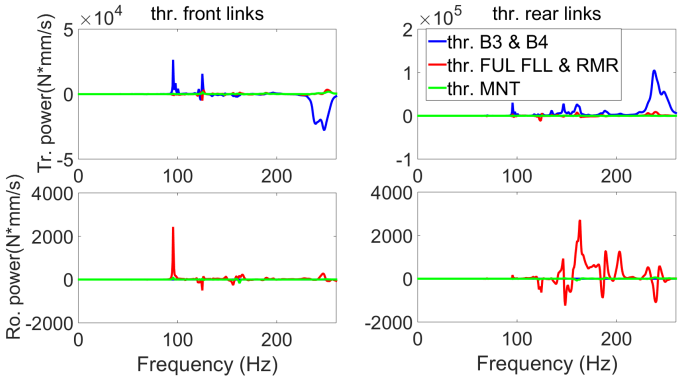

(b) with active external suspension

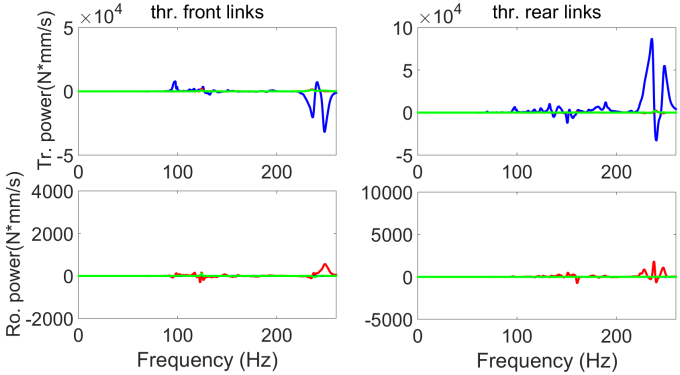

(c) with active internal suspension

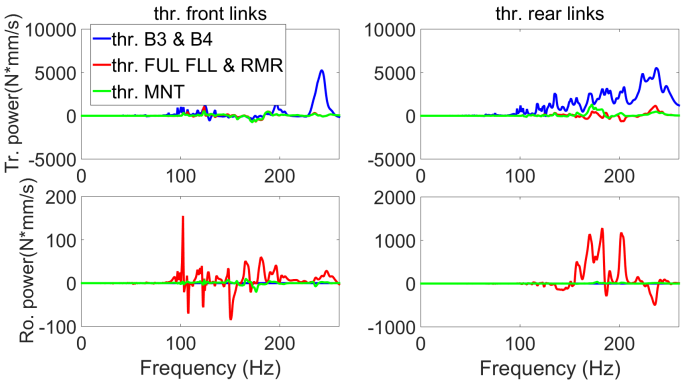

(d) with active bearing

Figure 4.10.: Power transmission through front and rear links in terms of translational and rotational power

No rotational power is transmitted through B3 and B4 in these systems. The importance of rotational DOFs of the internal and external suspension can be seen in Fig. 4.11: The effectiveness of optimizing a physical quantity only in translational DOFs is compared with that in both translational and rotational DOFs in the ActExSus and ActInSus approaches. All the plots are results in terms of power in all DOFs at each suspension position.

With the ActExSus approach (Fig. 4.11a), the optimization position is JntFL. When the power should be optimized, optimizing only the translational power is insufficient in the frequency range of 100 Hz − 150 Hz, yet there is little difference in the high frequency range. Thus, it appears that the rotational power through the MNT in the high frequency range is much lower than the translational power so that it can be neglected in the optimization, and the rotational movement of the MNT above 150 Hz is much less pronounced than that in the frequency range below 150 Hz. The second column of Fig. 4.11a shows that rotational DOFs are not critical when optimizing the squared acceleration, because the rotational acceleration is much lower in value than the translational one. Although the rotational accelerations scarcely count in the computation due to their low value, the results in terms of power in both translational and rotational DOFs are not worsened

considerably, comparing column 1 and column 2 in Fig. 4.11a. Considering the combination of forces and velocities as the objective, the system can be slightly less attenuated without considering rotational DOFs in the optimization, also in the high frequency range. This is probably due to the fact that the sum of the squared moment and the scaled squared rotational velocity in this objective function could not be neglected in the optimization computation as was possible for the squared rotational acceleration in optimizing the squared acceleration.

Different from the ActExSus approach, the results of the ActInSus approach shows that optimizing power only in translational DOFs through the FUL, FLL & RMR is not acceptable in the whole frequency range. This may be due to the non-negligible rotational movements of the FUL, FLL & RMR. When optimizing the squared acceleration with the ActExSus approach, it is not critical in the selection of translational or both translational and rotational DOFs for objective function. From the non-negligible rotational power and negligible rotational acceleration, it can be inferred that the moments are large and the rotational movements are small. The optimization strategy in the last column in Fig. 4.11b indicates that when considering rotational DOFs, it would even yield disadvantages in the high frequency range around 240 Hz, presumably because the high values of the moments or the high scaled rotational velocities are weighted too much in the optimization cost function and the actual power transmitted in rotational DOFs is relatively low. This can be improved by adjusting the scaling factor of the velocities.

Based on the analysis above, it can be concluded that the importance of rotational DOFs is different for two approaches and also for different optimization strategies. The different characters of the internal and external suspensions can be summarized as follows: The FUL, FLL & RMR transmits power both in translational and rotational forms, neither of which should be neglected in the whole frequency range, while the rotational power may be ignored through the external suspension in the high frequency range. In other words, the MNT would not be much rotationally excited but on the FUL, FLL & RMR translational and rotational movements are always coupled. Regarding the three control strategies, optimizing power with the ActExSus

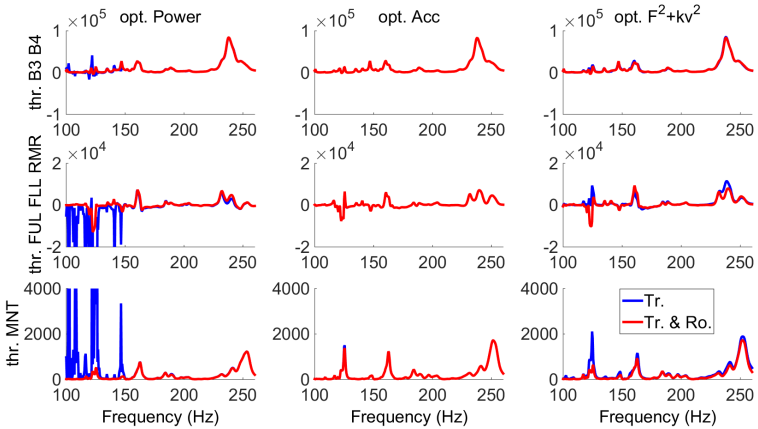

(a) Active external suspension

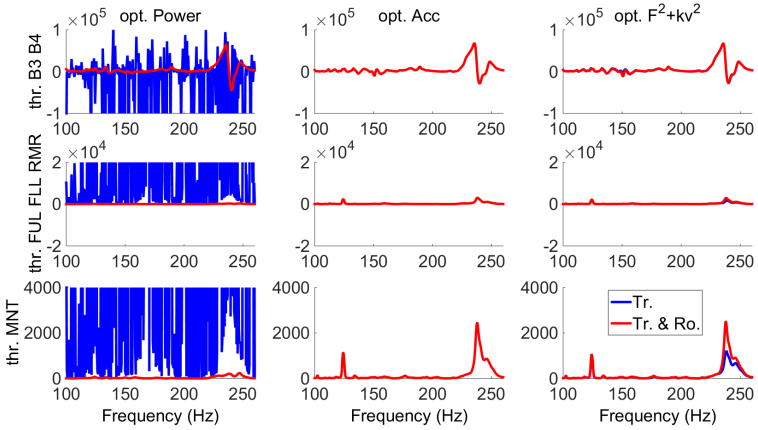

(b) Active internal suspension

Figure 4.11.: Power transmission (N*mm/s) showing the importance of rotational DOFs: Column 1 - optimizing power; Column 2 - optimizing the squared acceleration; Column 3 - optimizing combination of the squared force and squared velocity; Tr. - considering only translational coordinates; Tr.and Ro. - considering both translational and rotational coordinates

approach at high frequencies and optimizing the squared acceleration with both approaches show flexibility in selecting the DOFs to be optimized, and acceleration as the objective variable would be the best choice in the further study because it yields good effectiveness and does not require measurement in rotational DOFs. With the ActInSus approach, though, optimizing power is very sensitive to the rotational DOFs. Optimizing the combination has opposite results with two approaches, which may be due to the scaling factor and was not further investigated in this study. Comparing all of the plots in Fig. 4.11, optimizing power in all DOFs with the ActInSus approach brings about the best result. Optimizing the squared acceleration with the ActInSus approach is also better than that with ActExSus at most of the frequencies, but has a higher peak around 240 Hz.

4.3.4. Gyroscopic effect on active systems

The analyses until now have not taken the gyroscopic effect into consideration, so as to observe the influence of single factors, such as physical quantities or rotational DOFs. Here the gyroscopic effect will be discussed as a single variable. In Fig. 4.12 the power transmission at four stages and in uncontrolled and controlled systems is presented in rows and in columns, respectively, when optimizing the squared acceleration.

In the uncontrolled system, the response in power with the gyroscopic effect is basically shifted to the right compared with that without the gyroscopic effect, and the magnitude is increased between 150 Hz and 200 Hz.

In the active system with ActExSus, the gyroscopic effect has influence on the system similarly to the uncontrolled system with respect to the input power and the power through B3 & B4, since the actuation is outside the engine and far away from the rotor. With the ActInSus approach, the power from the rotor is reduced even to negative values due to the gyroscopic effect at the resonances around 240 Hz (see rows 1 & 2, column 3 in Fig. 4.12). The gyroscopic effect does not influence the system with the ActBrg approach much below 190 Hz, but shifts the resonance around 200 Hz to the right and reduces the highest resonance around 235 Hz. The reduction could result from the interaction between two rotors when the gyroscopic effect is considered

(Section 3.5.1).

The gyroscopic effect shifts the response of the uncontrolled system and increases it at some frequencies. Its influence on the controlled systems are mainly the following: When the actuation is outside the engine (ActExSus), the gyroscopic effect influences the system similarly to the uncontrolled system; when the actuation is inside the engine (ActInSus & ActBrg), it makes the part upstream to the actuated part absorb energy actively at the resonances around 240 Hz (rows 1 & 2, column 3 and row 1, column 4 in Fig. 4.12). Moreover, regarding these resonances, the ActInSus and ActBrg approaches prove to be more effective on the upstream positions in a rotating system (with gyroscopic effect) than in non-rotating system (without gyroscopic effect).

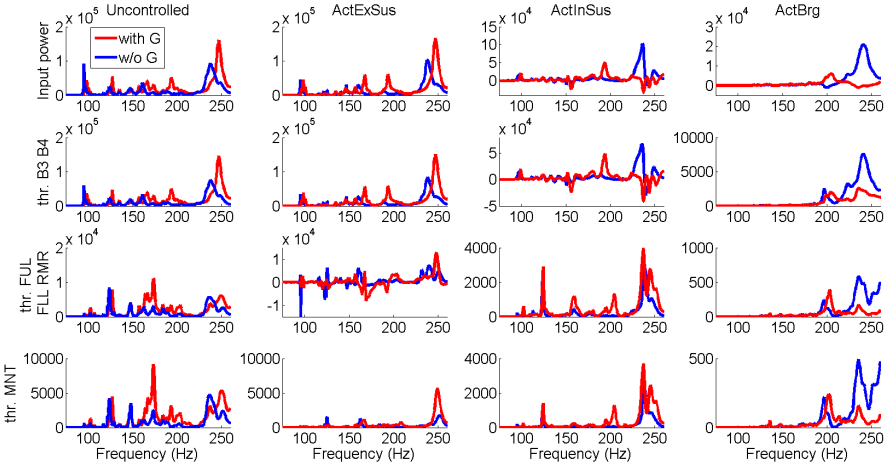

Figure 4.12.: Power transmission (N*mm/s) in Model 1 showing the gyroscopic effect: Column 1 - Uncontrolled; Column 2 - Active external suspension; Column 3 - Active internal suspension; Column 4 - Active bearing; with G - considering gyroscopic effect; w/o G - considering no gyroscopic effect

4.3.5. Interaction between squeeze film dampers and active systems

In Section 3.5.3, the effect on the system due to the installation of SFDs and actuators was discussed. Here the effects of the passive SFDs and the activated actuators will be compared.

To investigate the effect of the SFDs and the interaction with the actuation in active systems, the responses in the power transmitted through the MNT in seven systems are compared: Three systems without SFDs with three actuator placement approaches applied and four systems with SFDs with the three approaches applied (two of them are for ActBrg approach; in one, SFDs and actuators are in a parallel connection and in the other in a serial connection). And Fig. 4.14 magnifies the plots of the three ActBrg approaches. The gyroscopic effect is considered in all the systems. Fig. 4.13 shows the comparison in terms of the power transmitted through the MNT into the fuselage.

Generally, SFDs as passive damping attenuate further the vibration which is reduced by active methods, comparing the dotted lines and the solid lines. It is worth noting that the resonance at 237 Hz is increased by the actuation of both ActInSus cases (red). This may be due to the inconsistency between the evaluation variable (power through the MNT) and the optimization objective (the sum of the squared accelerations at FUL, FLL & RMR). At these resonance frequencies, the acceleration alone on the engine side cannot well represent the transmitted vibrational energy and the force plays a non-negligible role, which is consistent with the conclusion in Section 4.3.1.

To find out if the improper sensor placement strategy (insufficient types of physical quantities or improper sensor positions) is the cause of the increase of resonance at 237 Hz, different control strategies with ActInSus and SFDs were tested and compared with the uncontrolled system with SFDs and the controlled system with ActExSus and SFDs (Fig. 4.15). As discussed above, optimization of the squared acceleration at the FUL, FLL and RMR brings about more vibration in terms of the power transmitted into the fuselage at 237 Hz (comparing the blue line and the black line in the left plot). From the

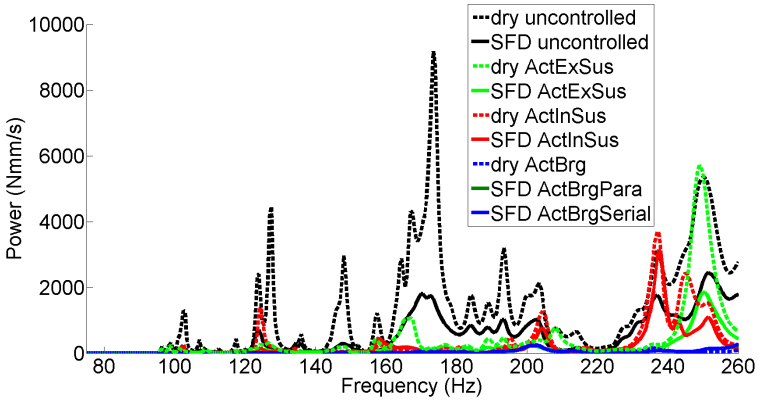

Figure 4.13.: Power transmitted through the MNT in systems with different damping methods

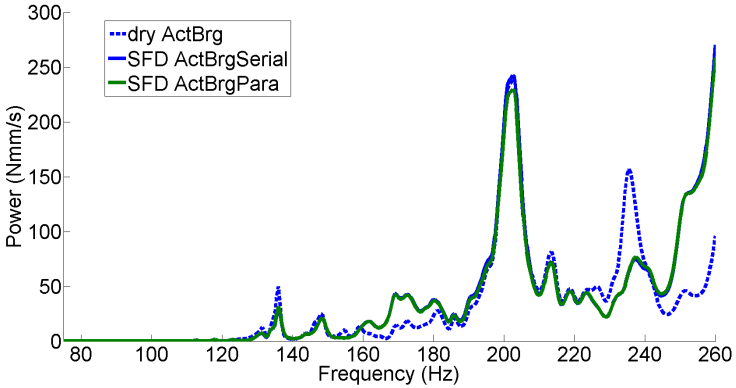

Figure 4.14.: Power transmitted through the MNT in systems with active bearing approach

red lines, it can be inferred that this worsening phenomenon can be avoided by changing the targeted positions of optimization to the MNT on the fuselage size, because this is at the end of the transmission path and the power there is also used as the evaluation criterion. Comparing the blue lines in both plots, it can be seen that when using a collocated control strategy, i.e. actuating the internal suspension and feeding back sensor signals at the FUL, FLL & RMR, optimizing both the squared force and squared velocity (blue line in the right plot) can avoid the worsening phenomenon. Comparing the red and the green lines, it can be seen that the ActInSus approach is more effective than the ActExSus approach, when the MNT is targeted in the optimization.

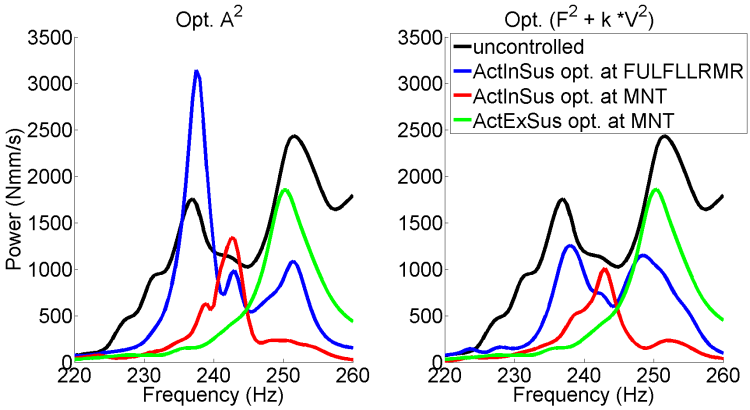

Figure 4.15.: Power transmitted through the MNT in systems with ActInSus and ActExSus, with different optimization targets applied

In the case of ActExSus without SFDs, a increased resonance also appears around 250 Hz (green dotted line in Fig. 4.13). Comparing the green lines in both plots in Fig. 4.15, it can be seen that the performance of the system with ActExSus cannot be improved by additional force sensors when only a simple scaling factor k is used in the optimization target. This worsening phenomenon shown by the green dotted line could be presumably avoided when a suitable scaling method is found for the strategy of optimizing the combination of the squared force and squared velocity or when the strategy

of optimizing the power is applied. This will not be discussed further, since the ActExSus system without SFDs will not be on the focus in this study.

The effectiveness of ActBrg is the same either with actuators and SFDs in a parallel connection or in a serial connection (see the overlapping dark green and blue solid lines in Fig. 4.14), only that the actuation effort is higher with the parallel configuration, since the actuation forces need to overcome more stiffness. Comparing them with the case without SFDs, as shown with the blue dotted line, it can be inferred that the active method to reduce the vibration is dominant in almost the whole frequency range, and additional SFDs only bring attenuation to the active system at around 235.5 Hz. Between 159 Hz and 182 Hz and above 250 Hz, the additional SFDs have a negative effect on the system response. The reason could be that these SFDs were designed for the system without actuators installed at the bearings and could not exert the same effect on the systems with the active bearing.

4.4. Questions and discussion

In this section, conclusions will be summarized by answering or discussing several questions.

How should the robustness of the passive systems be evaluated? (Fig. 4.4)

The robustness of the systems with SFDs is higher than that without SFDs, and the effectiveness of the SFDs could be weakened by the parallel installed actuators with high stiffness. Moreover, the lower the stiffness of the bearing is, the more robust the system could be. However, a soft bearing is not advantageous to generate effective actuation. Assuming that the robustness of Model 3 is the standard, which is the current state of the engine, only Model 4 with actuators and SFDs installed in series can meet the standard, and the others all need additional measures to ensure the operation of the activated actuators or to improve the robustness of the inactivated system.

Which physical quantity in which situation should be used in the cost function? (Section 4.3.1)

If the sensor techniques allow measuring both forces and velocities or accelerations with high precision, the power generated in all DOFs would be suggested as the controlled physical quantity for the generally best performance among the four quantities. If both forces and velocities can be measured but the accuracy of the phase difference cannot be ensured, then power cannot be precisely computed, and the combination of the squared force and squared velocity would be the choice as the targeted quantity, because of its better performance than optimizing the squared acceleration, e.g. Fig. 4.15. It would be suggested that the scaling factor should be adjusted. If the signals of the forces are not available, then acceleration would be suggested. Optimizing the squared force alone is not recommended for the ActBrg and ActExSus systems, due to its little improvement or negative effectiveness on the system at most of the frequencies.

How should the three actuator placement approaches generally be judged? (Section 4.3.2)

The ActExSus approach works in restraining the rotational movement of the RMR and prevents the power being transmitted further into the fuselage. Although the MNT is not directly connected to the vibration source (the HPR), the actuation of the MNT effects the vibration source in such a way that it makes the power input due to the unbalance from one position distributed along the HPR. The ActInSus approach is effective at all positions along the transmission path. It provides attenuation not only to the downstream part but also to the vibration source in the low frequency range below 220 Hz, and it exerts its effect not only on the input power but also on the power transmitted through B3 and B4. ActBrg reduces the vibration at the source and thus the power transmission at all positions along the transmission path. Due to its position at the front, it has less influence on the power transmitted through the rear links and effects the front links so that they absorb energy with power in a negative value, and the total power transmitted is reduced.

Generally, the optimized actuation through the MNT prevents rotational movement of the whole engine, exerting little influence on the power trans-

mission inside the engine, while the ActInSus and ActBrg approaches exert the effect of vibration reduction on more positions of the transmission path. ActBrg is more effective than ActInSus in the frequency range above 220 Hz and vice versa. It could be inferred that at the frequencies above 220 Hz, the eigenmodes of the HPR are more involved, which corresponds to the conclusion about the influence of the gyroscopic effect of the HPR (Fig. 3.13), and the lower frequencies are more strongly related to the eigenmodes of the engine. ActBrg reduces the vibration at the source, but does not have any further effect when the vibrational energy is spread in the engine and excites the eigenmodes of the engine. On the contrary, ActInSus can effect the resonances of the HPR less than ActBrg, but has more potential to attenuate the vibration at the eigenfrequencies where the eigenmodes of the engine are more involved.

Are the sensor signals of rotational DOFs necessary in the active control system? (Section 4.3.3)

It depends on the actuator placement approach and the control strategy. When optimizing power, they are necessary in the frequency range of 100 Hz − 150 Hz with the ActExSus approach, while the necessity is expanded to the whole frequency range with the ActInSus approach. When optimizing the squared acceleration, they are not required, and the same for optimizing the combination of the squared forces and squared velocities.

What kind of role does the gyroscopic effect play in the actively controlled system? (Section 4.3.4)

When the actuation is outside the engine as with ActExSus, the gyroscopic effect does not interact with the actuation and influences the system similarly to the passive system without actuation. However, when the actuation is inside the engine as with ActBrg or with ActInSus, the interaction between the gyroscopic effect and the actuation makes the parts which are located upstream to the actuated part actively absorb the energy at the resonances around 240 Hz.

How should the seven active systems be judged based on the analysis in this chapter? (Section 4.3.5)

The seven active systems rank according to the absolute power transmitted through different suspension parts in the frequency ranges lower than 220 Hz and higher than 220 Hz, as listed in Tables 4.8 & 4.9. The best effectiveness in vibration reduction is numbered as 1 and so forth. The reduction values in dB in terms of the power transmitted into the fuselage are acquired by comparing each active system with the current state of the engine, i.e. the open-loop system of Model 3 with SFDs. This evaluation of the reduction level at the end of the transmission path will be compared with the results based on different control algorithms in Chapter 5, while the reduction values in terms of the power transmitted through the other parts are not quantitatively examined. The ActBrg approach without SFDs is the best overall. When the SFDs designed for the original system are added in this ActBrg system, i.e. ActBrgPara and ActBrgSerial, there is no further reduction except at the resonance around 235 Hz. It could be inferred that these SFDs are not adapted for the ActBrg system. If the system is intended to replace the passive damping with the active method, it can be seen among the first three systems that ActBrg is the best.

System	Ranking		Reduction in dB	
	<220 Hz	>220 Hz	<220 Hz	>220 Hz
dry ActExSus	6	7	4.4	-7.4
dry ActInSus	7	6	2.2	-3.6
dry ActBrg	2	1	17.5	23.8
SFD ActExSus	1	4	18.5	2.4
SFD ActInSus	5	5	7.5	-2.2
SFD ActBrgPara	2	2	17.9	19.5
SFD ActBrgSerial	2	2	17.4	19.1

Table 4.8.: Ranking of seven active systems with respect to the transmitted power through MNT

ActBrg either with or without the SFDs is optimal among all systems. ActInSus and ActExSus have their advantages and disadvantages, mainly

System	thr. FUL FLL RMR		thr. B3 & B4	
	<220 Hz	>220 Hz	<220 Hz	>220 Hz
dry ActExSus	7	7	7	7
dry ActInSus	5	6	6	5
dry ActBrg	3	1	1	1
SFD ActExSus	6	4	4	5
SFD ActInSus	4	4	4	4
SFD ActBrgPara	1	2	2	2
SFD ActBrgSerial	1	2	2	2

Table 4.9.: Ranking of seven active systems with respect to the transmitted power through FUL, FLL & RMR and through B3 & B4

concerning the vibration transmission inside the engine and at the end of the transmission path. ActExSus is the closest to the evaluation points, the MNT, which causes its good effectiveness in the low frequency range, however, when the mode of the HPR is more involved in the high frequency range, it is much weaker than ActBrg.

The controls in the systems ranked here are all designed as collocated configurations. As discussed in Section 4.3.5, if the sensor signals at the MNT or the signals in force additional to the signals in acceleration at the FUL, FLL & RMR can be fed back in the application of ActInSus, it would be even better than ActExSus (Fig. 4.15). Therefore, it is expected that ActInSus would outperform ActExSus with proper sensor placement strategies, e.g. with the presence of sensors at the MNT or an observer with which the response at the MNT can be estimated or additional force sensors at the FUL, FLL & RMR.

Can the present application of the SFDs be completely replaced by the active control method? (Section 4.3.5)

Regarding the robustness, it is not recommended to replace the SFDs completely without implementing further measures, because only the system with SFDs and actuators installed in serial is comparable to the current system only with SFDs (Fig. 4.4). However, the optimized responses of the closed-

loop systems show that all the actively controlled systems with or without SFDs are comparable to the current system exclusively with SFDs (Fig. 4.13). Based on these optimization results, it is suggested to replace the SFDs when the robustness of the system can be ensured by other measures, in case that the active system fails.

If only the front side or rear side of ActInSus is activated, would the effectiveness be severely affected?

This question is raised for an inside view of the ActInSus approach and to find out if the number of actuation positions can be reduced when applying this approach.

As shown in Fig. 4.16, the rear actuation alone is generally better than the front actuation alone and almost overlaps the result of actuating both the front and the rear, except for the frequency range above 250 Hz. The effectiveness of ActInSusFront is comparable above 200 Hz to the case of ActInSus in which both sides are actuated, but a lot worse in the lower frequency range. It can be inferred that the effect of the rear actuation is dominant below 200 Hz, the effect of the front actuation above 250 Hz and with both of them between 200 Hz and 250 Hz.

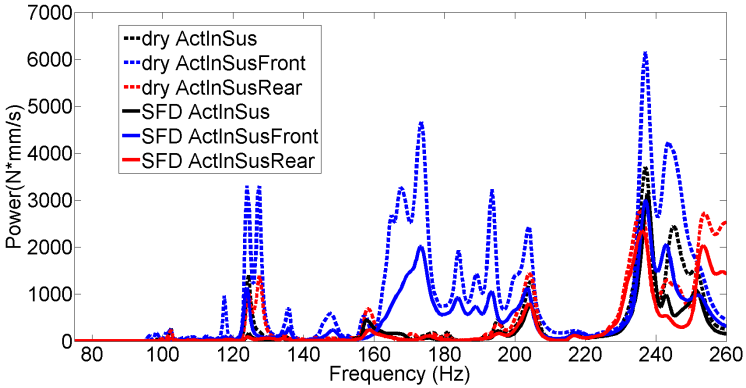

Figure 4.16.: Power transmitted through the MNT with active internal suspension showing the respective importance of front and rear actuation

Which cases should be selected for the further study on control design?

Based on the analysis and discussion on robustness, physical quantities, actuator placement approaches, the importance of rotational DOFs, the gyroscopic effect and the effect of the SFDs and actuation, the following decisions are made for the further investigation in control design.

- The translational acceleration should be the main sensor signal and the force signal should also be additionally collected when it yields better performance.

  The optimal results with acceleration as the physical quantity in the cost function are almost as good as those with power, and acceleration is not sensitive to the rotational DOFs. However, the as good effectiveness of optimizing the squared forces as optimizing the squared acceleration in the ActInSus system shows the potential of forces as sensor signals to reduce the vibration. In the collocated system with ActInSus (Fig. 4.15), the additional force signals render the active system more effectiveness. Under such conditions, force sensors should also be taken into consideration.

- Collocated control should be mainly considered, as described in Table 4.1 & shown in Fig. 4.1, and non-collocated control should be considered for ActInSus.

  On the one hand, the investigation above is mainly focused on the optimization of collocated suspension systems (Table 4.1), on the other hand, collocated control design is easier, and the stability can be relatively easily ensured. However, since the non-collocated actuators and sensors can bring about more effectiveness in the application of ActInSus (Section 4.3.5), non-collocated control should also be considered for this approach.

- Three actuator placement approaches with SFDs working together should be investigated, and the parallel configuration of the ActBrg approach should not be considered.

SFDs should remain, not only for the interest of robustness, but also to provide more attenuation in the active systems with the ActInSus and ActExSus approaches, so that the gap with respect to the effectiveness of the vibration reduction is not too large between them and ActBrg, with reference to Table 4.8. The parallel configuration has the same effectiveness as the serial one but costs more actuation effort and thus should not be considered.

- The gyroscopic effect should not be neglected in the numerical analysis of the vibration transmission of active systems.

  In the previous chapter, the importance of the gyroscopic effect in the simulation on the passive systems of WEM was proved. Here for active systems, while it does not significantly influence the end of the transmission path outside the engine, its effect inside the engine is not negligible.

5. Application of control algorithms in the aircraft engine system

This chapter concentrates on implementing vibration reduction through active methods: Control design. Several control algorithms have been studied. Some of these will be selected and presented here, while the reasons for excluding the rest will be explained. The results will be shown for each actuator placement approach with different types of controllers and be compared with the results in Chapter 4. They are presented mainly in terms of power transmitted or acceleration at MNT junctions.

5.1. Comparison of control algorithms

In the current application of the active engine mount approach, Filtered-x Least Mean Square (FxLMS) algorithm and Filtered-u Least Mean Square have been successfully implemented for the active damping on the fuselage [6][57]. The FxLMS algorithm applied on WEM in this study also shows good effectiveness of vibration reduction. However, it depends highly on the precision of the model as a model-based control algorithm.

Using the H_∞ method, another model-based control algorithm, the precision of the model required for a good effectiveness is lower than that with the FxLMS algorithm, according to [59]. Its disadvantage is that a large number of iterations are needed to find the solution, therefore rendering the computation effort too great for large models.

Integral Force Feedback (IFF) controllers would be preferred when the stability is aimed, because it can be ensured by collocated pairs of actuators and sensors using IFF. This algorithm itself is very effective in reducing the forces which are fed back into the controller; however, the reduction in terms of acceleration cannot be guaranteed and neither can the vibration in terms

of power at the end of the transmission path.

The Linear Quadratic Regulator (LQR) seeks the optimal solution based on a quadratic function. The solution is dependent on the weighting matrix. More details on this algorithm will be provided in the next section. It suffers an implementation problem as it requires all states of the system to be fed back. Theoretically, this may be solved by an observer, however, that would create a new problem in designing such an observer for large systems.

Instead of requiring information on all states, only a number of outputs should be measured and returned to the output feedback control. The optimization procedure to find the optimal solution with this control algorithm [44] has been tested on the WEM, and the computation time turned out to be very long. On the one hand, each iteration took long due to the size of the system, on the other hand, the step size has to be small enough to ensure convergence, which may also be affected by the system's size..

These algorithms are summarized in Table 5.1 (listed in alphabetic order). Weighing their advantages and disadvantages, FxLMS, IFF and LQR were selected to be applied on the WEM, and the results will be presented here. LQR requiring all the states be fed back mainly cannot be implemented in reality and serves as a benchmark here: Because it seeks the optimal using the information of all the states, it is expected to give the best performance with appropriate weighting matrices.

5.2. Application of selected control algorithms on the whole engine system

The fundamentals of the aforementioned control algorithms can be found in the common respective literature about control, e.g. [51] [60] [44]. This section will mainly deal with the processes of how the three selections (Table 5.1) have been adapted to this study and applied on the WEM.

FxLMS

As shown in Fig. 5.1, the FxLMS algorithm filters the reference input through $W(n)$ to generate such actuation forces $u(n)$ (Eq. (5.1)) at the time step n

Algorithm	Advantages	Disadvantages	Selected or not
FxLMS	Good effectiveness	High model precision is needed	Yes
H_∞	It yields good effectiveness, and the model precision requirement is not high	Difficulty in finding the solution for large models	No
IFF	Stable as long as sensors and actuators are collocated	Collocation is not always possible	Yes
LQR	The solution can be adjusted with weighting matrices	All states are required to be fed back	Yes
Output feedback control	Only outputs are required to be fed back	Optimization procedure could take a long time	No

Table 5.1.: Advantages and disadvantages of control algorithms tested on the WEM

that the errors can be minimized, which is consistent with the optimization target in the study on ideal effectiveness in the last chapter. The adaptive filter $W(n)$ is updated in each step by the product of errors and the estimated reference input (Eq. (5.2)), based on the least mean square algorithm. ρ is the step size, which determines the property of convergence. $\tilde{x}(z)$ is acquired by filtering the discrete-time signal $x(z)$ through the estimated secondary paths $\tilde{S}(z)$, which is the estimation of the secondary paths $S(z)$ representing the transfer function from the actuation to the sensor positions.

$$u\left(n\right) = W\left(n\right) x\left(n\right) \tag{5.1}$$

$$W\left(n+1\right) = W\left(n\right) + \rho e\left(n\right) \tilde{x}\left(n\right) \tag{5.2}$$

In the application of the FxLMS algorithm to reduce the vibration caused by the unbalance, the unbalance forces are set as the reference input $x(z)$. In the time domain, this can be represented by two sine wave signals with the amplitude of the unbalance force and the phase difference of 0.5π. The n_s errors in acceleration are measured at the receiver in each approach (see the circles in Fig. 4.1 for the positions of accelerometers). Each actuation approach

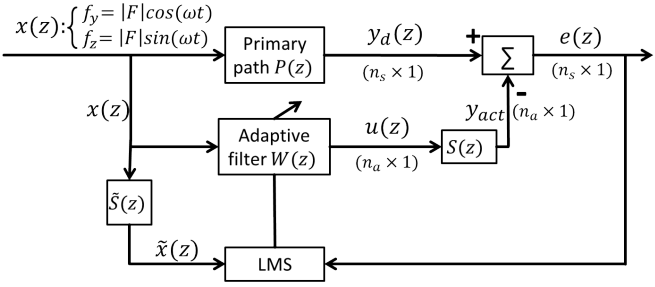

Figure 5.1.: The FxLMS algorithm adopted on the engine under the excitation of unbalance

provides different numbers of actuation forces (n_a), and correspondingly the size of the filter $W(z)$ changes.

This algorithm has been tested with the steady-state excitation, i.e. both rotors rotating at constant speeds.

IFF

This algorithm requires a displacement actuator and a force sensor to be collocated. The interlacing pole-zero configuration on the imaginary axis starting with a zero arises in the system controlled by IFF. All the loops in the root locus diagram are located in the left half plane, which ensures the unconditional stability of the closed-loop system with all values of the gain g (Eq. (5.3)).

$$C_{IFF}(s) = -g/s \tag{5.3}$$

As depicted in Fig. 5.2, the signals of the force sensors F_{sen}, collocated both in position and in direction with the corresponding actuators, are fed into the controller, and the actuation forces F_{act} are generated and fed into the system. All outputs y_{out} in acceleration and force at suspension positions should serve as the outputs for the calculation of the transmitted power.

LQR

The LQR algorithm is one of the optimal control algorithms. As in Fig. 5.3

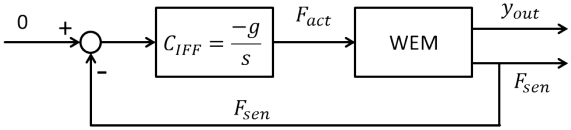

Figure 5.2.: Simple illustration of the IFF control algorithm

indicates, states of the system x are returned to the controller K_{LQR} to generate the actuation forces F_{act} as in Eq. (5.4), which is designed to minimize the value of the cost J defined in Eq. (5.5). The cost function considers both the outputs y_{out} and the actuation effort F_{act} with the weighting matrices Q and R.

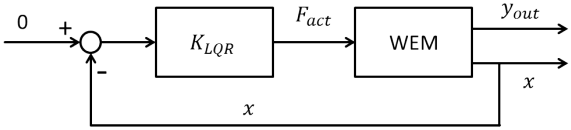

Figure 5.3.: Simple illustration of the LQR control algorithm

$$F_{act} = -K_{LQR}x \tag{5.4}$$

Substituting $y_{out} = C_{ss}x + D_{ss}F_{act}$ for the general case where the feedthrough matrix D_{ss} is not zero, Eq. (5.5) can be re-arranged as

$$J = \int_0^\infty \left(y_{out}(t)^T Q y_{out}(t) + F_{act}(t)^T R F_{act}(t) \right) dt \tag{5.5}$$

$$J = \int_0^\infty \left(x(t)^T Q_x x(t) + F_{act}(t)^T R F_{act}(t) + 2x(t)^T N F_{act}(t) \right) dt \tag{5.6}$$

Then K_{LQR} can be computed by

$$K_{LQR} = R^{-1}\left(B_{ss}^T P_r + N^T\right) \tag{5.7}$$

in which P_r can be found by solving the continuous time algebraic Riccati equation Eq. (5.8).

$$A_{ss}^T P_r + P_r A_{ss} - (P_r B_{ss} + N)R^{-1}(B_{ss}^T P_r + N^T) + Q_x = 0 \tag{5.8}$$

In the application of the LQR in this study, the weighting matrices Q and R are set as diagonal matrices, and Q is defined so that the targeted outputs can be kept as low as possible, under the condition that R guarantees the amplitudes of the actuation forces to stay below 10 kN. Presumably, this represents the limit of the potentially applicable piezoelectric actuator (the reason for selecting the limit of a piezoelectric actuator as the standard will be explained in Chapter 7).

5.3. Achievable vibration reduction with different actuator placement approaches

The three suspension systems corresponding to the three actuator placement approaches introduced in Table 4.1 were further investigated with the three aforementioned types of controllers applied.

With the LQR

The states in each system are fed back into the controller K_{LQR}. For the systems with ActBrg, with ActInSus and with ActExSus, the sizes of the controllers are 2×3790, 4×3768 and 3×3768, respectively. (There are 12 more states in the system with ActBrg, because of the serial connection between actuators and SFDs, for which additional nodes and DOFs are added, referring to Fig. 3.6)

Initially, constant weighting matrices Q and R with only diagonal elements were used, resulting in the actuation forces remaining below 10 kN. An overview of the effectiveness of each approach employing the LQR in terms of the transmitted power at the four stages is displayed in Fig. 5.4. ActExSus and ActInSus scarcely affect the vibration source as seen in the two plots above (the input power generated by the unbalance forces and the power transmitted through bearings), while ActBrg with its actuator positions at the bearings shows its ability to reduce the vibration at the source (see the blue lines). ActExSus reduces the vibration at the end of the transmission path in such a way that it changes the role of FUL, FLL & RMR to absorbers, especially between 150 Hz and 200 Hz (see the green line in the left bottom

plot).

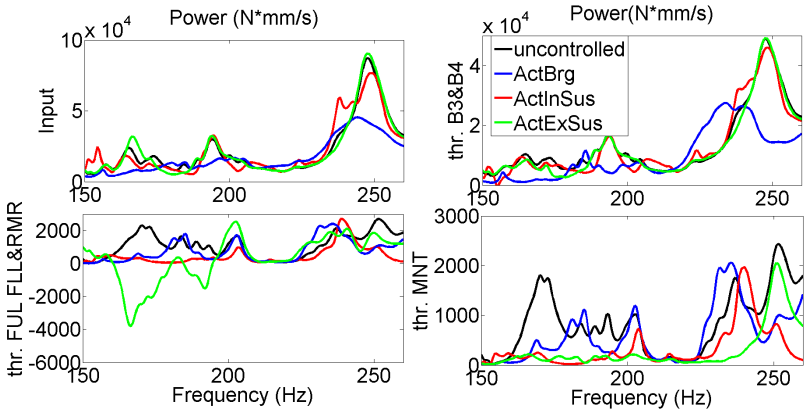

Figure 5.4.: Power transmission at four stages with the three actuation approaches when the LQR is applied

The power transmitted through the MNT into the fuselage is a consistent criterion to evaluate these three approaches, as depicted in the right bottom plot in Fig. 5.4. Generally, ActInSus & ActExSus present similar performance in the low frequency range below 200 Hz and prove to be better than the ActBrg approach, while all of them have high resonances which are only slightly lower or even higher than those of the uncontrolled system in the high frequency range above 230 Hz. ActBrg underperforms the optimization results. ActInSus and ActExSus stay in line with the expectations in Fig. 4.13: Good attenuation in the low frequency range and slight reduction or slight increase at resonances in the high frequency range.

Sensors and actuators are collocated in the ActInSus & ActExSus approaches, while ActBrg uses actuation only at B3 to control the acceleration both at B3 and B4 (Fig. 4.1). Lacking actuation in the rear but having the same weight in the weighting matrix for the front and rear at all the frequencies could account for ActBrg's general bad performance. It can be improved by adjusting the weighting matrices. Fig. 5.5 shows the power at the end of the transmission path, when R is kept the same as above, and the weight is assigned equally to the front and rear in Q as above (blue) or almost only

to the front (red) or to the rear (green). The performance in this critical frequency range 220 Hz – 260 Hz, for example, can be enhanced by assigning more weight in the weighting matrix to the front below 237 Hz and by assigning more weight to the rear above 237 Hz. However, all of these three are still not comparable to the optimized result in Fig. 4.13, and the weighting matrix should be adjusted further for a significantly better performance.

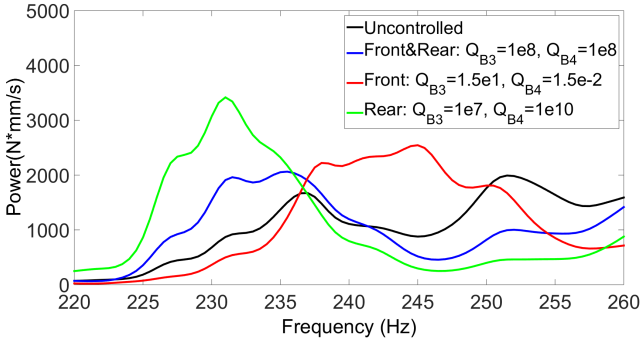

Figure 5.5.: Power transmitted into the fuselage when the LQR is applied with different weighting matrices in the active bearing approach

The advantage of ActBrg from the optimization results cannot be made full use of, when the LQR algorithm is applied without tuning the weighting matrices specifically. However, the conclusions about the other two approaches do not deviate much from those in Chapter 4. In Fig. 5.6 different optimization strategies are compared based on the optimization in Chapter 4 and the LQR. The green lines almost overlap each other, indicating that the potential of the ActExSus approach can be fully exploited with the LQR. The resonance around 240 Hz is shifted in the ActInSus system based on the LQR, compared with the optimization results. The frequency shift and the lower resonance in the ActInSus system with the LQR compared with the optimal result can be attributed to the change of the system's dynamic characteristics when the LQR is integrated. The performance improvement by replacing the targeted points at the FUL, FLL & RMR with those at the MNT is still true when employing the LQR, as concluded from the optimization results. The ranking among these three actuator and sensor placement strategies also re-

mains as it was in Chapter 4: ActExSus is better than ActInSus when using the collocated control, while ActInSus yields a better reduction effectiveness than ActExSus when the MNT is targeted instead of the FUL, FLL & RMR.

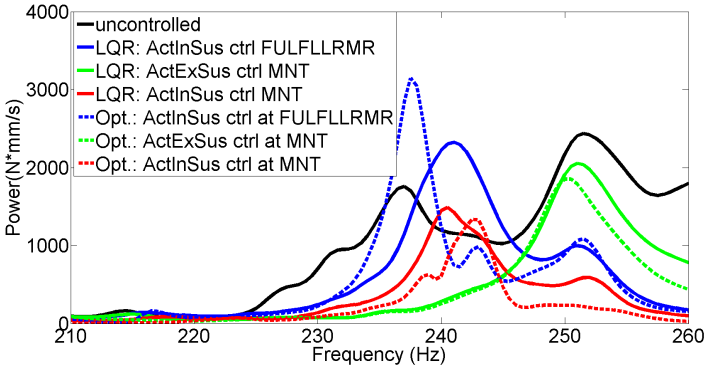

Figure 5.6.: Power transmitted through the MNT in systems with ActInSus and ActExSus: Results based on the optimization (Chapter 4) and on the LQR algorithm

With the IFF control

Implementing the IFF control requires the collocated sensor and actuator pairs to be used to guarantee stability. The ActBrg approach was tested only with the front bearing actuated and collocated force sensors applied, and the power transmission was much reduced in the front but much increased in the rear. It was inferred that the vibration through the rear bearing cannot be neglected and the control in the front alone is not sufficient. Thus only the other two approaches are presented here with the IFF control. Force sensors are collocated with actuators at the FUL & FLL and the A-frame links 1 & 2 in the ActInSus approach and the two rear links of the MNT in the ActExSus approach.

The sensors are placed on the A-frame links 1 & 2 (in green boxes of Fig. 2.2) instead of on the RMR, so as to be collocated with the actuation. Only the two rear links of the MNT are actuated in the ActExSusRear approach. The reason can be seen in Fig. 5.7 (refer to the numbering of links

in Fig. 2.3): The blue lines represent the power through the six links of the MNT when link 2 in the front and links 5-6 in the rear are all actuated, i.e. except the links which transmit the thrust (links 3 & 4) and the yoke (link 1), and the red lines represent only the links in the rear being actuated. According to that figure, there is little difference in terms of the power through links 2-6 between these two actuation approaches, while link 1 is more excited around 250 Hz when the front link, i.e. link 2, is excited. It means that the effort at link 2 to attenuate the local force can lead to a greater power transmission at link 1, which represents the connection between the yoke and the fuselage. Therefore, it was decided to use the results from the case with only rear actuation in the ActExSus approach when investigating the IFF control.

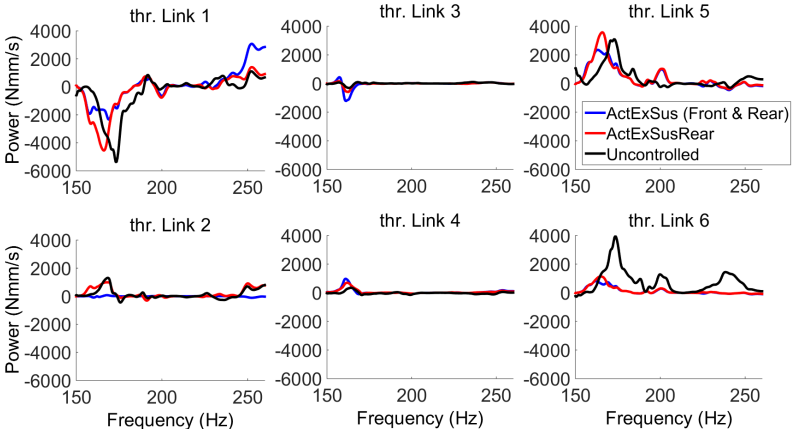

Figure 5.7.: Power transmitted through each link of the MNT when different actuation strategies of ActExSus are applied, based on the IFF control

As depicted in the two plots above in Fig. 5.8, under the IFF control, there is little effect on the power transmission on the HPR with either of these two actuation approaches. ActExSus is capable of attenuating the power through FUL, FLL & RMR at two resonances, 184 Hz and 237 Hz, but not much at other frequencies, while ActInSus is effective over a wider range. At the end of the transmission path, i.e. through the MNT, they share the same tendency

as through FUL, FLL & RMR. Generally, the ActInSus approach is superior to ActExSus regarding the effective frequency range and the magnitude of attenuation.

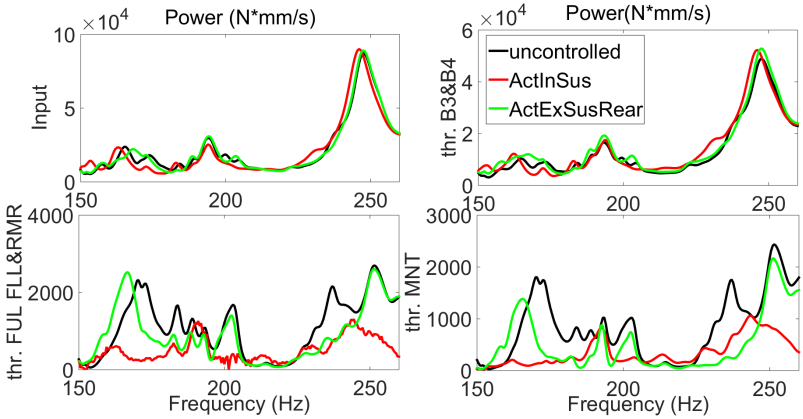

Figure 5.8.: Power transmission at four stages with ActInSus and ActExSus when the IFF control is applied

With the FxLMS algorithm

The time responses of each active system to the steady-state excitation of the unbalance of 1000 gmm with rotors rotating at constant speeds, based on the FxLMS algorithm, are recorded and processed with the Wattmeter method [13] to extract the information in the frequency domain at the frequency of the HPR's rotational speed. The sampling rate is 7000 Hz. The results are recorded until they converge. The rate of convergence depends on the step size ρ (Eq. (5.2)). Here, the step size is tuned for each frequency so that the active system is kept stable and the results converge as fast as possible. Generally, the higher the rotational speeds are, the faster it will converge. Among these three approaches, it converges much faster with ActBrg ($0.5\ s - 1.5\ s$) than with the other two ($1\ s - 4\ s$ with ActExSus and $5\ s - 7\ s$ with ActInSus). The accelerations at B3 & B4, at FUL, FLL & RMR or at the MNT, respectively, are considered as the errors to update the filter coefficients (Eq. (5.2)), when ActBrg, ActInSus or ActExSus is employed.

Based on the settings described above, the frequency response to the unbalance can be generated, as presented in Fig. 5.9 in terms of the transmitted power at the four stages. Similar to its LQR counterpart, the actuation in the ActExSus approach rarely acts on the beginning of the transmission path (see the green lines in the two plots at the top) and causes the FUL, FLL & RMR to absorb energy at some frequencies (see the green line in the plot at the left bottom). Unlike the LQR, the reduction at the HPR with ActInSus can be achieved to some extent (see the red lines in the two plots at the top), and the relative flat blue lines in all plots indicate ActBrg's best performance.

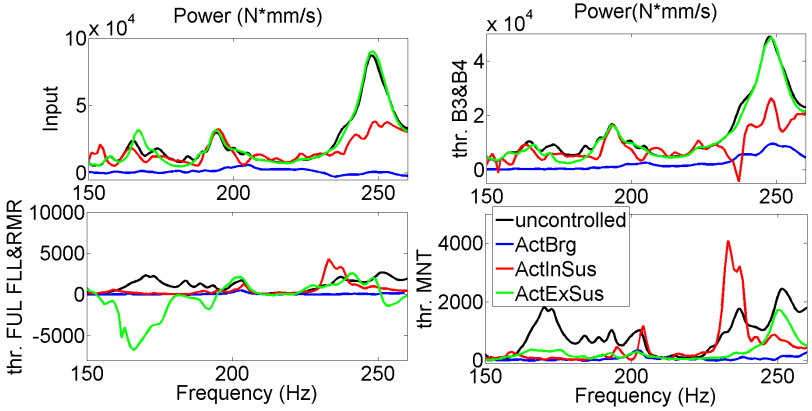

Figure 5.9.: Power transmission at four stages with the three actuation approaches when the FxLMS algorithm is applied

In order to learn to which extent the FxLMS algorithm can exploit the potential of each actuation approach, the results are compared with those based on the optimization in terms of the transmitted power through the MNT, as shown in Fig. 5.10. The generally similar trends and comparable amplitudes between the solid and dotted lines highlight a good agreement between the achievable and the ideal effectiveness with the help of the FxLMS algorithm. A noticeable difference, though, is the worsening phenomenon with ActInSus (refer to Section 4.3.5) appearing in a wider frequency range, $230\,\mathrm{Hz} - 240\,\mathrm{Hz}$, when the FxLMS algorithm is applied.

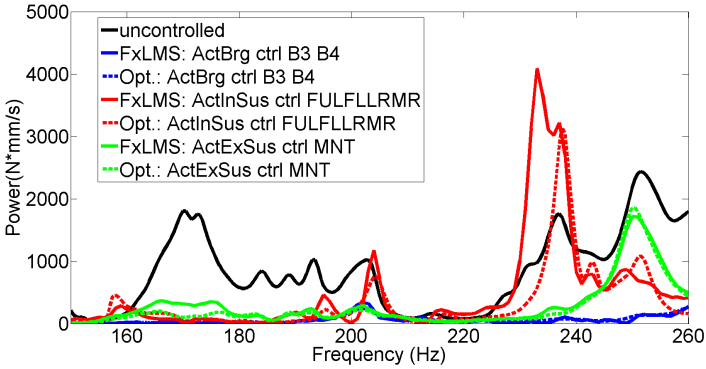

Figure 5.10.: Power transmitted through the MNT in systems with three actuation approaches: Results based on the optimization (Chapter 4) and on the FxLMS algorithm

Apart from ActBrg with its absolute advantage in nearly the whole frequency range, it is worth comparing the ActInSus and ActExSus approaches under the same condition. Fig. 5.11 presents the power transmitted through the MNT in the higher frequency range, where higher resonances manifest, under different sensor placement strategies. When ActInSus is used to control the acceleration at the FUL, FLL & RMR, it underperforms the open-loop system in the range of 230 Hz − 240 Hz. However, using the accelerations at the MNT as error signals considerably improves the effectiveness of the ActInSus approach, surpassing even ActExSus, without the worsening phenomenon.

5.4. Vibration reduction effectiveness with different controllers

The previous section explored how effective the three approaches can be with different controllers. Here, the results will be compared to determine which controller achieves the best reduction performance for each approach. The three approaches with the sensors at the same stage of the actuator positions and the ActInSus approach with the sensors placed at the MNT have been

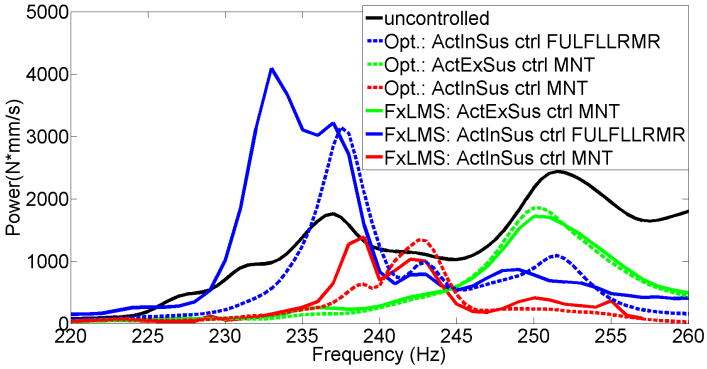

Figure 5.11.: Power transmitted through the MNT in systems with ActInSus and ActExSus and different sensor placement strategies: Results based on the optimization (Chapter 4) and on the FxLMS algorithm

studied.

Reduction levels

Different reduction values are listed in Table 5.2. Regarding the reduction at the cruise phase (225 Hz), which is the most relevant to the passenger comfort, FxLMS performs the best with ActBrg and the worst when ActInSus collocated system is applied. It yields the comparable effectiveness with the LQR in the other two actuation approaches. LQR in brackets in the tables means that it gives good results but not feasible in reality. The ActInSus system controlling the FUL, FLL & RMR has the best performance with the IFF control with a very low reduction level. But when the acceleration at the fuselage side is fed into the FxLMS algorithm, ActInSus performs almost as well as ActBrg, 4 dB better than ActExSus.

Regarding the highest resonance amplitude above 150 Hz, it shows that the FxLMS algorithm is advantageous for most of the actuation approaches, while LQR is the weakest. Up to 17.35 dB can be achieved with the FxLMS algorithm applied in ActBrg, which also provides the best case with the highest reduction among all the combinations of approaches and controllers. With

ActInSus, the FxLMS algorithm raises the resonance even above that of the uncontrolled system, while the IFF control yields a reduction of 7.22 dB, approx. 40% of the best case. The ActInSus and ActExSus systems controlling the acceleration at the MNT show approx. 20% of the reduction of the best case under FxLMS.

Besides the cruise frequency, the highest resonance frequency and the high frequency range, several other frequencies are also noticeable when comparing those actuation approaches in Fig. 5.12. While ActBrg showing a good reduction almost over the whole frequency range keeps a resonance at 200 Hz, both ActInSus approaches eliminate this resonance at 200 Hz. The reason is that this is an eigenfrequency of the non-rotating part of the engine close to the FUL, FLL & RMR, other than the HPR. It can be proved by Fig. 3.17, in which it shows that different bearing configurations do not alter the resonance around 200 Hz. The worsening phenomenon with ActInSus when applying the FxLMS algorithm is similar to the optimization results in Fig. 4.15. In this frequency range, the deformation of the mount system including the FUL, FLL & RMR is more involved in the excited mode, so that the forces cannot be controlled by reducing the accelerations at the junctions between the MNT and the engine and the energy flow cannot be attenuated. This can also be confirmed by the good effectiveness of ActExSus in this range. Moreover, ActInSus can be improved by directly reducing the acceleration errors at the fuselage side, as shown in the plot on the right hand side in Fig. 5.12. The incapability of ActExSus around 250 Hz can be explained with the help of Fig. 5.7: Links 2, 5 & 6 are actuated but can hardly reduce the power through link 1, which represents the connection between the yoke and the fuselage. It can be inferred that the dynamics of the yoke is more excited around 250 Hz and can hardly be controlled by actuating MNT. It can be improved by reducing the vibration earlier in the upstrem part, e.g. with ActBrg or with ActInSus.

An overview of the vibration in terms of the power carried through the MNT can be found in Fig. 5.12. Comparing the frequency responses of the closed-loop system and the open-loop system at each frequency, the average reduction values in the critical range 220 Hz – 260 Hz are listed in Table 5.2c.

Reduction at 225 Hz (dB)	ActBrg ctrl B3&B4	ActInSus ctrl FUL FLL&RMR	ActExSus ctrl MNT	ActInSus ctrl MNT
LQR	*-5.24*	*1.92*	*10.21*	*16.34*
IFF	-	1.59	6.25	-
FxLMS	17.07	0.34	10.15	14.06
Best	FxLMS	IFF/(LQR)	FxLMS/(LQR)	FxLMS/(LQR)

(a) The reduction during the cruise

Reduction of the highest resonance(dB)	ActBrg ctrl B3&B4	ActInSus ctrl FUL FLL&RMR	ActExSus ctrl MNT	ActInSus ctrl MNT
LQR	*1.44*	*1.87*	*1.47*	*4.28*
IFF	-	7.22	1.01	-
FxLMS	17.35	-4.50	3.03	4.89
Best	FxLMS	IFF	FxLMS	FxLMS

(b) The reduction of the highest resonance

Average reduction (dB)	ActBrg ctrl B3&B4	ActInSus ctrl FUL FLL & RMR	ActExSus ctrl MNT	ActInSus ctrl MNT
LQR	*1.16*	*6.26*	*9.60*	*10.08*
IFF	-	4.71	6.90	-
FxLMS	29.06	2.44	9.93	12.97
Best	FxLMS	IFF/(LQR)	FxLMS	FxLMS

(c) The average reduction in the range of 220 Hz − 260 Hz

Table 5.2.: Reduction in terms of the power transmitted through the MNT, with different actuator placement approaches, based on LQR, IFF & FxLMS, respectively

Similar to the investigation above, most of the best results are based on the FxLMS algorithm, and ActBrg with FxLMS proves to be the best case. The ActInSus and ActExSus approaches with FxLMS show approx. 40% of the reduction of the best case. In terms of the average reduction, the ActInSus approach is more effective with the LQR algorithm than with the other two, indicating a reduction of approx. 20% as the best case. Considering the reduction values in both criteria in the two tables, it is suggested that the IFF control be more suitable for ActInSus when designed to control the vibration at the FUL, FLL & RMR.

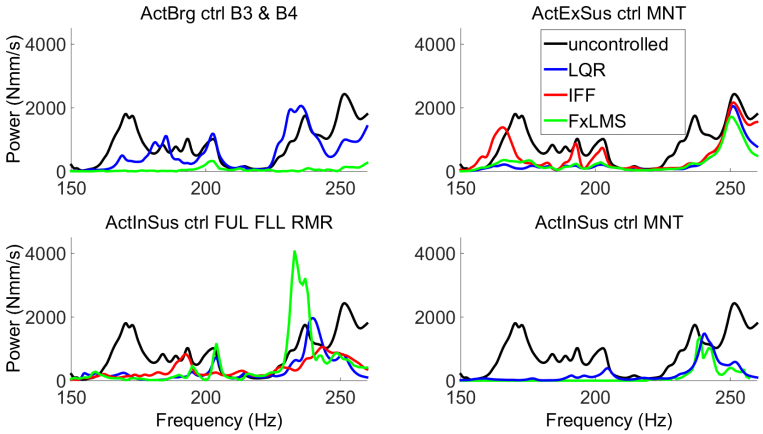

Figure 5.12.: Power transmitted through the MNT with the three actuation approaches based on the LQR, IFF & FxLMS

To sum up, since the FxLMS algorithm works well for most of the actuation approaches in this investigation, it proves very promising for the application of active systems on aircraft engines. Comparing the three approaches for which the FxLMS algorithm is the most effective control algorithm, it leads to the following ranking from the best to the worst: ActBrg, ActInSus controlling the acceleration at the MNT and ActExSus. When ActInSus controlling the vibration at the FUL, FLL & RMR with the IFF control is added, it ranks the second regarding the reduction of the highest resonance and the last regarding the average reduction and the reduction during the cruise. LQR's

poor performance is due to the rough tuning of the weighting matrices. As a state feedback control algorithm requiring full states to be observable, it can be used with well-adjusted weighting matrices for performance evaluation on the simulation level, instead of being implemented.

Model uncertainty in the FxLMS algorithm

It is stated in [59] that high accuracy of the secondary model estimation is required for good performance of the FxLMS algorithm. Here it will also discuss how the uncertainty of the model will influence the reduction effectiveness through this algorithm. Phase and amplitude uncertainties were separately introduced into the secondary path and the results from three active systems to which this algorithm provides good performance are presented in Fig. 5.13, in terms of the power transmitted into the fuselage.

Generally, this algorithm is much more robust to amplitude errors than to phase errors when applied on the WEM. It was found through the manually tuning process that with higher phase errors in the model, it needs smaller step sizes to ensure stability and accordingly longer time to converge. The ActInSus system is more sensitive to model uncertainty compared with the other two. The tests of uncertainty on this system were only performed until 20%, because it was very difficult to converge or convergence became too slow since 20% of phase error. And compared with the uncontrolled system, this phase uncertainty results in 1.5 dB less reduction than the ActInSus system without phase error. The ActExSus system can endure the phase error until 40% with 1.5 dB less reduction and the ActBrg system until 30% with 3 dB less reduction.

5.5. Questions and discussion

How were the control algorithms selected for investigation? (Table 5.1)

Several common control algorithms were explored and compared. Generally, not all of them are suitable for the aircraft engine system, mainly due to its computational complexity. FxLMS, IFF and LQR were selected, because the control design based on these algorithms could be carried out on the

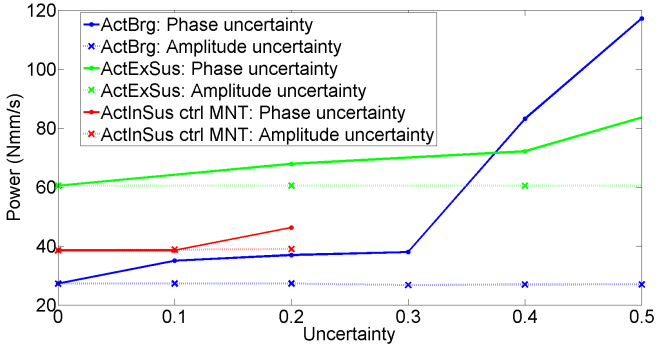

Figure 5.13.: Power transmitted into the fuselage during the cruise with model uncertainties in the FxLMS algorithm

large model and a certain effectiveness in the vibration reduction could be achieved.

What is the suitable control algorithm for each actuator placement approach?

The FxLMS algorithm is suitable for ActBrg and ActExSus, but not for ActInSus at some frequencies when targeting the acceleration reduction at the FUL, FLL & RMR in the closed-loop system. However, when the signals at the MNT on the fuselage side can be fed into the controller, i.e. ActInSus controlling the MNT, the FxLMS algorithm proves also able to cause the active system to attenuate the vibration effectively at all frequencies. Otherwise, the IFF control is appropriate for ActInSus controlling the FUL, FLL & RMR.

According to the achieved reduction effectiveness based on the control algorithm, how are the three approaches evaluated?

ActBrg yields at least more than twice the reduction of its counterparts (Table 5.2). ActInSus has no absolute advantage against ActExSus, when it is designed to control the vibration at the FUL, FLL & RMR: Regarding the reduction of the highest resonance, ActInSus doubles the reduction of ActExSus, while ActExSus is twice as effective as ActInSus regarding the average of

reduction. However, under the same condition of the sensor placement, i.e. controlling the vibration at the MNT, ActInSus shows its absolute advantage (approx. 1.5 of the reduction of the ActExSus approach), considering the reduction of the power transmitted into the fuselage.

What are the advantages and disadvantages of the suitable control algorithm for each approach?

The advantage of the FxLMS algorithm lies firstly in coming close to achieving the ideal optimal effectiveness discussed in Chapter 4. The numerical uncertainty study shows that it can tolerate at least 20% phase error. Its requirement of the model precision should be further investigated, when it is implemented in practice. Moreover, the step size needs to be tuned for several frequency ranges, and its rate of convergence depends on the actuation approaches and tends to be slow. Therefore, the basic FxLMS algorithm cannot produce a stable attenuation in an average run-up test, in which the rotational speeds rise within a relatively short time and the frequency of the unbalance excitation changes, but it is only effective in a test where the excitation is steady-state, i.e. the rotational speeds are constant.

IFF has the stability advantage, due to the collocation of actuators and sensors, and it benefits from the easy manual tuning of the controller gain. When employed with the ActInSus approach, four actuators and four sensors should be attached to the FUL & FLL and the two A-frame links close to the RMR. The implementation is easy, but the reduction effectiveness is much lower than the other approaches based on FxLMS during the cruise.

6. Verification and discussion of active vibration control methods in an aircraft engine system

Chapter 2 summarized the state of the art in two respects: Applications to reduce the vibration from the engine and research methods on an active system. In the analysis in Chapters 4 & 5, the current applications, i.e. SFDs as a passive damping method (open-loop system of Model 3) and active engine mounts (ActExSus) as an active reduction method, were each compared with the two proposed active approaches. In this chapter, the research methods, with which the results in Chapters 4 & 5 were generated, will be discussed in comparison with the results from past studies.

6.1. Active suspension systems

Before discussing the systems in past studies and here, it is worth distinguishing the working principles of passive and active mounts. Generally, an ideal vehicle mount should be capable of transmitting low-frequency forces, but incapable of doing so for high-frequency forces. The former forces refer to the static loads to maintain the alignment specification due to the vehicle acceleration, and the latter to the vibratory forces. In other words, the stiffness of the mount should be large enough to support static loads and low enough for dynamic loads. Thus, the passive mount should reach a compromise to achieve a certain vibration isolation. Since the damping of the mount can prevent excessive vibration at the resonance while at the same time degrading the high-frequency isolation performance of the passive mount [66], the expectation of its effectiveness should not be high. The benefit of active mounts is that they are not limited by these theories, because they do not

respond passively to the excitation.

Past studies using the same optimization method to study active suspension systems as in Chapter 4 were briefly reviewed in 2.3.2. Their main conclusions are listed below and compared with the results of the three suspension systems (Table 4.1) in the previous chapters:

1. The strategy of optimizing the total power, both linear and rotational power, is ideally the best. [18] [33] [31] [32]

   This statement is also true for the three suspension systems in this investigation as shown in Fig. 4.7, 4.8 & 4.9. It was also stated in [18] that this strategy can yield an average power reduction of 30 dB, in which a two-mount suspension system with multiple degrees of freedom was investigated. 43.0 dB, 17.9 dB and 14.3 dB can be achieved in the ActExSus, ActInSus and ActBrg systems, respectively. Moreover, it was demonstrated in [33], investigating the power transmission from a rigid body to a cylindrical shell, that the power transmission can be completely canceled when the moments are not present. The ActBrg system using only linear bearings as the suspension and cylindrical engine as the receiver can be seen as a comparable system. However, the power transmitted through the bearings is not eliminated completely, yet it reaches a reduction of 17.1 dB regarding the highest resonance within the frequency range of interest. The reason could be that only the front bearing is actuated.

2. Controlling the power transmitted only through part of the DOFs can bring about power circulation, i.e. the control forces reduce the measured power at the expense of increasing the power through other DOFs. This is also why the strategy of optimizing the power is sensitive to flanking paths, through which the vibrational power travels in addition to the main transmission path but is not measured, even if the power through flanking paths is low in the open-loop system. [18] [31] [32]

   This conclusion holds true with the two active suspension systems in which both the linear and rotational power are involved in the vibration transmission through the suspension. The cost function accepts nega-

tive values indicating that the power is absorbed from the receiver, and this absorbed power can be supplied to the receiver through the DOFs which are ignored in the optimization. Fig. 4.11 shows that ActExSus is sensitive only in the low frequency range, while the performance of ActInSus is far worse than the passive system in the whole frequency range, when only linear power is targeted in the optimization. The rotational DOFs are not easily excited at the MNT above 150 Hz. This is different from the conclusion in [17] that the power transmitted through moments in that simple system can be neglected at low frequencies, but that it increases with the frequency. It can be inferred that the DOFs which are difficult to excite can be neglected in optimizing the power, however, this condition cannot always be guaranteed in a real system.

3. The results from optimizing the combination of the squared force and squared velocity is comparable with those from optimizing the power. In addition, they have the advantage of robustness to measurement errors, e.g. phase errors, regarded as a more reliable and practical solution. [18] [33] [32]

   It was explained in [18] that optimizing the forces and velocities simultaneously yields a good effectiveness in their suspension system, because the resonances are excited at different frequencies when they are minimized separately and optimizing the combination can avoid this problem. This improvement can be clearly seen at the max. take-off frequency in the ActBrg system. However, such a better performance is not generally present in Fig. 4.7 4.8 & 4.9: To be precise, the optimization of the combination can only improve the result from the optimization of the squared acceleration alone at several resonances. The main reason is that the scaling factor in this investigation was only adjusted as one constant for all the frequencies, aiming at minimizing the highest resonance and also ensuring that it was not so large as to yield the same performance as optimizing the squared acceleration. Considering the similarity of results of optimizing the squared acceleration and optimizing the combination leads to the inference that, unlike the conclusion above for the simple suspension systems, the ex-

cited frequencies from optimizing the squared force and the squared velocity do not differ much. Furthermore, the force in the optimization does not always prove beneficial in reducing the highest resonance in these three systems.

4. The minimization of the squared linear acceleration or the squared linear force performs nearly as well as the minimization of the total power, even with the presence of rotational moments. [18] [31]

   It was proved on a simple system in [31]: An adaptive control method was used to achieve the optimal reduction and a locus of filter coefficients indicating the 0 power could be drawn, on which the points representing the optimal set of filter coefficients corresponding to the minimization of the square acceleration and of the squared force can be found. Optimizing the squared acceleration yields similar results to optimizing the power in the ActBrg and the ActExSus system, while in the ActInSus system, there is a difference of approx. 20 dB. This gap indicates how important the contribution of the force is to the optimization and the necessity of an optimal scaling factor for optimizing the combination of the squared force and squared velocity with the ActInSus approach. The respective improvement can be seen in Fig. 4.15 displaying the responses of the systems with SFDs while considering the gyroscopic effect. Fig. 4.11 proves that the minimization of the squared linear acceleration reaches nearly as good a performance as the minimization of the total power with the ActExSus approach with the presence of moments, but not so good with the ActInSus approach. Optimizing the squared force yields the worst performances in the ActBrg and ActExSus systems, showing lesser effectiveness and/or negative influence in most of the frequency range. For example, there is almost no improvement in the ActBrg system in the low frequency range. In other words, the motion of the junctions between the HPR and the other parts of the engine is still much excited, although the forces at the bearings are minimized. This indicates that the other parts, excluding the rotor, are much involved in the modes of these frequencies. Similar reasons can be used for the other systems.

5. The control effort to minimize the power is less than that needed to minimize the acceleration or the force. [31]

   Due to the poor results from optimizing the squared force, said option will be excluded from this discussion. Comparing the effort to minimize the power and the squared acceleration, this conclusion applies only to the high frequency range of the ActBrg system. However, it is noticeable that the optimization of the combination of the squared force and squared velocity, yielding similar results to the optimization of the squared acceleration, requires less effort in the low frequency range of the ActExSus system and in the whole frequency range of the ActBrg system.

6. The actuation should be applied near the source, while sensors near that source are not effective in controlling the downstream; instead, using signals directly from the fuselage is more effective. [67]

   Fig. 4.13 shows that among these three approaches, ActBrg is the most effective, in which the actuation is at the source. In Fig. 4.15, it can be seen that directly targeting the vibration at the MNT close to the fuselage side improves the performance of ActInSus. This agrees with the conclusion in [67] that accelerometers near the engine-to-pylon interface (corresponding to the FUL, FLL & RMR) appear to be ineffective while those at the pylon-to-wing intersection (corresponding to the MNT) are effective.

7. Large reductions occur not uniformly at all sensors, but at individual spots. [67]

   This holds generally true for the multi-input multi-output system. For example, Fig. 5.7 shows that the reduction at link 5 is different from that at link 6 in the range of $150\,\mathrm{Hz} - 200\,\mathrm{Hz}$.

6.2. Performance of control algorithms

The application of controllers on a rotating system was discussed in Section 2.3.3, and will be compared with the results from Chapter 5 as follows.

1. A feedforward adaptive control system, e.g. the FxLMS algorithm, provides the potential to bring about the maximum achievable performance. [33] [34] [46] [30] [61]

   As shown in Table 5.2 and Fig. 5.12, the FxLMS algorithm represents the best control algorithm in the selection. The reason is that a conventional gradient descent algorithm would converge towards the global minimum. In [34], it was stated that the experimental results from an actively controlled beam rig with an FxLMS implementation showed good agreement with the optimization results. It was proved numerically in this investigation that, as compared in Fig. 5.10 & 5.11, the results based on the FxLMS algorithm can well represent the optimum.

2. Due to the inaccurate estimation of the secondary path, it converges slowly or may even easily become unstable. [34] [59]

   In this investigation, the slow convergence was also present in the three active systems with the three approaches. The uncertainty study numerically shows that the FxLMS algorithm applied in the whole engine system can endure up to 20% phase errors in the model with a compromise of 3 dB less reduction. And the higher the errors are, the slower the results converge and easily go unstable.

3. The stability of the IFF control applied on the active bearing of an aircraft engine was proved numerically and experimentally on a test rig of a rotating machine. [7]

   In [7], the IFF control was applied on a test rig of a rotating system. Only one end of the rotor was actuated by the IFF control. The reduction effectiveness at the active bearing and at a sensor position close to the active bearing showed good performance. However, the vibration at the passive bearing through which the vibration was further transmitted was not discussed. Moreover, the rotor in that experiment had fixed boundary condition, while the HPR in this study is connected with a flexible whole engine system. Therefore, it is stated based on the numerical analysis that the IFF control is not applicable to the ActBrg approach in the WEM when only the front bearing is actuated.

However, this study proves that this unconditionally stable control algorithm is applicable to the ActInSus and ActExSus approaches, as long as actuators and sensors are collocated, and it provides ActInSus with good performance.

7. Feasibility study

This chapter will focus on the implementation of the active methods on the aircraft engine, investigating potential problems and/or suggestions regarding the selection and integration of the hardware, the design of the controller for a real engine system, etc.

7.1. Space and environment of active internal suspension approach

Taking a twin-spool engine for example, the space at the three positions is shown in Fig. 7.1 & 7.2, respectively. The hollow area is 100 mm wide and 300 mm long. The cross-section resembles a convex lens, in which an actuator with a diameter of 25 mm can be fitted. As for the rear, the application in [4] can be used, that is, three piezoelectric stack actuators (Fig. 7.2) are attached to the link so that they are at 120° angles to each other and the extension direction is along the length of the link (see the right hand side in Fig. 7.2). The forces and even bending moments can be introduced into the link: A deflection in the longitudinal direction, a lateral bending deflection in any direction and the torsion of the link. As an application in the actuation system in the engine, the torsional DOF will not be considered but the other two can be used.

The temperature changes with the measurement point in the engine and with the phase of the flight. The flight can for example go through the following phases: Taxi, take-off, climb, cruise, step climb, cruise, descent, approach, thrust reverse and taxi. It is supposed that the struts directly after the fan share the temperature of the bypass flow. It is ca. 20 °C − 35 °C during the cruise phase, considered a stationary state and most relevant to passenger comfort. Regarding the transient operation, the extremes occur

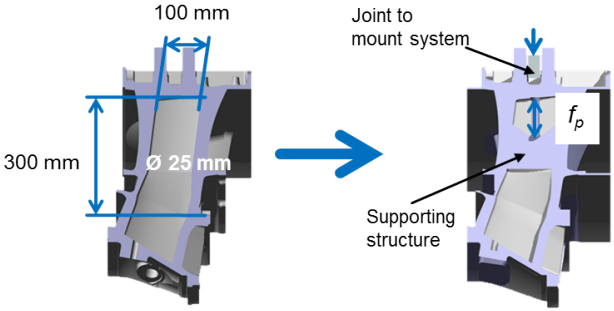

Figure 7.1.: Left: Original strut in IMC; Right: Strut in IMC with supporting structure [42]

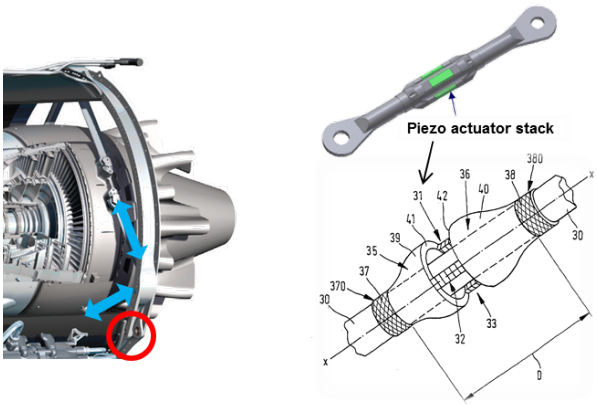

Figure 7.2.: Left: Rear actuation (indicated as double arrows); Right, top: Actuator application on the link; Right, bottom: Invention of piezoelectric extension actuator [4] *(numbers will not be explained, except 31, 32 and 33 - piezo stack actuators)*

at the end of the take-off phase, ca. 80 °C, and at the end of descent, ca. −15 °C.

In the rear, the links for actuator placement are surrounded by the bypass flow, emitted from the struts in the IMC. Since it is neither further compressed after the fan nor does it pass through the combustor chamber, the temperature of the flow should not to be much higher than at the exit of fan. Because of the great mass of this bypass flow, the influence on the links from the hot components of the core engine through heat convection is very limited. However, when the engine stops the operation, the heat convection from the hot core engine will be dominant without bypass flow.

7.2. Space and environment of active bearing approach

As described in Section 3.2, the bearing chamber is connected in series with the IMC through bolted junctions in the current passive configuration. The space for actuators was identified, and two alternatives to integrate actuators were proposed, either influencing both B2 and B3 or B3 alone. In case of overload, for the former, the overload protection housing (not shown in Fig. 3.4) is necessary, which should operate in parallel to the actuator, while it is not required for the latter, because the force would be transmitted through the small gap of the SFD between the SC and the IMC, so that the actuator can be relieved, avoiding mechanical damage through the high forces. Otherwise, another concept introduced in [10] can also be considered, in which vibration isolators are mounted on the engine case and coupled to a rotor bearing assembly disposed within the engine case, rather than directly affecting the rotor.

As mentioned in Section 2.1, the temperature in the rear area, where B4 lies, is much higher than in the front, where B3 is located. Taking a twin-spool engine for example, it can reach 220 °C at B4, while B3 it is does not encounter more than 90 °C, during the phase of climb. The temperature would be lower during the cruise phase, when it is less loaded, compared with climb phase. The temperature range from −15 °C to 80 °C at the exit

of the fan can be referred to as the temperature at B3 as well, for B3 is at the entry of the HPC, following the exit of the fan (see Fig. 2.1 for engine structures).

Therefore, application at B4 is not feasible without a cooling system, since the operating temperature of actuators generally does not exceed 200 °C (refer to [19]) and actuators cannot perform well or last a long time under high temperatures. This research gives preference to an application of actuators at B3, which was analyzed in the previous chapters.

7.3. Actuator selection

As stated in [66], if an actuator is attached to a link or a strut in series, it is required to provide a low-frequency stroke and high-frequency force. An electrodynamic actuator might be suitable. Otherwise, when in parallel, a stiff, low stroke actuator, e.g. a piezoelectric actuator, can satisfy the force/deflection requirements. The actuator placement approaches in this study employ a parallel configuration (although ActBrg uses a serial connection with B3, it is parallel to B4, which is also integrated into the mount between the HPR and the other part of the engine). Therefore, the piezoelectric actuators are selected. Moreover, a piezoelectric actuator has also the advantage of small size and fits the small installation space inside the engine. Other advantages, such as high force generation and rapid response, will also yield benefits to the system.

The actuators should be chosen according to the dimensions and operating temperature range. They should fit into the space without much construction cost. The resulted temperature on the actuator depends on the environment and the operating condition, bringing with it different effects of self-heating. This is an important factor, because the thermal depolarization of the piezoceramic material will occur under high temperatures, while the low temperatures might, for instance, damage the glue between the piezoelectric discs. Considering these factors, the two types of piezoelectric actuators listed in Table 7.1 are selected for the two approaches inside the engine. Compared with ActInSus, more efficient actuators should be used for ActBrg, because

they are normally difficult to cool down. Actuators for the rear of ActInSus and ActExSus are not determined, since there is considerable freedom for their application on the links. The blocking force of the smaller one is 14 kN. The limit of actuation forces in Chapter 5 was assumed based on this value.

Approach	ActInSus (front)	ActBrg
Order number	P-025.80P	P-035.80P
Displacement (mm) (0-1000V) -10/+20%	0.12	0.12
Diameter OD (mm)	25	35
Length L (mm) +/- 0.5	113	114
Blocking force (0-1000V) (N)	14000	28000
Stiffness (N/mm)	120000	230000
Capacitance (nF) +/-20%	2600	5200
Resonant frequency (kHz)	10	10
Operating temperature range	-20 to 85 °C	-20 to 85 °C

Table 7.1.: Parameters of selected actuators

A cooling system for the actuators at B3 and in the front IMC struts can be designed, if the body heat of actuators should not be neglected due to the hysteresis effect. As presented in Fig. 3.4, the relatively cool air flows into the actuator from the front and out of the engine through the hollow space of the IMC strut. As for the rear A-frame links, a cooling system should be designed to ensure that the actuators are not damaged due to the high heat convection from the core engine after shut-down, without cool air flow.

7.4. Sensor selection and placement

Generally, sensors should be collocated with the actuators in each approach. As stated in [67] and proved in this investigation, sensors should be additionally placed at the fuselage side, for a better reduction effectiveness, although this may not be practical due to the complexity of installation, such as wire connection. As a rotating system, the information on the HPR's rotation is also necessary for some control algorithms, e.g. FxLMS. Therefore, a

tachometer at the HPR which is normally present is also essential in these active vibration control systems.

As concluded in [67], the most effective control pickups are the direct quantities being minimized. Here in this investigation, the acceleration was chosen as the optimizing target based on the analysis in Chapter 4, and accelerometers should be selected. For the IFF control, force sensors should certainly be used.

7.5. Implementation of controllers

In Chapter 5, the advantages and disadvantages of several control algorithms were discussed. Some experience regarding their implementation was also collected from past studies:

1. In [6], the time-domain filtered-U algorithm was employed on the active mount of the aircraft engine, and it was stressed that the implementation issue should be taken care of because a potential long-term divergence of the algorithm could be caused by the ill-conditioned transfer function matrices.

   In the process of designing the FxLMS algorithm for this engine system, it was found that manually tuning the step size for a stable and fast convergence was already difficult at some frequencies on the simulation level, especially when the actuators and the sensors are not collocated, such as in the case of ActInSus controlling the vibration at the MNT. This may be due to the unstable interaction with lightly damped resonances. When implemented, the step size should be kept relatively small, and it can also avoid the unwanted response to noise.

2. Due to the good effectiveness of the FxLMS algorithm and its instability, it was suggested that the feedforward control should be used for the vibration reduction and an additional IFF controller as an emergency system in [7].

   These properties of the FxLMS algorithm and the stability of the IFF control were also proved in this investigation. As long as the imple-

mentation of both algorithms is possible, this combination could be employed to ensure a good and stable reduction.

Therefore, with the ActInSus and ActExSus approaches, FxLMS and IFF would be recommended to act in tandem so as to compensate for each other's drawback based on the following working logic: The FxLMS algorithm is active for the reduction, and in case the system goes unstable, the IFF control should be activated. Typically, a FxLMS control system would require DSP (digital signal processor) with the ability of operate at 10^6 cycles per second, a low-pass filter, an A/D converter and a D/A converter [61]. As for the IFF control, the collocated actuators and force sensors are required.

The stability of the FxLMS algorithm with the ActBrg approach is relatively easy to achieve, based on the experience of the FxLMS design for ActBrg in this study, and its high reduction effectiveness makes it highly recommendable to implement the FxLMS algorithm with the ActBrg approach to reduce vibration in the engine. The stability issue should be resolved by generating accurate secondary paths or by other measurements, e.g. using the IFF control as an emergency system.

8. Conclusion and outlook

Conclusion

This work was initiated by new actuator placement approaches inside the aircraft engine to actively reduce the vibration transmitted from the engine into the fuselage. A model generation procedure was developed to start the investigation of active systems applied on aircraft engine system. To study the effectiveness of these approaches, different positions on the vibration transmission path were identified (at the source, upstream inside the engine and downstream outside the engine close to the fuselage) and compared regarding the ideal optimal reduction level and the achievable reduction level. After employing different control algorithms with each of these approaches, suitable types of controllers were determined. Since the system can be seen as different active suspension systems with those actuation approaches, the simulation results were compared with the research on different suspension systems in past studies for verification. Based on the past experimental experience with different suspension systems, the feasibility of each approach and its corresponding control implementation were studied, leading to suggestions on their appropriate use.

Five state space models with different bearing configurations were generated based on the developed model generation method. This method was verified by comparing the results of modal, harmonic and transient analyses from Model 1 with those from the original FE model, according to adjusted MAC, FRAC and Pearson's correlation coefficient, respectively. By analyzing the frequency response to the synchronous excitation of unbalance of the HPR under different conditions in these models, it was found that the resonance around 250 Hz is important in the unbalance study and belongs to the HPR, It was further determined that the interaction between the LPR

and the HPR proves to be positive in the vibration reduction at some resonances when the system is excited by the latter's unbalance, and the bearing configurations influence the response of the HPR differently under various boundary conditions (fixed at the ends or connected to the WEM).

According to the three actuator placement approaches, three suspension systems were defined in the WEM. The average power was selected as the main evaluation criterion. Four stages were identified to represent the power transmission in the WEM: The input power by the unbalance of the HPR, the power through B3 & B4, the power through FUL, FLL & RMR and the power through the MNT.

The robustness of the passive systems in terms of the power transmitted into the fuselage shows the importance of the SFDs. Replacing them completely with the active methods is not recommended without implementing measures to ensure the functionality of the active system.

Minimization of the quadratic cost functions of several variables at different positions with the help of an optimal actuation force vector was used to learn the ideal effectiveness of reduction in the active systems.

Several variables were investigated as the optimization target for the three systems. Among these variables, acceleration can represent the vibration in the ActBrg and ActExSus systems well, while force and acceleration are both important to reduce the transmitted power in the ActInSus system. Because of the generally good performance of optimizing the squared acceleration in all cases without considering the rotational DOFs, this optimization strategy was selected for further investigation.

The non-negligible gyroscopic effect was stressed in the controlled systems: The actuation outside the engine does not interact with this effect (ActExSus), while it causes the relatively upstream part to the actuated part, when that is inside the engine (ActBrg and ActInSus), to absorb energy actively around the resonance of 240 Hz.

The damping effect of each actuation approach on the system was determined: ActBrg reduces the vibration at the beginning of the vibration path and does not change the role of the MNT and the engine as passive parts, while ActExSus and ActInSus affect the HPR and lead to the concentrated

excitation of the unbalance being distributed along the HPR. ActExSus reduces the vibration transmission mainly through restraining the rotation of the RMR and hardly modifies the power transmitted from the HPR. ActInSus proves its effectiveness at all positions, while ActBrg reduces the total power transmitted into the fuselage by making the front suspension absorb energy, due to its lesser effect on the rear links.

The study on the ideal effectiveness of all the systems with different bearing configurations and actuator placement approaches showed that ActBrg yields good results either with or without SFDs and that ActExSus with SFDs performs even better in the low frequency range (below 220 Hz), while ActInSus is relatively weak without sensor signals at the fuselage side. However, the performance of ActInSus can surpass ActExSus either by additional sensors at the junctions between the MNT and the fuselage or by additional force sensors at the FUL, FLL & RMR.

Based on the conclusions from the optimization results, different controllers were tested on the active systems. LQR, FxLMS and IFF were chosen because of their relatively easy design for large systems and their good reduction effectiveness. The performance of LQR is generally not good, although all the states are fed back. It can be improved by adjusting the weighting matrices. The best reduction is achieved with the FxLMS algorithm for three of the systems: ActBrg, ActExSus and ActInSus controlling the MNT. Moreover, the IFF control is suitable for the ActInSus system controlling the FUL, FLL & RMR. With their own suitable control algorithms, these four active systems, i.e. ActBrg controlling B3 & B4, ActInSus controlling the FUL, FLL & RMR, ActInSus and ActExSus controlling the MNT, can achieve a reduction of 17.35 dB, 7.22 dB, 4.89 dB and 3.03 dB, respectively, with regard to the highest resonance. ActBrg shows its absolute advantage, and ActInSus ranks the second with 10 dB less reduction. The two actuation approaches controlling the MNT are even weaker, although they target the evaluated positions, the JntFL. Considering the comfort during the cruise, ActBrg, ActInSus and ActExSus controlling the vibration at the fuselage side can reduce the vibration by 17.07 dB, 14.06 dB and 10.15 dB, respectively, based on the FxLMS algorithm. The numerical uncertainty study shows that

it can tolerate at least 20% phase error. The uncertainty study of secondary paths used in the FxLMS algorithm shows that it can endure at least 20% phase error with a compromise of 3 dB less reduction. Based on the process of the control design, it was found that the only gain of the IFF algorithm is easy to tune manually and can be applied for all the frequencies, thanks to its unconditional stability with collocation configurations, whereas the step size of the FxLMS algorithm needs to be adjusted differently for several frequency ranges, and the stability of a run-up test cannot be ensured due to the slow rate of convergence.

The conclusions based on simulations were compared with those from past studies, considering the active suspension systems and the control algorithms for large rotating machines. Some were verified, proving that those conclusions based on simple suspension systems are applicable to the complex system, e.g. optimizing the power through some of the DOFs has no advantage but causes power circulation, or determining which of the suspension systems identified in the aircraft engine system can be seen as a simple suspension system. The latter applies for instance in the ActExSus system, where the minimization of the squared linear acceleration indeed performs nearly as well as the minimization of the total power, even with the presence of rotational moments, but this does not hold true to the ActInSus system. There was disagreement between the present simulation and past conclusions in other cases, showing that those conclusions cannot be generalized, e.g. it was found only in the high frequency range of the ActBrg system that the control effort to minimize the power is less than that to minimize other variables, which was stated in past studies for simple suspension systems.

As the last part of this investigation, a feasibility study was carried out, considering the packaging and selection of actuators for ActBrg and ActInSus, the placement and selection of sensors and the implementation of controllers. With respect to the space and temperature, two types of piezoelectric actuators were selected for ActBrg and the front actuation of ActInSus, and an invention of piezoelectric extension actuators are applicable to the actuation of the rear links of ActInSus and the links of ActExSus. As for the sensor placement, placing accelerometers at the collocated positions with the actu-

ators is the main principle for each approach. Apart from that, additional accelerometers at the fuselage side are needed for ActInSus when the FxLMS algorithm is applied, and force sensors should be used when the IFF control is applied. The design of the IFF control is relatively easy, whereas the slow converging speed and instability of the FxLMS algorithm needs to be dealt with by using small step sizes, or by accurately estimating secondary paths or by using the IFF control as an emergency system. Based on the experience of control design and the results of reduction effectiveness in this investigation, it was recommended that ActBrg should be employed with FxLMS, together with the IFF control acting as an emergency system.

Outlook

Based on this investigation, the future work would be recommended to head in two directions: Further numerical investigation, which will be elaborated below, and experimental validation the necessity of which is self-evident.

The results of this work were generated mainly from the state space models. Based on these models, it was straightforward to learn about the motion of all DOFs and internal forces of some elements, such as the bearings of spring elements and the links of beam elements, with the help of their structural information, i.e. mass and stiffness. Subsequently, the power transmitted through certain elements could be further computed to describe the power flow in respective parts of the system. Furthermore, the active control can be integrated in the state space model. However, some information required for a decision on the implementation is not available, for example, in order to select the proper material, it is essential to be aware of how the stress is distributed when a specific actuator placement approach with a certain control algorithm is applied on the system. To extract more information from the actively controlled system, ANSYS as a FE analysis software is advisable. Moreover, the visualization module of the FE analysis software makes the presentation of the information easy and straightforward. The possibility of integrating the active control in a model in ANSYS was proved by past studies to reduce the vibration of a cantilever beam, and the results were validated experimentally [65]. However, it was predicted that a long

processing time would be needed for a large and complex model, since a full transient analysis should be carried out when integrating controllers. Therefore, whether it is worth such a long computational time to acquire more detailed information from the actively controlled WEM depends on the cost of immediately constructing a test rig and assessing all considered aspects through experiments. As part of future work, the cost of tests and the aspects to be verified should be learned. If said cost is high or too many aspects are of interest, it would be recommended to take the time to test them in ANSYS in advance, rather than waste time and money on the experimental tests.

In addition, optimizing the combination of the squared force and squared velocity was discussed in many sections here and in past studies, revealing some of its advantages for this engine system while others may yet lie hidden due to the non-optimal scaling factor. This prospect is worth further investigation, because of the already discovered benefits, e.g. that this strategy does not require any additional accelerometers on the fuselage side for the ActInSus approach to achieve a good reduction level and that the complex wire connection or observer design can be avoided. Furthermore, the control effort of this strategy is less than that needed to minimize the acceleration, and this strategy works as effectively as optimizing the power at the max. take-off frequency in the ActBrg system, whereas the other strategies have no effect at all at this frequency.

With regard to the control application, the stability of the FxLMS algorithm should be improved. In [69], an adaptive algorithm, using simultaneous equations method without the model of secondary paths, was developed, and its advantages in converging speed and stability were validated experimentally. This method could be employed on the engine as an alternative to FxLMS.

Bibliography

[1] K. Aainsqatsi. Turbofan operation. https://commons.wikimedia.org/wiki/File:Turbofan_operation_lbp.svg#filelinks. Licensed under GNU.

[2] L. S. Andrés. Notes 13. Squeeze film dampers: Operation, models and technical issues. http://rotorlab.tamu.edu/me626/Notes_pdf/Notes13%20Squeeze%20Film%20Dampers.pdf, 2010. Accessed: 2015-01-12.

[3] J. Antonio. *Power flow in structures during steady-state forced vibration.* PhD thesis, University of London, 1984.

[4] M. Bebesel and P. Jänker. Piezoelectric extension actuator, December 8 2004. EP Patent 1,322,873.

[5] H. Bedrossian and N. Veikos. Rotor-disk system gyroscopic effect in MSC/Nastran dynamic solution. In *MSC World Users' Conference*, 1982.

[6] G. Billoud. Active control at Lord Corporation - A reality. Technical report, Lord Corporation, 2001.

[7] M. Borsdorf. *Aktive Schwingungsminderung elastischer Flugtriebsrotoren mit Piezostapelaktoren unter Berücksichtigung der Dynamik des Triebwerkgehäuses.* PhD thesis, Technische Universität Darmstadt, 2014.

[8] John Burkardt. Matlab function: hb_to_msm. http://people.sc.fsu.edu/~jburkardt/m_src/hb_to_msm/hb_to_msm.html, Jan 2014. It reads a sparse matrix in the Harwell Boeing Sparse Matrix File Format and returns it as a MatLab sparse matrix.

[9] C. Chang-Jian, H. Yau, and J. Chen. Nonlinear dynamic analysis of a hybrid squeeze-film damper-mounted rigid rotor lubricated with couple stress fluid and active control. *Applied Mathematical Modelling*, 34(9):2493 – 2507, 2010.

[10] B. Cottrell, G. J. Zalewski, and J. Kroeger. Gas turbine engine rotor tip clearance and shaft dynamics system and method, April 22 2014. US Patent 8,702,377.

[11] R. R. Craig. A review of time domain and frequency domain component mode synthesis methods. *International Journal of Analytical and Experimental Modal Analysis*, 2(2):59–72, 1987.

[12] NSW Environment Protection Authority (EPA). Assessing vibration: A technical guideline, 2006.

[13] K. Federn. *Auswuchttechnik: Band 1: Allgemeine Grundlagen, Meßverfahren und Richtlinien.* Springer-Verlag Berlin Heidelberg, 1977.

[14] D. P. Fleming. Dual clearance squeeze film damper for high load conditions. In *Joint lubrication conference*, 1984.

[15] E. Frankenberger and P. Konstanzer. Structural element for an aircraft, July 9 2008. EP Patent 1,681,236.

[16] C. R. Fuller. Apparatus and method for global noise reduction, December 29 1987. US Patent 4,715,559.

[17] P. Gardonio, S. J. Elliott, and R. J. Pinnington. Active isolation of structural vibration on a multiple-degree-of-freedom system, part I: The dynamics of the system. *Journal of Sound and Vibration*, 207(1):61 – 93, 1997.

[18] P. Gardonio, S. J. Elliott, and R. J. Pinnington. Active isolation of structural vibration on a multiple-degree-of-freedom system, part II: Effectiveness of active control strategies. *Journal of Sound and Vibration*, 207(1):95 – 121, 1997.

[19] PI Ceramic GmbH. Catalog: PI Piezoelectric actuators, 2012.

[20] J. H. Gorndt, W. E. Schmidt, and P. R. Woodford. Engine mounting system, November 29 1966. US Patent 3,288,404.

[21] H. G. D. Goyder and R. G. White. Vibration power flow from machines into built-up structures, part I: Introduction and approximate analyses of beam and plate-like foundations. *Journal of Sound and Vibration*, 68(1):59–75, 1980.

[22] H. G. D. Goyder and R. G. White. Vibration power flow from machines into built-up structures, part II: Wave propagation and power flow in beam-stiffened plates. *Journal of Sound and Vibration*, 68(1):77–96, 1980.

[23] H. G. D. Goyder and R. G. White. Vibration power flow from machines into built-up structures, part III: Power flow through isolation system. *Journal of Sound and Vibration*, 68(1):97–117, 1980.

[24] M. Grasselli and D. Pelinovsky. *Numerical mathematics*. Jones and Bartlett, 2008.

[25] G. W. D. M. Gunawardene and E. Forrest. Controllability of linear control systems using gilbert and kalman criteria. *International Journal of Mathematical Education in Science and Technology*, 27(5):675–683, 1996.

[26] V. Gupta, M. Sharma, and N. Thakur. Optimization criteria for optimal placement of piezoelectric sensors and actuators on a smart structure: A technical review. *Journal of Intelligent Material Systems and Structures*, 21(12):1227–1243, 2010.

[27] Aurélien Hazan, Michel Verleysen, Marie Cottrell, and Jérôme Lacaille. Trajectory clustering for vibration detection in aircraft engines. In Petra Perner, editor, *Industrial Conference on Data mining 2010*, pages 362–375, Berlin, Germany, July 2010. Springer.

[28] R. Helfrich. Active damping of composites. In *NAFEMS World Congress*, 2009.

[29] D. A. Hodgson and T. G. Duclos. Mount with adjustable length inertia track, November 13 1990. US Patent 4,969,632.

[30] F. Hoffmann, R. Maier, P. Jänker, and F. Hermle. Helicopter interior noise reduction by using active gearbox struts. In *12th AIAA/CEAS Aeroacoustics Conference (27th AIAA Aeroacoustics Conference)*, 2006.

[31] C. Q. Howard and C. H. Hansen. Finite element analysis of active vibration isolation using vibrational power as a cost function. *International Journal of Acoustics and Vibration*, 4(1):23–36, 1999.

[32] C. Q. Howard and C. H. Hansen. Active vibration isolation experiments using translational and rotational power transmission as a cost function. *Journal of the Acoustical Society of America*, 120(4):2004–2016, 2006.

[33] C. Q. Howard, C. H. Hansen, and J. Pan. Power transmission from a vibrating body to a circular cylindrical shell through passive and active isolators. *Journal of the Acoustical Society of America*, 101(3):1479–1491, 1997.

[34] C. Q. Howard, S. D. Snyder, and C. H. Hansen. Calculation of vibratory power transmission for use in active vibration control. *Journal of Sound and Vibration*, 233(4):569–581, 2000.

[35] Mechanical vibration and shock - Evaluation of human exposure to whole-body vibration Part 1: General requirements, 1997.

[36] P. Jänker, F. Claeyssen, B. Grohmann, M. Christmann, T. Lorkowski, R. Leletty, O. Sosniki, and A. Pages. New actuators for aircraft and space applications. In *11th international conference on new actuators*, 2008.

[37] R. A. John, E. J. Straneva, and P. R. Woodford. Mounting system, December 10 1968. US Patent 3,415,470.

[38] Y. K. Koh and R. G. White. Analysis and control of vibrational power transmission to machinery supporting structures subjected to a multi-excitation system, part II: Vibrational power analysis and control schemes. *Journal of Sound and Vibration*, 196(4):495 – 508, 1996.

[39] P. Koutsovasilis and M. Beitelschmidt. Model reduction of large elastic systems: A comparison study on the elastic piston rod. In *II World Congress in Mechanism and Machine Science, IFToMM*, 2007.

[40] P. Koutsovasilis and M. Beitelschmidt. Comparison of model reduction techniques for large mechanical systems. *Journal of Multibody System Dynamics*, 20(2):111–128, 2008.

[41] F. Kubica and B. Madelaine. Passenge comfort improvement by integrated control law design. In *Structural Aspects of Flexible Aircraft Control*. Aerospatiale Matra Airbus, 1999.

[42] F. Lebo and S. Rinderknecht. Umsetzungsanalyse piezoaktorischer Reduktion von Rotorschwingungen in realen Flugtriebwerken. Internal report from Institute for mechatronic systems in mechanical engineering, TU Darmstadt, Germany, 2011.

[43] G. Locatelli, H. Langer, M. Müller, and H. Baier. Simultaneous optimization of actuator placement and structural parameters by mathematical and genetic optimization algorithms. In U. Gabbert and H.S. Tzou, editors, *IUTAM Symposium on Smart Structures and Structronic Systems*, volume 89 of *Solid Mechanics and Its Applications*, pages 255–263. Springer Netherlands, 2001.

[44] J. Lunze. *Regelungstechnik 2: Mehrgrößensysteme Digitale Regelung*. Springer, 2013.

[45] N. J. Mansfield, P. Holmlund, and R. Lundström. Comparison of subjective responses to vibration and shock with standard analysis methods and absorbed power. *Journal of Sound and Vibration*, 230(3):477 – 491, 2000.

[46] J. Marra, P. J. P. Gonçalves, and L. C. S. Góes. A multichannel active-adaptive vibration control system applied to an aeronautical structure. In *ISMA2010-USD2010 Conference*, 2010.

[47] H. Nguyen-Schäfer. *Rotordynamics of automotive turbochargers: Linear and nonlinear rotordynamics-bearing design-rotor balancing.* Springer, 2012.

[48] American Bureau of Shipping. Guide for passenger comfort on ships, 2014.

[49] H. Porumamulla. *Modeling, analysis and non-linear control of a novel pneumatic semi-active vibration isolator: A concept validation study.* PhD thesis, Iowa State University, 2007.

[50] F. Pradko and R. A. Lee. Vibration comfort criteria. In *Automotive Engineering Congress.* Society of Automotive Engineers. Inc., Jan. 1966.

[51] A. Preumont. *Vibration control of active structures.* Springer, 2011.

[52] Zu-Qing Qu. *Model order reduction techniques with applications in finite element analysis.* Springer, 2004.

[53] J. Quehl. *Comfort studies on aircraft interior sound and vibration.* PhD thesis, Universität Oldenburg, 2001.

[54] J. Rodriguez, L. Gaudiller, S. Chesne, and P. Cranga. Control of a helicopter main gearbox active suspension system. In *ASME 2014 International Design Engineering Technical Conferences and Computers and Information in Engineering Conference*, 2014.

[55] Rolls-Royce. *The jet engine.* Rolls Royce Technical Publications, 1996.

[56] Rolls-Royce. *The jet engine.* Rolls Royce Technical Publications, 2005.

[57] D. J. Rossetti, D. E. Ivers, M. A. Norris, M. C. Heath, and S. C. Southward. Active structural control system and method including active vibration absorbers (AVAs), December 14 1999. US Patent 6,002,778.

[58] D. J. Rossetti, M. A. Norris, and G. D. Billoud. Active vibration control system for helicopter with improved actuator placement, October 22 2002. US Patent 6,467,723.

[59] R. S. Schittenhelm. *Regelungstechnische Verfahren zur aktiven Minderung von Rotorschwingungen.* PhD thesis, Technische Universität Darmstadt, 2014.

[60] K.M. Sen and D.R. Morgan. *Active noise control systems: Algorithms and DSP implementations.* John Wiley & Sons, Inc., 1996.

[61] Sensor Technology Ltd. Active noise and vibration control. Technical report, Smart Structures, 1998.

[62] S. C. Southward and D. E. Ivers. Active mounts for aircraft engines, May 1 2001. CA Patent 2,193,080.

[63] W. Sun, Z. Gao, D. Tang, and X. Zhu. Design and experiment of adaptive active vibration control system for aircraft framework. In *System Simulation and Scientific Computing*, pages 197–204. Springer Berlin Heidelberg, 2012.

[64] E. Swanson, C.D. Powell, and S. Weissman. A practical review of rotating machinery critical speeds and modes. *Journal of Sound and Vibration*, 39(5):10–17, 2005.

[65] G. Takács and B. Rohal-ilkiv. Direct closed-loop active vibration control system prototyping in ANSYS. In *Noise and Vibration: Emerging Methods*, 2012.

[66] A. H. von Flotow. An expository overview of active control of machinery mounts. In *27th Conference on Decision and Control*, 1988.

[67] J. L. White, S. A. Shipley, and T. F. Yantis. Active control studies of structurally transmitted engine vibration on commercial airplanes. In *IMAC XII - 12th International Modal Analysis Conference*, 1994.

[68] G. P. Whiteford and P. T. Herbst. Vibration isolation system including a passive tuned vibration absorber, November 18 1997. US Patent 5,687,948.

[69] P. Zech, F. Becker, and S. Rinderknecht. Der Simultaneous-Equations-Algorithms zur aktiven Schwingungsisolation bei schmalbandigen Störungen. In *Schwingungen in Antrieben*, 2015.

Appendices

A. Cost functions and optimization

Assuming that the responses in terms of acceleration and force with respect to frequency in complex plane are

$$A_{rsp}(j\omega) = Z_{ap}(j\omega) F_p(j\omega) + Z_{ac}(j\omega) F_c(j\omega) \tag{A.1}$$

$$F_{rsp}(j\omega) = Z_{fp}(j\omega) F_p(j\omega) + Z_{fc}(j\omega) F_c(j\omega) \tag{A.2}$$

where F_p and F_c are the primary force (or the disturbance) and control force, respectively, and Z_{ij} is the transfer function between acceleration or force, i, and disturbance or control force, j.

The quadratic cost function in terms of acceleration is

$$A_{sq}(\omega) = A_{rsp}^* A_{rsp} = Re\left(A_{rsp}^* A_{rsp}\right) \tag{A.3}$$

And it can be expanded based on Eq. (A.1) and Eq. (A.2):

$$A_{sq}(\omega) = Re\left(F_c^* Z_{ac}^* Z_{ac} F_c + F_c^* Z_{ac}^* Z_{ap} F_p + F_p^* Z_{ap}^* Z_{ac} F_c + F_p^* Z_{ap}^* Z_{ap} F_p\right) \tag{A.4}$$

where $Re(\ )$ denotes extracting the real part of the complex expression.

With the help of

$$a_a(j\omega) = Z_{ac}^* Z_{ac} \tag{A.5}$$

$$b_{a1}(j\omega) = Z_{ac}^* Z_{ap} F_p \tag{A.6}$$

$$b_{a2}(j\omega) = F_p^* Z_{ap}^* Z_{ac} \tag{A.7}$$

$$c_a(j\omega) = F_p^* Z_{ap}^* Z_{ap} F_p \tag{A.8}$$

the calculation can be changed to real plane from complex plane, i.e. the

squared acceleration can be rearranged and expressed in real matrices:

$$\begin{aligned} A_{sq}(\omega) = &\begin{bmatrix} F_c^r & F_c^i \end{bmatrix} \begin{bmatrix} a_a^r & -a_a^i \\ a_a^i & a_a^r \end{bmatrix} \begin{bmatrix} F_c^r \\ F_c^i \end{bmatrix} \\ &+ \begin{bmatrix} F_c^r & F_c^i \end{bmatrix} \begin{bmatrix} b_{a1}^r \\ b_{a1}^i \end{bmatrix} + \begin{bmatrix} b_{a2}^r & -b_{a2}^i \end{bmatrix} \begin{bmatrix} F_c^r \\ F_c^i \end{bmatrix} + c_a^r \end{aligned} \tag{A.9}$$

where X^r and X^i denote the real and imaginary parts of a complex number X.

Assuming that

$$q_c(\omega) = \begin{bmatrix} F_c^r & F_c^i \end{bmatrix}^T \tag{A.10}$$

$$\alpha_a(\omega) = \begin{bmatrix} a_a^r & -a_a^i \\ a_a^i & a_a^r \end{bmatrix} \tag{A.11}$$

$$\beta_a(\omega) = \frac{1}{2}\left(\begin{bmatrix} b_{a1}^r \\ b_{a1}^i \end{bmatrix} + \begin{bmatrix} b_{a2}^r & -b_{a2}^i \end{bmatrix}^T \right) \tag{A.12}$$

then the expression of squared acceleration can be further simplified:

$$A_{sq}(\omega) = q_c^T \alpha_a q_c + q_c^T \beta_a + \beta_a^T q_c + c_a^r \tag{A.13}$$

Similarly, the quadratic cost function of force can be expressed as:

$$F_{sq}(\omega) = F_{rsp}^* F_{rsp} = q_c^T \alpha_f q_c + q_c^T \beta_f + \beta_f^T q_c + c_f^r \tag{A.14}$$

based on the complex expressions

$$a_f(j\omega) = Z_{fc}^* Z_{fc} \tag{A.15}$$

$$b_{f1}(j\omega) = Z_{fc}^* Z_{fp} F_p \tag{A.16}$$

$$b_{f2}(j\omega) = F_p^* Z_{fp}^* Z_{fc} \tag{A.17}$$

$$c_f(j\omega) = F_p^* Z_{fp}^* Z_{fp} F_p \tag{A.18}$$

and the real expressions

$$\alpha_f(\omega) = \begin{bmatrix} a_f^r & -a_f^i \\ a_f^i & a_f^r \end{bmatrix} \tag{A.19}$$

$$\beta_f(\omega) = \frac{1}{2}\left(\begin{bmatrix} b_{f1}^r \\ b_{f1}^i \end{bmatrix} + \begin{bmatrix} b_{f2}^r & -b_{f2}^i \end{bmatrix}^T \right) \tag{A.20}$$

Different from the squared acceleration and squared force, which take the real part of the product of two complex values, the time average value of the power at each frequency in steady state should be expressed as the function of the imaginary part of the product of complex force and complex acceleration.

$$\begin{aligned} P_{av}(\omega) &= \frac{1}{2} Re\left(F_{rsp}^{*} V_{rsp}\right) \\ &= -\frac{1}{2\omega} Im\left(F_{rsp}^{*} A_{rsp}\right) \\ &= -\frac{1}{2\omega}\left(q_c^T \alpha_{pw} q_c + q_c^T \beta_{pw} + \beta_{pw}^T q_c + c_{pw}^i\right) \end{aligned} \tag{A.21}$$

based on the complex expressions

$$a_{pw}(j\omega) = Z_{fc}^{*} Z_{ac} \tag{A.22}$$

$$b_{pw1}(j\omega) = Z_{fc}^{*} Z_{ap} F_p \tag{A.23}$$

$$b_{pw2}(j\omega) = F_p^{*} Z_{fp}^{*} Z_{ac} \tag{A.24}$$

$$c_{pw}(j\omega) = F_p^{*} Z_{fp}^{*} Z_{ap} F_p \tag{A.25}$$

and the real expressions

$$\alpha_{pw}(\omega) = \begin{bmatrix} a_{pw}^i & a_{pw}^r \\ -a_{pw}^r & a_{pw}^i \end{bmatrix} \tag{A.26}$$

$$\beta_{pw}(\omega) = \frac{1}{2}\left(\begin{bmatrix} b_{pw1}^i \\ -b_{pw1}^r \end{bmatrix} + \begin{bmatrix} b_{pw2}^i & b_{pw2}^r \end{bmatrix}^T\right) \tag{A.27}$$

The cost equations J can be minimized when

$$(q_c)_{opt} = -\alpha^{-1}\beta \tag{A.28}$$

where α corresponds to α_a, α_f or α_{pw}, and β corresponds to β_a, β_f or β_{pw}, respectively aiming at the minimal of squared acceleration, sqared force or power expressed as:

$$min(A_{sq}) = -\beta_a^T \alpha_a^{-1} \beta_a + c_a^r \tag{A.29}$$

$$min(F_{sq}) = -\beta_f^T \alpha_f^{-1} \beta_f + c_f^r \tag{A.30}$$

$$min(P_{av}) = \frac{1}{2\omega}\left(-\beta_{pw}^T \alpha_{pw}^{-1} \beta_{pw} + c_{pw}^i\right) \tag{A.31}$$

B. FE Model transfer from Nastran to ANSYS

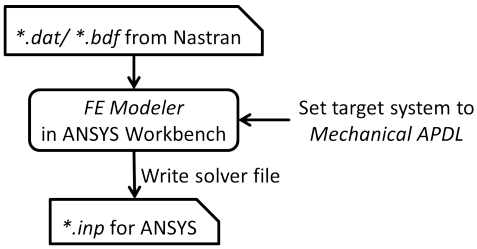

(a) Common input file from Nastran

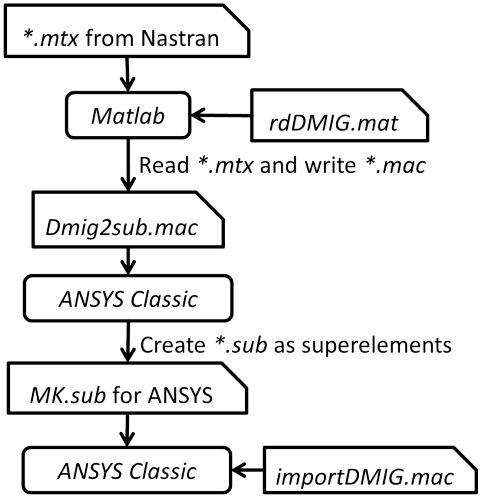

(b) Matrix file from Nastran

Figure B.1.: Files from Nastran transferred into ANSYS

Example of rdDMIG.mat

```
%%%%%%%% %%%%%%% %%%%%%% %%%%%%% %%%%%%%% %%%%%%% %%%%%%%
% This is for the HPR
% For LPR, replace all 'HPR' in this file with 'LPR'
%%%%%%%% %%%%%%% %%%%%%% %%%%%%% %%%%%%%% %%%%%%% %%%%%%%
startRow_K=63;
nRows_endOfK=1488;
nRows_endOfM=2897;
noOfdof_sglNd_HPR=6;
rdfile='HPR.mtx';
createFile='dmig2sub_HPR.mac';
%
fid = fopen(rdfile);
for nn=1:startRow_K
   textline = fgetl(fid);
end
% read K
textline = fgetl(fid);
txt = sscanf(textline,'%*s %*s %d %d %d %d %d');
noOfdof_K_HPR=txt(5);
cnt_row_K=0;
for j=startRow_K+2:nRows_endOfK
   textline = fgetl(fid);
   txt = sscanf(textline,'%*s %d %d %f');
   if isempty(txt)==1
      cnt_row_K=cnt_row_K+1;
      txt = sscanf(textline,'%*s %*s %d %d');
      node_K(cnt_row_K)=txt(1);
      dof_row_K(cnt_row_K)=txt(2);
      continue
   end
   node_col_K=txt(1);
   dof_col_K=txt(2);
   if node_col_K==35365
      cnt_col_K=dof_col_K;
   else
      cnt_col_K=((node_col_K-35366)/2)*6+dof_col_K;
   end
   KAAHP0(cnt_row_K,cnt_col_K)=txt(3);
end
Ksize_HPR=size(KAAHP0,1);
%
```

```
% read M
textline = fgetl(fid);
txt = sscanf(textline,'%*s %*s %d %d %d %d %d');
noOfdof_M_HPR=txt(5);
cnt_row_M=0;
for j=nRows_endOfK+2:nRows_endOfM
   textline = fgetl(fid);
   txt = sscanf(textline,'%*s %d %d %f');
   if isempty(txt)==1
      cnt_row_M=cnt_row_M+1;
      txt = sscanf(textline,'%*s %*s %d %d');
      node_M(cnt_row_M)=txt(1);
      dof_row_M(cnt_row_M)=txt(2);
      continue
   end
   node_col_M=txt(1);
   dof_col_M=txt(2);
   if node_col_M==35365
      cnt_col_M=dof_col_M;
   else
      cnt_col_M=((node_col_M-35366)/2)*6+dof_col_M;
   end
   MAAHP0(cnt_row_M,cnt_col_M)=txt(3);
end
Msize_HPR=size(MAAHP0,1);
fclose(fid);
%complete M K
KAAHP=KAAHP0;
MAAHP=MAAHP0;
for i=1:Msize_HPR
   for j=i:Msize_HPR
      KAAHP(i,j)=KAAHP0(j,i);
      MAAHP(i,j)=MAAHP0(j,i);
   end
end
%
%%%%%%%% %%%%%%% %%%%%%% %%%%%%%
%write dmig2sub.mac
%%%%%%%% %%%%%%% %%%%%%% %%%%%%%
fout=fopen(createFile,'wt');
% print node coordinates
fprintf(fout,'%s','/prep7');
```

```
% print K
fprintf(fout,'\n%s,%d,%d','*DMAT,K_HPR,d,alloc',Ksize_HPR,Ksize_HPR);
for i=1:Ksize_HPR
   for j=1:Ksize_HPR
      fprintf(fout,'\n%s%d%s%d%s%.9e','K_HPR(',i,',',j,')=',KAAHP(i,j
          ));
   end
end
% print M
fprintf(fout,'\n%s,%d,%d','*DMAT,M_HPR,d,alloc',Msize_HPR,Msize_HPR);
for i=1:Msize_HPR
   for j=1:Msize_HPR
      fprintf(fout,'\n%s%d,%d%s%.9e','M_HPR(',i,j,')=',MAAHP(i,j));
   end
end
% print rowinfo
fprintf(fout,'\n%s,%d,%d','*DMAT,rowinfo_hpr,i,alloc',Msize_HPR,2);
for j=1:floor(Msize_HPR/18)+1
   fprintf(fout,'\n%s%d,%d%s%d','rowinfo_hpr(',(j-1)*18+1,1,')=',
       node_M((j-1)*18+1));
   if j==floor(Msize_HPR/18)+1
      for i=2:mod(Msize_HPR,18)
         fprintf(fout,',%d',node_M((j-1)*18+i));
      end
      break
   end
   if j<floor(Msize_HPR/18)+1
      for i=2:18
         fprintf(fout,',%d',node_M((j-1)*18+i));
      end
   end
end
for j=1:floor(Msize_HPR/18)+1
   fprintf(fout,'\n%s%d,%d%s%d','rowinfo_hpr(',(j-1)*18+1,2,')=',
       dof_row_M((j-1)*18+1));
   if j==floor(Msize_HPR/18)+1
      for i=2:mod(Msize_HPR,18)
         fprintf(fout,',%d',dof_row_M((j-1)*18+i));
      end
      break
   end
   if j<floor(noOfdof_K_HPR/18)+1
```

```
      for i=2:18
         fprintf(fout,',%d',dof_row_M((j-1)*18+i));
      end
   end
end
fprintf(fout,'\n%s','*PRINT,rowinfo_hpr');
fprintf(fout,'\n%s','*EXPORT,K_HPR,sub,MKHPR.sub,stiff,rowinfo_hpr,
    wait');
fprintf(fout,'\n%s','*EXPORT,M_HPR,sub,MKHPR.sub,mass,rowinfo_hpr,done
    ');
fprintf(fout,'\n%s','SELIST,MKHPR,3');
fclose(fout);
```

Example of Dmig2sub.mac

```
/prep7
*DMAT,K_HPR,d,alloc,96,96
K_HPR(1,1)=8.533332655e+05
K_HPR(1,2)=0.000000000e+00
K_HPR(1,3)=0.000000000e+00
K_HPR(1,4)=0.000000000e+00
K_HPR(1,5)=0.000000000e+00
K_HPR(1,6)=0.000000000e+00
K_HPR(1,7)=-7.547295621e+05
K_HPR(1,8)=0.000000000e+00
K_HPR(1,9)=0.000000000e+00
K_HPR(1,10)=0.000000000e+00
.
.
.
K_HPR(2,1)=0.000000000e+00
K_HPR(2,2)=5.615777400e+05
K_HPR(2,3)=0.000000000e+00
.
.
.
K_HPR(96,96)=2.285032918e+09
*DMAT,M_HPR,d,alloc,96,96
M_HPR(1,1)=6.685584284e-03
M_HPR(1,2)=0.000000000e+00
.
.
.
```

```
M_HPR(96,96)=3.936195265e+00
*DMAT,rowinfo_hpr,i,alloc,96,2
rowinfo_hpr(1,1)=35365,35365,35365,...
rowinfo_hpr(19,1)=35372,35372,35372,...
rowinfo_hpr(37,1)=35378,35378,35378,...
rowinfo_hpr(55,1)=35384,35384,35384,...
rowinfo_hpr(73,1)=35390,35390,35390,...
rowinfo_hpr(91,1)=35396,35396,35396,...
rowinfo_hpr(1,2)=1,2,3,4,5,6,1,2,3,4,5,6,1,2,3,4,5,6
rowinfo_hpr(19,2)=1,2,3,4,5,6,1,2,3,4,5,6,1,2,3,4,5,6
rowinfo_hpr(37,2)=1,2,3,4,5,6,1,2,3,4,5,6,1,2,3,4,5,6
rowinfo_hpr(55,2)=1,2,3,4,5,6,1,2,3,4,5,6,1,2,3,4,5,6
rowinfo_hpr(73,2)=1,2,3,4,5,6,1,2,3,4,5,6,1,2,3,4,5,6
rowinfo_hpr(91,2)=1,2,3,4,5,6
*PRINT,rowinfo_hpr
*EXPORT,K_HPR,sub,MKHPR.sub,stiff,rowinfo_hpr,wait
*EXPORT,M_HPR,sub,MKHPR.sub,mass,rowinfo_hpr,done
SELIST,MKHPR,3
```

Example of importDMIG.mac

```
/prep7
et,111,matrix50
type,111
se,mkhpr
se,mklpr
```

C. Calculation of stiffness and mass matrices of extended models

As shown in Fig. 3.6, the stiffness and damping matrices of the bearing structure are listed below for each configuration. The values of the stiffness and damping used in this investigation can be found in Section 3.3.2.

Model 1: with rigid connections

Combining the stiffness matrices of the element on the casing, of the bearing and of the element on the HPR, i.e.

$$\begin{bmatrix} k_1 & -k_1 \\ -k_1 & k_1 \end{bmatrix}, \begin{bmatrix} k_r & -k_r \\ -k_r & k_r \end{bmatrix} \textit{ and } \begin{bmatrix} k_2 & -k_2 \\ -k_2 & k_2 \end{bmatrix}, \tag{C.1}$$

the stiffness matrix of this whole structure is

$$\begin{bmatrix} k_1 & -k_1 & 0 & 0 \\ -k_1 & k_1 + k_r & -k_r & 0 \\ 0 & -k_r & k_r + k_2 & -k_2 \\ 0 & 0 & -k_2 & k_2 \end{bmatrix}. \tag{C.2}$$

The damping in this case is zero.

Model 2: with actuators applied

When the actuator with stiffness k_{act} is introduced in series with the rigid bearing, Model 2 is generated. m_0 has a small mass value. The stiffness of the bearing structure is:

$$\begin{bmatrix} k_1 & -k_1 & 0 & 0 & 0 \\ -k_1 & k_1 + k_{act} & -k_{act} & 0 & 0 \\ 0 & -k_{act} & k_{act} + k_r & -k_r & 0 \\ 0 & 0 & -k_r & k_r + k_2 & -k_2 \\ 0 & 0 & 0 & -k_2 & k_2 \end{bmatrix} \tag{C.3}$$

The damping in this case is also zero.

Model 3: with SFDs applied

When the rigid connection is replaced with the SFD, including the SC (k_{sc}) and the oil film (d_{sfd}), Model 3 is generated. The stiffness of the bearing structure is:

$$\begin{bmatrix} k_1 & -k_1 & 0 & 0 & 0 \\ -k_1 & k_1 + k_{sc} & -k_{sc} & 0 & 0 \\ 0 & -k_{sc} & k_{sc} + k_r & -k_r & 0 \\ 0 & 0 & -k_r & k_r + k_2 & -k_2 \\ 0 & 0 & 0 & -k_2 & k_2 \end{bmatrix} \tag{C.4}$$

The damping of the bearing structure is:

$$\begin{bmatrix} 0 & 0 & 0 & 0 & 0 \\ 0 & d_{sfd} & -d_{sfd} & 0 & 0 \\ 0 & -d_{sfd} & d_{sfd} & 0 & 0 \\ 0 & 0 & 0 & 0 & 0 \\ 0 & 0 & 0 & 0 & 0 \end{bmatrix} \tag{C.5}$$

Model 4: SFDs and actuators applied in series

When the actuator is introduced to Model 3 and connected in series with the SFD, Model 4 is generated. The stiffness of the bearing structure is:

$$\begin{bmatrix} k_1 & -k_1 & 0 & 0 & 0 & 0 \\ -k_1 & k_1 + k_{act} & -k_{act} & 0 & 0 & 0 \\ 0 & -k_{act} & k_{act} + k_{sc} & -k_{sc} & 0 & 0 \\ 0 & 0 & -k_{sc} & k_{sc} + k_r & -k_r & 0 \\ 0 & 0 & 0 & -k_r & k_r & -k_2 \\ 0 & 0 & 0 & 0 & -k_2 & k_2 \end{bmatrix} \tag{C.6}$$

The damping of the bearing structure is:

$$\begin{bmatrix} 0 & 0 & 0 & 0 & 0 & 0 \\ 0 & 0 & 0 & 0 & 0 & 0 \\ 0 & 0 & d_{sfd} & -d_{sfd} & 0 & 0 \\ 0 & 0 & -d_{sfd} & d_{sfd} & 0 & 0 \\ 0 & 0 & 0 & 0 & 0 & 0 \\ 0 & 0 & 0 & 0 & 0 & 0 \end{bmatrix} \tag{C.7}$$

Model 5: with SFDs and actuators applied in parallel

When the actuator is introduced to Model 3 and connected in parallel with the SFD, Model 5 is generated. The stiffness of the bearing structure is:

$$\begin{bmatrix} k_1 & -k_1 & 0 & 0 & 0 \\ -k_1 & k_1 + \left(\frac{k_{sc}k_{act}}{k_{sc}+k_{act}}\right) & -\left(\frac{k_{sc}k_{act}}{k_{sc}+k_{act}}\right) & 0 & 0 \\ 0 & -\left(\frac{k_{sc}k_{act}}{k_{sc}+k_{act}}\right) & \left(\frac{k_{sc}k_{act}}{k_{sc}+k_{act}}\right) + k_r & -k_r & 0 \\ 0 & 0 & -k_r & k_r + k_2 & -k_2 \\ 0 & 0 & 0 & -k_2 & k_2 \end{bmatrix} \tag{C.8}$$

The damping of the bearing structure is:

$$\begin{bmatrix} 0 & 0 & 0 & 0 & 0 \\ 0 & d_{sfd} & -d_{sfd} & 0 & 0 \\ 0 & -d_{sfd} & d_{sfd} & 0 & 0 \\ 0 & 0 & 0 & 0 & 0 \\ 0 & 0 & 0 & 0 & 0 \end{bmatrix} \tag{C.9}$$

D. Model validation results

D.1. Validation based on FRAC values

Input	Position	Input number
Unbalance	at 6^{th} stage of HPR	0
Actuation	at B3 in y	1
Actuation	at the strut under FUL	2
Actuation	at lower link of the A-frame	3
Actuation	at a front link of MNT (Link 2)	4
Actuation	at a rear link of MNT (Link 6)	5

Table D.1.: Inputs to be used in FRAC calculation

Output	Coordinate	Output number
at 6^{th} stage of HPR	A_x, A_y, A_z	1 to 3
B1	A_x, A_y, A_z	4 to 6
B2	A_y, A_z	7 to 8
B3	A_x, A_y, A_z	9 to 11
B4	A_y, A_z	12 to 13
B5	A_y, A_z	14 to 15
FUL	A_x, A_y, A_z, $A_{\theta x}$, $A_{\theta y}$, $A_{\theta z}$	16 to 21
FLL	A_x, A_y, A_z, $A_{\theta x}$, $A_{\theta y}$, $A_{\theta z}$	22 to 27
RMR	A_x, A_y, A_z, $A_{\theta x}$, $A_{\theta y}$, $A_{\theta z}$	28 to 33
Link 1 of MNT	A_x, A_y, A_z, $A_{\theta x}$, $A_{\theta y}$, $A_{\theta z}$	34 to 39
Link 2 of MNT	A_x, A_y, A_z, $A_{\theta x}$, $A_{\theta y}$, $A_{\theta z}$	40 to 45
Link 3 of MNT (alignment rod)	A_x, A_y, A_z, $A_{\theta x}$, $A_{\theta y}$, $A_{\theta z}$	46 to 51
Link 4 of MNT (thrust rod)	A_x, A_y, A_z, $A_{\theta x}$, $A_{\theta y}$, $A_{\theta z}$	52 to 57
Link 5 of MNT	A_x, A_y, A_z, $A_{\theta x}$, $A_{\theta y}$, $A_{\theta z}$	58 to 63
Link 6 of MNT	A_x, A_y, A_z, $A_{\theta x}$, $A_{\theta y}$, $A_{\theta z}$	64 to 69

B1	F_x, F_y, F_z	70 to 72
B2	F_y, F_z	73 to 74
B3	F_x, F_y, F_z	75 to 77
B4	F_y, F_z	78 to 79
B5	F_y, F_z	80 to 81
FUL	F_x, F_y, F_z, $M_{\theta x}$, $M_{\theta y}$, $M_{\theta z}$	82 to 87
FLL	F_x, F_y, F_z, $M_{\theta x}$, $M_{\theta y}$, $M_{\theta z}$	88 to 93
RMR	F_x, F_y, F_z, $M_{\theta x}$, $M_{\theta y}$, $M_{\theta z}$	94 to 99
MNT1	F_x, F_y, F_z, $M_{\theta x}$, $M_{\theta y}$, $M_{\theta z}$	100 to 105
MNT2	F_x, F_y, F_z, $M_{\theta x}$, $M_{\theta y}$, $M_{\theta z}$	106 to 111
MNT3	F_x, F_y, F_z, $M_{\theta x}$, $M_{\theta y}$, $M_{\theta z}$	112 to 117
MNT4	F_x, F_y, F_z, $M_{\theta x}$, $M_{\theta y}$, $M_{\theta z}$	118 to 123
MNT5	F_x, F_y, F_z, $M_{\theta x}$, $M_{\theta y}$, $M_{\theta z}$	124 to 129
MNT6	F_x, F_y, F_z, $M_{\theta x}$, $M_{\theta y}$, $M_{\theta z}$	130 to 135

Table D.2.: Outputs to be used in FRAC calculation

Input / Output	***0***	***1***	***2***	***3***	***4***	***5***
1	96.94%	98.64%	96.99%	98.22%	97.06%	97.13%
2	99.82%	99.88%	98.56%	99.76%	99.31%	97.91%
3	99.76%	96.93%	97.04%	99.61%	97.80%	98.71%
4	99.02%	99.71%	98.97%	98.73%	99.00%	97.93%
5	99.36%	99.82%	99.32%	99.64%	99.44%	99.32%
6	98.62%	97.02%	99.20%	99.44%	99.02%	99.56%
7	98.95%	99.64%	99.10%	99.49%	99.30%	99.09%
8	96.74%	96.68%	99.00%	99.44%	98.44%	99.55%
9	98.20%	99.01%	98.64%	98.29%	97.98%	97.27%
10	99.73%	99.93%	99.87%	99.70%	99.79%	99.26%
11	99.55%	96.39%	98.92%	99.51%	99.52%	99.25%
12	99.80%	99.83%	99.26%	99.82%	99.32%	99.07%
13	99.82%	99.08%	99.44%	99.63%	99.34%	99.43%
14	99.68%	99.84%	99.61%	99.69%	99.24%	99.22%
15	99.50%	99.22%	98.87%	99.35%	99.08%	99.25%
16	96.49%	97.41%	95.82%	98.12%	98.24%	97.73%

17	99.05%	99.64%	99.95%	99.14%	99.04%	98.81%
18	98.49%	99.16%	99.97%	99.19%	99.49%	98.48%
19	99.26%	99.73%	99.72%	99.38%	98.97%	99.29%
20	98.16%	97.55%	98.40%	98.05%	98.84%	98.36%
21	98.26%	98.55%	98.27%	98.44%	98.57%	96.89%
22	98.09%	99.34%	99.19%	98.36%	99.06%	98.66%
23	99.52%	99.88%	99.62%	98.87%	99.73%	98.90%
24	97.82%	98.80%	99.07%	98.76%	98.45%	97.48%
25	99.40%	99.69%	99.32%	99.49%	99.29%	99.31%
26	96.96%	96.34%	95.50%	97.83%	97.02%	93.22%
27	99.03%	99.36%	98.93%	98.72%	98.81%	96.11%
28	98.78%	99.36%	98.98%	99.36%	99.08%	98.63%
29	99.71%	99.65%	98.10%	99.47%	98.58%	98.97%
30	99.31%	98.71%	97.59%	99.13%	98.18%	99.07%
31	99.50%	99.44%	99.56%	99.39%	99.56%	99.25%
32	99.37%	99.50%	99.24%	99.58%	99.37%	99.27%
33	99.14%	99.27%	99.35%	99.53%	99.47%	99.42%
34	98.67%	99.15%	99.27%	99.11%	99.21%	98.24%
35	99.55%	99.88%	99.70%	99.38%	99.72%	99.33%
36	98.89%	98.86%	98.87%	99.20%	98.86%	98.82%
37	99.12%	99.47%	99.44%	99.40%	99.82%	99.66%
38	98.31%	98.85%	98.39%	98.33%	98.41%	96.61%
39	99.00%	99.51%	98.92%	98.93%	98.73%	98.15%
40	98.33%	98.98%	98.52%	98.49%	98.72%	96.94%
41	98.97%	99.74%	99.40%	99.10%	99.76%	99.05%
42	99.04%	99.11%	99.14%	99.31%	99.36%	99.08%
43	99.22%	99.24%	99.40%	99.25%	99.57%	99.00%
44	98.18%	98.57%	98.05%	98.38%	98.33%	94.97%
45	98.27%	98.85%	98.35%	98.46%	98.49%	94.82%
46	98.42%	99.22%	98.76%	98.71%	98.17%	99.21%
47	98.45%	98.01%	97.56%	99.32%	98.19%	99.21%
48	99.12%	98.90%	98.27%	99.39%	98.42%	99.16%
49	96.65%	96.23%	96.49%	97.89%	94.81%	96.96%
50	96.62%	96.37%	95.27%	98.56%	94.65%	97.89%
51	81.56%	85.33%	72.40%	88.50%	80.23%	80.07%
52	98.83%	99.46%	96.83%	98.44%	98.68%	98.21%

53	99.66%	99.58%	97.97%	99.46%	98.58%	99.70%
54	98.81%	98.93%	98.52%	99.42%	98.68%	99.21%
55	84.95%	81.65%	78.41%	88.68%	81.50%	82.01%
56	85.19%	82.85%	78.57%	90.36%	81.81%	83.57%
57	87.92%	90.43%	87.79%	68.30%	**61.77%**	67.60%
58	98.80%	98.86%	99.26%	99.39%	99.36%	99.32%
59	99.53%	99.38%	97.95%	99.43%	98.58%	98.79%
60	98.89%	98.98%	98.69%	99.39%	98.71%	99.00%
61	99.71%	99.73%	99.51%	99.61%	99.46%	99.27%
62	99.17%	99.24%	99.24%	99.38%	99.40%	99.23%
63	99.20%	99.21%	99.41%	99.53%	99.50%	99.36%
64	99.25%	99.58%	99.44%	99.36%	99.43%	99.66%
65	99.75%	99.68%	98.38%	99.45%	98.51%	99.86%
66	98.85%	98.93%	98.56%	99.44%	98.70%	99.34%
67	99.60%	99.55%	99.51%	99.44%	99.50%	99.21%
68	99.16%	99.27%	99.36%	99.53%	99.43%	99.33%
69	99.26%	99.31%	99.34%	99.56%	99.44%	99.38%
70	99.17%	99.65%	99.16%	98.54%	98.86%	97.37%
71	99.35%	99.85%	99.28%	99.53%	99.93%	99.74%
72	98.85%	97.76%	99.02%	99.59%	99.67%	99.81%
73	99.05%	99.76%	99.22%	99.15%	99.69%	99.27%
74	97.74%	97.38%	98.96%	99.51%	99.09%	99.66%
75	97.18%	98.79%	96.84%	98.21%	97.04%	97.09%
76	99.77%	100.00%	98.97%	99.72%	99.39%	97.87%
77	99.73%	97.38%	96.56%	99.58%	98.20%	98.95%
78	99.81%	99.90%	99.44%	99.66%	99.44%	98.13%
79	99.82%	97.65%	96.45%	99.44%	98.66%	99.20%
80	99.80%	99.91%	99.32%	99.36%	98.95%	98.38%
81	99.86%	99.09%	98.73%	99.27%	98.88%	99.11%
82	95.76%	96.39%	93.89%	97.32%	96.68%	93.53%
83	98.10%	98.56%	97.81%	99.37%	99.82%	99.83%
84	97.26%	98.93%	98.30%	99.28%	99.55%	99.73%
85	98.26%	98.78%	96.28%	99.67%	99.88%	99.88%
86	95.38%	95.79%	94.12%	97.25%	96.55%	93.76%
87	96.91%	97.57%	96.91%	98.81%	99.40%	98.02%
88	98.88%	99.61%	98.93%	99.50%	99.95%	99.76%

89	98.97%	99.53%	98.85%	99.78%	99.99%	99.91%
90	98.44%	99.10%	99.17%	99.60%	99.74%	99.89%
91	98.65%	99.10%	99.61%	99.79%	99.83%	99.94%
92	95.56%	95.36%	94.42%	98.42%	98.82%	97.28%
93	96.91%	98.43%	94.19%	99.48%	99.92%	99.71%
94	99.10%	99.26%	99.37%	99.51%	99.44%	99.34%
95	99.10%	99.27%	95.82%	99.35%	98.93%	99.33%
96	98.84%	98.76%	98.98%	99.17%	99.85%	99.93%
97	99.75%	99.81%	99.25%	99.58%	99.85%	99.97%
98	98.70%	99.11%	98.55%	99.44%	98.99%	99.15%
99	98.60%	98.52%	97.67%	99.38%	99.31%	99.56%
100	94.25%	95.57%	85.84%	96.90%	95.49%	98.50%
101	98.48%	99.57%	99.48%	99.73%	99.97%	99.82%
102	97.39%	96.33%	97.73%	99.02%	99.63%	99.81%
103	98.47%	98.62%	98.40%	99.27%	99.93%	99.81%
104	97.01%	98.07%	97.21%	97.52%	97.38%	97.41%
105	95.92%	95.29%	87.82%	98.41%	96.72%	99.04%
106	96.45%	96.51%	95.68%	97.05%	99.91%	96.03%
107	98.73%	99.41%	99.06%	99.51%	100.00%	99.86%
108	98.74%	99.45%	99.08%	99.53%	100.00%	99.86%
109	98.24%	98.45%	98.53%	99.30%	99.92%	99.78%
110	95.41%	94.47%	93.46%	97.29%	97.12%	98.48%
111	96.37%	97.03%	96.58%	98.44%	99.37%	99.28%
112	96.61%	98.44%	96.13%	99.09%	99.76%	99.14%
113	92.04%	94.39%	88.00%	98.45%	98.71%	96.98%
114	96.64%	95.64%	93.57%	97.72%	95.43%	95.79%
115	96.75%	96.19%	96.10%	96.93%	94.80%	95.27%
116	96.77%	96.37%	95.31%	97.67%	94.91%	96.36%
117	73.29%	82.06%	69.51%	79.40%	79.50%	65.90%
118	98.89%	99.64%	99.20%	99.31%	99.97%	99.61%
119	94.30%	97.97%	98.42%	89.99%	99.60%	93.87%
120	84.39%	83.10%	77.34%	94.79%	96.48%	92.20%
121	80.33%	79.55%	77.39%	89.65%	79.88%	85.45%
122	80.63%	79.42%	77.62%	89.28%	80.15%	83.46%
123	**63.79%**	**74.14%**	**68.10%**	**65.22%**	67.44%	**64.18%**
124	99.10%	99.28%	99.33%	99.47%	99.42%	99.36%

125	99.11%	99.07%	98.02%	99.19%	99.76%	99.90%
126	99.56%	99.46%	98.85%	99.14%	99.77%	99.90%
127	99.50%	99.60%	99.46%	99.45%	99.38%	99.38%
128	98.88%	99.22%	98.94%	99.48%	99.18%	99.18%
129	98.87%	99.21%	99.24%	98.93%	99.28%	98.33%
130	99.03%	99.33%	99.13%	99.51%	99.33%	99.95%
131	98.67%	98.02%	98.33%	99.18%	99.86%	99.99%
132	98.84%	98.48%	98.46%	99.14%	99.82%	99.99%
133	99.35%	99.36%	99.37%	99.32%	99.39%	99.62%
134	98.66%	99.20%	98.83%	99.06%	99.33%	99.57%
135	98.64%	99.14%	98.83%	98.68%	99.08%	98.37%

Table D.3.: FRAC values for the correlation between the generated model and the original model

The values in bold are the minimum in the corresponding columns.

D.2. Validation based on Pearson's correlation coefficient

Correlation coefficient (%)	ux	uy	zu	rotx	roty	rotz
at 6th stage of HPR	98.13	98.38	99.76	-	-	-
at B1	98.29	99.02	99.06	-	-	-
at B2	-	98.92	99.14	-	-	-
at B3	98.63	93.62	97.34	-	-	-
at B4	-	99.72	99.69	-	-	-
at B5	-	99.68	99.62	-	-	-
at FUL	99.12	99.63	99.39	98.83	96.06	93.88
at RMR	99.28	99.37	98.57	99.83	99.47	99.41
at front link of MNT	95.07	98.93	99.06	98.00	93.14	**92.51**
at rear lower link of MNT	99.35	99.31	98.92	99.84	99.02%	99.41

Table D.4.: Based on time response under excitation of unbalance at 150Hz

The value in bold is the minimum in this table.

Correlation coefficient (%)	ux	uy	zu	rotx	roty	rotz
at 6th stage of HPR	99.15	99.09	99.66	-	-	-
at B1	96.52	99.57	99.58	-	-	-
at B2	-	92.78	97.92	-	-	-
at B3	98.96	99.37	99.56	-	-	-
at B4	-	99.64	99.64	-	-	-
at B5	-	99.50	99.59	-	-	-
at FUL	98.59	99.31	99.03	98.67	98.72	98.20
at RMR	96.09	98.76	98.52	95.40	96.69	96.16
at front link of MNT	97.23	98.57	99.16	97.56	95.58	97.66
at rear lower link of MNT	99.29	98.36	93.23	92.69	**91.67**	93.64

Table D.5.: Based on time response under excitation of unbalance at 260Hz

E. Gyroscopic effect of the HPR and LPR on the WEM

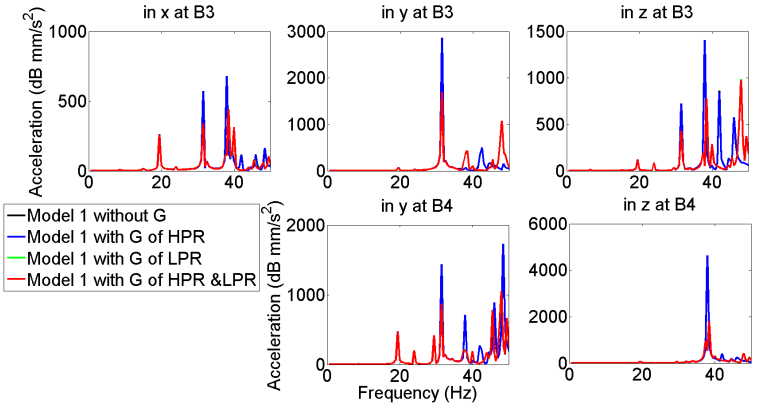

(a) 0 Hz-50 Hz

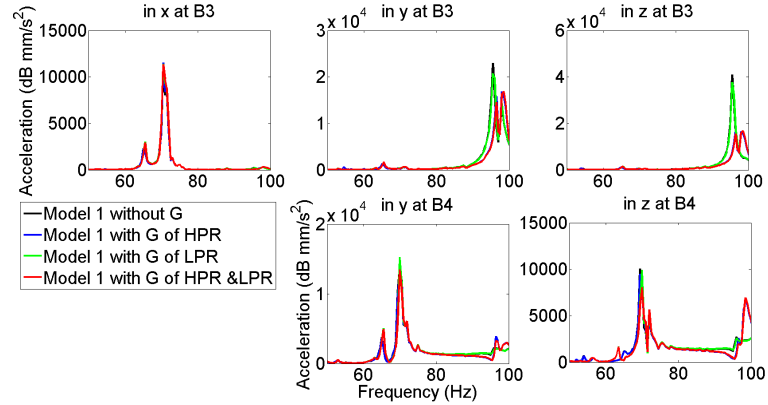

(b) 50 Hz-100 Hz

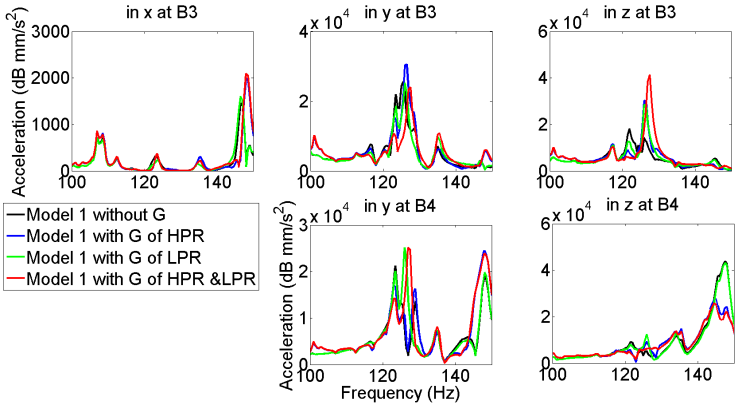

(c) 100 Hz-150 Hz

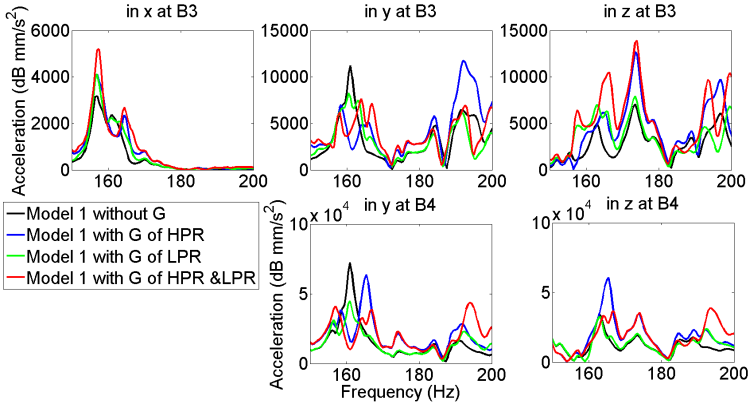

(d) 150 Hz-200 Hz

Figure E.1.: Frequency response of HPR (Model 1) to the unbalance showing gyroscopic effect of the HPR and LPR on the WEM